Copyright Warning & Restrictions

The copyright law of the United States (Title 17, United States Code) governs the making of photocopies or other reproductions of copyrighted material.

Under certain conditions specified in the law, libraries and archives are authorized to furnish a photocopy or other reproduction. One of these specified conditions is that the photocopy or reproduction is not to be "used for any purpose other than private study, scholarship, or research." If a, user makes a request for, or later uses, a photocopy or reproduction for purposes in excess of "fair use" that user may be liable for copyright infringement,

This institution reserves the right to refuse to accept a copying order if, in its judgment, fulfillment of the order would involve violation of copyright law.

Please Note: The author retains the copyright while the New Jersey Institute of Technology reserves the right to distribute this thesis or dissertation

Printing note: If you do not wish to print this page, then select "Pages from: first page # to: last page #" on the print dialog screen

NJIT
New Jersey's Science & Technology University

The Van Houten library has removed some of the personal information and all signatures from the approval page and biographical sketches of theses and dissertations in order to protect the identity of NJIT graduates and faculty.

ABSTRACT

MECHANICAL, ELECTRONIC AND OPTICAL PROPERTIES OF MULTI-TERNARY SEMICONDUCTOR ALLOYS

by
Dongguo Chen

The ability to obtain tunable properties with composition makes multi-ternary alloys extremely useful for a variety of applications in semiconductor devices and is of significant interest in experimental and theoretical research. This dissertation investigates the mechanical, electronic and optical properties of multi-ternary, i.e., binary, ternary and quaternary, semiconductor alloys using analytical methods and first-principles calculations.

For the calculations of mechanical properties, existing models on the average shear modulus of III-V & II-VI binary semiconductors are revised. New expressions are developed for the average Young's modulus as well as the shear modulus and Young's modulus on (111) plane for these compounds. It is found that the proposed models provide a simple and accurate means for predicting the elastic constants of ternary semiconductors.

The crystal structures, formation enthalpies and electronic properties of alloys, GaP_xSb_{1-x}, InP_xSb_{1-x} and CdS_xTe_{1-x}, are then investigated using first-principles calculations. These alloys are studied for various structures and compositions. Comparisons between GaP_xSb_{1-x} and InP_xSb_{1-x} are made. In the study of CdS_xTe_{1-x} system, negative bowing parameter of spin-orbit splitting is found in the ordered structure while positive value is found in disordered structure.

This work also gives a recipe to calculate the properties of Y2 alloys in any degree of crystal ordering. For the partially ordered samples, the trends of the Y2 ordering induced changes in the crystal field splitting and band gap narrowing are explored and explained in terms of the lattice mismatch and band offset between the binary constituents. The Y2 ordering induced change in the spin-orbit splitting is found to be positive and small.

Additionally, a model for the pressure dependence of the energy gap of group III-V & II-VI ternary semiconductor alloys is proposed. The trends in the pressure coefficients with respect to nearest neighbor distance and ionicity are discussed.

Finally, the electronic and optical properties of Cu_2ZnGeS_4, $Cu_2ZnGeSe_4$ and $Cu_2ZnGeTe_4$ in KS and ST structures are studied. Band structure and optical spectra including the dielectric function, refractive index, absorption coefficient and reflectivity are determined. The critical points in the optical spectra are assigned to the interband transitions in accord with the calculated band structures. The trends of these properties with respect to crystal structures and VI (S, Se and Te) anion atoms are explored qualitatively.

MECHANICAL, ELECTRONIC AND OPTICAL PROPERTIES OF MULTI-TERNARY SEMICONDUCTOR ALLOYS

by
Dongguo Chen

A Dissertation
Submitted to the Faculty of
New Jersey Institute of Technology and
Rutgers, The State University of New Jersey - Newark
in Partial Fulfillment of the Requirements for the Degree of
Doctor of Philosophy in Applied Physics

Federated Physics Department

May 2013

Copyright © 2013 by Dongguo Chen

ALL RIGHTS RESERVED

.

APPROVAL PAGE

MECHNICAL, ELECTRONIC AND OPTICAL PROPERTIES OF MULTI-TERNARY SEMICONDUCTOR ALLOYS

Dongguo Chen

Dr. Nuggehalli M. Ravindra, Dissertation Advisor — Date
Professor and Chair of Physics, NJIT

Dr. Keun Hyuk Ahn, Committee Member — Date
Assistant Professor of Physics, NJIT

Dr. Anthony T. Fiory, Committee Member — Date
Research Professor of Physics, NJIT

Dr. Martin Schaden, Committee Member — Date
Associate Professor of Physics, Rutgers, The State University of New Jersey — Newark

---

Dr. Vitaly Shneidman, Committee Member — Date
Senior University Lecturer of Physics, NJIT

BIOGRAPHICAL SKETCH

Author: Dongguo Chen

Degree: Doctor of Philosophy

Date: May 2013

Undergraduate and Graduate Education:

- Doctor of Philosophy in Applied Physics,
  New Jersey Institute of Technology, Newark, NJ, 2013
- Bachelor of Science in Applied Physics,
  Nanjing University of Science & Technology, Nanjing, P. R. China, 2009

Major: Applied Physics

Publications and Presentations:

1. D. Chen, and N. M. Ravindra, *Optical fingerprints of Y2 ordering in III-V ternary semiconductor alloys*. Semiconductor Science and Technology, (Accepted), 2013.
2. D. Chen, and N. M. Ravindra, *Structural, thermodynamic and electronic properties of* GaP_xSb_{1-x} *and* InP_xSb_{1-x}. Emerging Materials Research, 2013. **2**(2): p. 109-113.
3. D. Chen, and N. M. Ravindra, *Elastic properties of diamond and zincblende covalent crystals*. Emerging Materials Research, 2013. **2**(1): p. 58-63.
4. D. Chen, and N. M. Ravindra, *Pressure dependence of energy gap of III–V and II–VI ternary semiconductors*. Journal of Materials Science, 2012. **47**(15): p. 5735-5742.
5. H. Wu, D. Chen, D. Huang, and K. Deng, *Electronic and magnetic properties of* $SrCoO_3$*: The first principles study.* Acta Physica Sinica, 2012. **61**(3): p. 037101-037101-6.
6. C. Lamsal, D. Chen, and N. M. Ravindra, *Optical and electronic properties of AlN, GaN and InN: An analysis*. Supplemental Proceedings: Materials Processing and Interfaces, 2012. **1**: p. 701-713.

7. Z. Cheng, K. Lo, H. Opyrchal, J. Pan, D. Chen, T. Zhou, Q. Wang, G. E. Georgiou, and K. K. Chin, *Working quantum efficiency of CdTe solar cell*, Proceedings of 35th Photovoltaic Specialists Conference, 2010, **1**: p. 001912-001914.

8. Z. Cheng, J. Pan, Z. Wang, P. Kharangarh, D. Chen, R. M. Zhang, G. Wang, Z. Zheng, J. Liu, G. E. Georgiou, and K. K. Chin, *Simulations of dopants of p-CdTe thin film in n-CdS/p-CdTe solar cell*, Proceedings of 5th World Conference on Photovoltaic Energy Conversion, 2010, **1**: p. 3481-3485.

9. Y. Liu, D. Chen, and N. M. Ravindra, *Structural, optical and electronic properties of* CdS_xSe_{1-x}. Presentation at The Minerals, Metals and Materials Society Meeting, (San Antonio, TX, March 2013).

10. D. Chen, and N. M. Ravindra, *Mechanical properties of zincblende structured III-V & II-VI ternary semiconductors*. Presentation at the Materials Science & Technology Meeting, (Pittsburgh, PA, October 2012).

11. D. Chen, and N. M. Ravindra, *Optical and electronic properties of AlN, GaN and InN*. Presentation at The Minerals, Metals and Materials Society Meeting, (Orlando, FL, March 2012).

12. D. Chen and N. M. Ravindra, *Temperature dependence of optoelectronic properties of* CdS_xSe_{1-x}, CdS_xTe_{1-x} *and* $CdSe_xTe_{1-x}$. Presentation at American Physical Society Meeting, (Boston, MA, March 2012).

To my beloved parents: Taiqing Chen, and Sue Wang

ACKNOWLEDGMENT

I wish to express my sincere gratitude to Dr. N. M. Ravindra, not only for his valuable guidance, inspiration and encouragement during the entire course of this research, but also for his support, help and advices in my personal development. The knowledge and philosophies that I learnt from Dr. Ravindra will benefit me in my whole life. I wish to be as great an advisor to others as he is to me.

Special thanks are given to Dr. Keun Hyuk Ahn. As one of my thesis committee members, Dr. Ahn has been extremely generous with his time, knowledge and ideas to help me. I thank Dr. James C. Phillips, Distinguished Research Professor at Rutgers University (New Brunswick), Professor James A Van Vechten at Oregon State University, Dr. Suhuai Wei of National Renewable Energy Laboratory, Professor Emeritus Peter Y. Yu at the University of California, Berkeley and Dr. Victor V. Matveev, Associate Professor in the Department of Mathematical Sciences at NJIT for useful discussions in this research.

Acknowledgements are also extended to Dr. Anthoy T. Fiory, Dr. Martin Schaden and Dr. Vitaly Shneidman for serving on my dissertation committee.

I am greatly indebted to my beloved parents for their endless support and encouragement throughout my life and study.

TABLE OF CONTENTS

Chapter	Page
1 INTRODUCTION…………………………………………………………………	1
1.1 Semiconductors and Their Alloys………………………………………………	1
1.1.1 Growth Techniques………………………………………………………..	2
1.1.2 Wide Band Gap Alloys and Their Applications……………………....	5
1.1.3 Narrow Band Gap Alloys and Their Applications……………….....	7
1.1.4 Solar Cell Materials………………………………………………………..	8
1.2 Theory of First-Principles Calculations…………………………………...	10
1.2.1 Theoretical Background……………………………………………....	10
1.2.2 Density Functional Theory………………………………………....	13
1.2.3 Exchange-Correlation Functional…………………………………	15
1.2.4 Pseudopotentials………………………………………………………..	16
1.3 Dissertation Framework…………………………………………………....	18
2 MECHANICAL PROPERTIES OF BINARY AND TERNARY SEMICONDUCTORS………………………………………………………………	20
2.1 Overview…………………………………………………………………….	20
2.2 Existing Models on Bulk and Shear Modulus…………………………….	21
2.3 Development of New Expressions…………………………………….........	22
2.4 Comparison with Experimental Data……………………………………..	29
2.5 Elastic Constants of Ternary Semiconductors…………………………….	31
2.6 Summary……………………………………………………………………..	33
3 PROPERTIES OF III-V TERNARY ALLOYS………………………………..	34

TABLE OF CONTENTS
(Continued)

Chapter **Page**

3.1 Theoretical Background.. 34

3.2 Ordered Structures of Ternary Alloys.. 35

3.3 Structure Properties... 37

3.3.1 Lattice Relaxation.. 37

3.3.2 Bimodal Behavior.. 38

3.4 Formation Enthalpies... 38

3.4.1 Structure Dependence.. 39

3.4.2 Trend from Ga to In Cation.. 39

3.4.3 Alloy Mixture.. 41

3.5 Electronic Properties and Bowing Parameter................................ 41

3.5.1 Crystal Field Splitting.. 41

3.5.2 Band Gap... 42

3.5.3 Bowing Parameter.. 43

3.6 Comparison with Experiments and Other Calculations..................... 44

3.7 Summary.. 45

4 PROPERTIES OF II-VI TERNARY ALLOYS....................................... 46

4.1 Theoretical Background.. 46

4.2 Special Quasirandom Structures.. 48

4.3 Ground State Structures.. 49

4.4 Crystal Field Splitting.. 50

TABLE OF CONTENTS
(Continued)

Chapter **Page**

4.5 Spin-Orbit Splitting and Band Gap………………………………………….. 52

4.6 Dependence on Alloy Compositions……………………………………... 53

4.7 Comparison with Experiments……………………………………………. 55

4.8 Summary………………………………………………………………….. 56

5 FINGERPRINTS OF Y2 ORDERING IN III-V TERNARY ALLOYS………. 57

5.1 Spontaneous Y2 Ordering………………………………………………… 57

5.2 Hopefield Quasicubic Model……………………………………………... 58

5.3 Fingerprints of Y2 Ordering……………………………………………… 60

5.4 Comparison with Other Orderings………………………………………... 62

5.5 Comparison with Experiments……………………………………………. 65

5.6 Summary………………………………………………………………….. 67

6 PRESSURE DEPENDENCE OF ENERGY GAP OF III-V & II-VI TERNARY SEMICONDUCTORS…………………………………………….. 69

6.1 Theoretical Background…………………………………………………... 69

6.2 Modeling Pressure Dependent Band Gap of Ternary Alloys…………….. 71

6.3 Results and Discussion…………………………………………………… 77

6.3.1 Dependence of Pre-factor b_p on Pressure…………………………. 77

6.3.2 Bulk Modulus of Ternary Alloys…………………………………. 78

6.3.3 Trends in Pressure Coefficients of Energy Gap…………………... 78

6.4 Comparison with Experiments……………………………………………. 80

6.5 Temperature Coefficients of Ternary Alloys……………………………... 83

TABLE OF CONTENTS
(Continued)

Chapter **Page**

6.6 Summary…………………………………………………………….. 83

7 ELECTRONIC AND OPTICAL PROPERTIES OF I_2-II-IV-VI_4 QUATERNARY SEMICONDUCTORS………………………………………. 84

7.1 Theoretical Background…………………………………………………... 84

7.2 Crystal Structures…………………………………………………………. 85

7.3 Electronic Properties……………………………………………………… 87

7.3.1 Band Structures…………………………………………………… 88

7.3.2 Density of States…………………………………………………... 89

7.4 Optical Properties…………………………………………………………. 91

7.4.1 Dielectric Functions and Interband Transitions…………………... 91

7.4.2 Refractive Index…………………………………………………... 92

7.4.3 Absorption and Reflectivity………………………………………. 93

7.5 Summary…………………………………………………………….. 95

8 CONCLUSIONS AND FUTURE WORK…………………………………….. 96

8.1 Conclusions…………………………………………………………….. 96

8.2 Future Work…………………………………………………………. 98

LIST OF TABLES

Table **Page**

2.1 Calculated Elastic Moduli and Comparison with Experimental Results………………………………………………………………………... 27

2.2 Calculations of Elastic Constants of Some Ternary Semiconductors for Composition 0.5 and Comparison with Available Experimental Data…………………………………………………………..………….. 28

3.1 LDA Calculated Properties of GaP_xSb_{1-x}………………………...……….... 40

3.2 LDA Calculated Properties of InP_xSb_{1-x}………………………….…………….... 40

3.3 Experimental Valence Band Energy Levels (in eV) of Binary Constituents, GaP, GaSb, InP and InSb……………………………………………………….. 42

4.1 Calculated Properties of $CdS_{0.5}Te_{0.5}$ at Various Structures………..…...……. 51

4.2 LDA Calculated Valence Band Energy Levels of CdS and CdTe, Relative to Valence Band Maximum……………………………………………………... 51

4.3 Calculated Properties of CdS_xTe_{1-x} at Various Compositions along (100) Ordering……………………...…………………………………………….. 51

5.1 GGA Calculated Optical Fingerprints of Five III-V Alloys………………….. 63

5.2 Calculated Properties of Five Fully Y2 Ordered Compounds…………..……….. 63

6.1 Calculated Properties of III-V & II-VI Ternary Semiconductors for Composition 0.5…………………………………………………...………. 75

6.2 Comparison between Calculated Pressure Coefficients of Band Gap for Some Ternary Compounds for Compositions ≠ 0.5 and Al-Compounds.…… 77

7.1 Calculated Properties of Cu_2ZnGeX_4 (X=S, Se and Te)…………................... 88

LIST OF FIGURES

Figure		Page
1.1	Schematic drawing of Aix-200 II-VI MOCVD reactor for HgCdTe epitaxial growth. The system is equipped with additional mercury bath………………	3
1.2	Top cross-view of a MBE system…………………………………………….…	5
1.3	Chart of PV solar cell materials……………………………………….…...	9
1.4	A schematic illustration of all-electron potentials (solid lines) and pseudopotentials (dashed lines) and their corresponding wavefunctions. The all electron potentials and pseudopotentials match at the region $r > r_c$ ……...	17
2.1	Correlations between $Gd^{5.5}$ and ionicity f_i. Triangle and square points are experimental data. Solid lines are plotted using Equation (2.9b) and (2.10b)…………………………………………………………………....	26
2.2	Correlations between $Ed^{4.5}$ and ionicity f_i. Triangle and square points are experimental data. Solid lines are plotted using Equation (2.9a) and (2.10a)……………………………………………………………………	33
3.1	Crystal structures of ordered ternary semiconductor alloys $A_xB_{1-x}C$ at composition 0.25, 0.5 and 0.75……………………………………………….	36
4.1	The crystal structures of alloy $A_xB_{1-x}C$ at composition 0.5: (a) Y2 ordered structure and (b) SQS8 random structure……………………………………..	49
4.2	The effects of crystal ordering and composition on the spin-orbit splitting and band gap of CdS_xTe_{1-x}. Experimental values are plotted to compare with the calculated results………………………………………………………	52
4.3	The calculated partial and total density of states of CdS_xTe_{1-x} at various compositions…………………………………………………………………..	55
5.1	(a) The crystal structure of ternary alloy $A_xB_{1-x}C$ in Y2 ordering; (b) The Brillouin zone of the Y2 ordered superlattice……………………………...	59
5.2	The band structures for the (a) random and (b) Y2 ordered $Ga_{0.5}In_{0.5}P$ alloy are plotted along the high symmetry lines in the Brillouin zone. The arrow A denotes the interband transition responsible for the anomalous peak at 2.2 eV in the electroreflectance spectra…………………………………………...	64

LIST OF FIGURES
(Continued)

Figure **Page**

5.3 (a) Variation of the crystal field splitting $\left[\Delta_{CF}(1)-\Delta_{CF}(0)\right]$ with the band offset between alloys' binary constituents. (b) Variation of the band gap narrowing $\Delta E_g(1)$ with the alloys lattice mismatch………………………… 67

7.1 The crystal Structures of (a) Kesterite (KS) and (b) Stannite (ST) Cu_2ZnGeX_4……………………………………………………………… 86

7.2 Calculated band structures along the high-symmetry lines in the first Brillouin zone: T(Z): $2\pi/a$ (0, 0, 0.5) $\rightarrow \Gamma$: $2\pi/a$ (0, 0, 0) $\rightarrow$ N(A): $2\pi/a$ (0.5, 0.5, 0.5), for Cu_2ZnGeS_4, $Cu_2ZnGeSe_4$ and $Cu_2ZnGeTe_4$ in KS structure…... 87

7.3 The partial and total DOS of Cu_2ZnGeS_4 in KS and ST structures, $Cu_2ZnGeSe_4$ and $Cu_2ZnGeTe_4$ in KS structure……………………………… 90

7.4 The dielectric function $\varepsilon(\omega)=\varepsilon_1(\omega)+i\varepsilon_2(\omega)$ of Cu_2ZnGeS_4, $Cu_2ZnGeSe_4$ and $Cu_2ZnGeTe_4$ in KS and ST structures. The left panels represent the real part $\varepsilon_1(\omega)$ and the right panels represent the imaginary part $\varepsilon_2(\omega)$. The optical transitions E_{1A} and E_{1B} are labeled in the $\varepsilon_2(\omega)$ spectra……………... 92

7.5 The complex refractive index of Cu_2ZnGeS_4, $Cu_2ZnGeSe_4$ and $Cu_2ZnGeTe_4$ in KS and ST structures. The left panels represent the refractive index *n* and the right panels represent the extinction coefficient *k*………………………... 93

7.6 The normal incident reflectivity and absorption coefficient of Cu_2ZnGeS_4, $Cu_2ZnGeSe_4$ and $Cu_2ZnGeTe_4$ in KS and ST structures. The left panels represent the reflectivity *R* and the right panels represent the absorption coefficient α (cm^{-1}). The absorption coefficient is plotted in logarithm scale.. 94

CHAPTER 1

INTRODUCTION

1.1 Semiconductors and Their Alloys

A semiconductor is defined as a material with electrical conductivity in the range of 10^{-9} – 10^{2} S/m. Alternatively, it can be defined as a material with energy gap between 0 to 6 electron volts (eV). For example, Si and Ge have small energy gaps as 1.12 and 0.67 eV, respectively, while ZnS and Diamond have large band gaps as 3.60 and 5.50 eV [1]. Materials with zero band gaps are metals or semimetals and those with band gap large than 6 eV are considered as insulators. According to the types of band structures, materials can also be characterized as direct or indirect band gap semiconductors.

In the development of semiconductor technologies, semiconductor alloys have attracted much attention because of their ability to tailor the optoelectronic properties, such as, the band gap with the alloy compositions. For example, the band gap of $Al_xGa_{1-x}N$ varies from 3.42 to 6.20 eV when the Al composition x increases from 0 to 1. The most basic alloys are formed by two group IV elements, such as Si_xGe_{1-x} and Ge_xSn_{1-x}. Ternary alloys (AB_xC_{1-x}) are formed by substituting some atoms B in binary compound AB by C atoms which are usually in the same column with B in the periodic table, such as, the common-cation alloy CdS_xTe_{1-x} and the common-anion alloy $Ga_xIn_{1-x}P$. Similarly, quaternary alloys, such as, $Al_xGa_{1-x}N_yAs_{1-y}$, have been synthesized in experiment [2]. For some quaternary alloys, the atom can be replaced by other atoms from the neighbor columns in the periodic table. For example, Cu_2ZnGeS_4 can be formed by replacing Ga atom in $CuGaS_2$ compound by Zn and Ge atoms. These multi-ternary alloys will, in general,

inherit the structures of their parent alloys and short or long range of sub-ordering can be formed depending on the growth conditions.

1.1.1 Growth Techniques

The recent developments in crystal growth techniques have greatly fastened the experimental and theoretical studies on semiconductor alloys. Techniques such as Metal-Organic Chemical Vapor Deposition (MOCVD) and Molecular Beam Epitaxy (MBE) allow crystals to be deposited on substrates at fixed compositions within very small deviations. These techniques have made it possible to synthesize semiconductor devices with complicated structures, such as, MOS transistors and CIGS solar cells. Some growth techniques are briefly introduced here.

1.1.1.1 Growth of Bulk Crystals. Czochralski (CZ) method [3] is the most important and common method in the growth of semiconductor bulk crystals because it is capable of producing large diameter crystals. In this technique, the raw material is melted in a crucible. A small single-crystal seed is then lowered into the melt. The melt will be gradually pulled out and solidified onto the seed. The crystal orientation of the seed will determine the orientation of the resulting pulled crystals.

During the CZ crystal growth, the seed and crucible are normally rotated in the opposite directions to promote more uniform growth. However, the opposite rotations increase the corrosion of the crucible by the melt. The main unexpected impurities of the CZ technique are from the crucible material and gas surrounding the melt. For example, in the growth of bulk crystal Si, carbon evaporation from the graphite susceptor of quartz crucible and melt source results in the carbon incorporation in the crystal, typically at levels of 10^{15}-10^{16} cm^{-3} [4].

Another bulk crystal growth technique is the Bridgman Method, which is similar as the CZ method. The differences are the following: (I) A temperature gradient is implemented along the crucible for a better solidification; (II) The crucible can be positioned either vertically or horizontally to control convention flow. The Bridgman method is a popular way of producing certain crystals, such as, GaAs, for which the CZ technique is more difficult.

1.1.1.2 Growth of Thin Films. Epitaxial films are usually grown by Chemical Vapor Deposition (CVD) method. In CVD, gases containing the required chemical elements are introduced into the deposition chamber to react and form the desired film on the surface of the substrate. The semiconductors formed during the gas reaction are deposited as a thin film on a substrate inside the reactor.

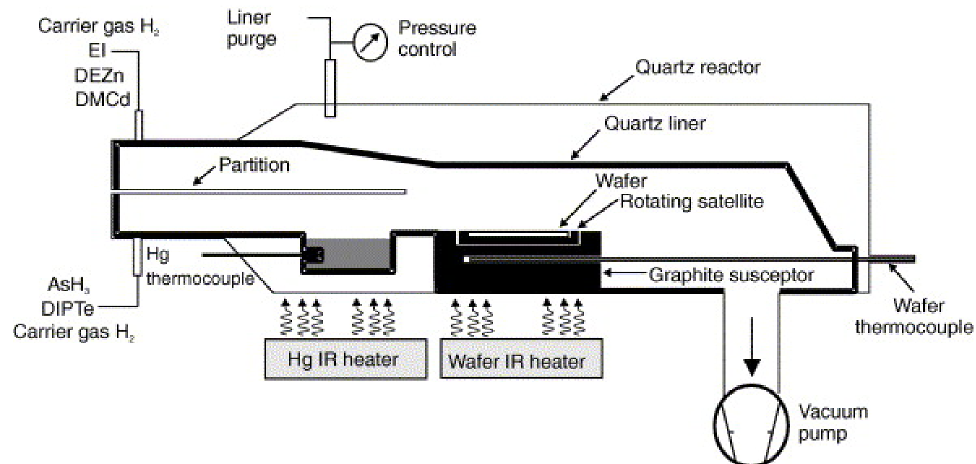

Figure 1.1 Schematic drawing of Aix-200 II-VI MOCVD reactor for HgCdTe epitaxial growth. The system is equipped with additional mercury bath [5].

Figure 1.1 shows the growth of ternary semiconductor HgCdTe alloys (MCT) using Metal-Organic Chemical Vapor Deposition (MOCVD) [5]. In this reactor, two separated gas inlet channels are provided to prevent premature gas reactions and dust formation. The precursors, dimethylcadmium (DMCd) and diethylzinc (DEZn), and the donor doping source Ethyl iodine (EI), together with the carrier gas H_2 are delivered into the reactor through the upper channel. The precursor, diisopropyltelluride (DIPTe), and the acceptor doping source, arsine AsH_3, together with the carrier gas H_2 are delivered into the reactor through the lower channel. The mercury source is held in the quartz container inside the reactor with temperature maintained at 200-220˚C. The MCT epilayer is formed onto the substrate at around 360-410˚C.

A typical disadvantage with the CVD technique is that the reactor may contains a high concentration of contaminants in the form of residual gases. This problem can be avoided in the Molecular Beam Epitaxy (MBE) method (Figure 1.2) [6]. The principle underlying MBE growth is relatively simple: a molecular beam is created in an effusion cell with a very small orifice by heating a source material until vaporization. The molecular beams from effusion cells at different angles then migrate in an UHV environment and impinge on a hot substrate surface, where the molecules can diffuse and eventually incorporate into the growing film. Despite the conceptual simplicity, it is difficult to control the crystal stoichiometry in MBE growth. However, it is possible to monitor the surface quality and epilayer growth conditions using some electron or ion based techniques, such as, Auger Electron Spectroscopy (AES) and Reflection High-Energy Electron Diffraction (RHEED) [4].

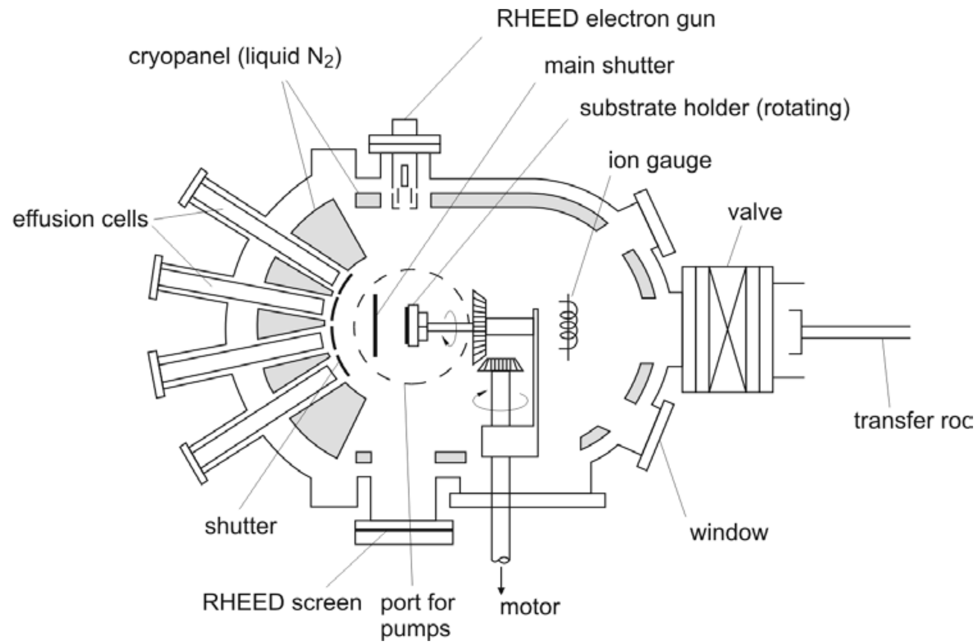

Figure 1.2 Top cross-view of a MBE system [6].

Some other techniques are also employed to grow semiconductor alloys. For example, the Liquid Phase Epitaxy (LPE) growth technique is extensively used in the growth of GaAs samples and devices [7]. The Ga metal is utilized as a solvent for As. When the solvent is cooled in contact with a GaAs substrate, it becomes supersaturated with As and the nucleation of GaAs starts on the substrate. The advantage of this method is that the equipment is inexpensive and easy to setup. However, it is difficult to control the growth conditions.

1.1.2 Wide Band Gap Alloys and Their Applications

Wide band gap (larger than 2.5 eV) semiconductors are experiencing extensive developments because of their thermal conductivities, breakdown electric fields, thermal and chemical stabilities at high temperatures and high powers [8]. A wide range of

materials have been investigated as wide band gap semiconductors, most notably 6H-SiC, III-V nitrides and ZnS based II-VI alloys.

The wide band gap energy and low intrinsic carrier concentration of SiC [9] will allow SiC semiconductor device to function at much higher temperatures . For example, 600˚C SiC device operation has been experimentally demonstrated on a variety of SiC devices [9]. Moreover, the high breakdown field and high thermal conductivity of SiC coupled with high operational junction temperature theoretically permit extremely high-power densities and efficiencies to be realized in SiC devices. For example, the high breakdown field of SiC relative to silicon enables the blocking voltage region of a power device to be roughly 10× thinner and 10× heavier doped, permitting a roughly 100-fold beneficial decrease in the blocking region resistance at the same voltage rating [10]. Finally, while SiC's smaller on-resistance and faster switching helps minimize energy loss and heat generation, SiC's higher thermal conductivity enables more efficient removal of waste heat energy from the active device.

The wide band gap III-V nitrides have been the subjects of great interest because of their applications in blue light emitting diodes and lasers as well as solar-blind UV photodetectors. Recently, much effort has been directed toward a p-i-n photodiode involving solely high Al content $Al_xGa_{1-x}N$ layers [11]. The choice of the p-i-n photodiode designed for solar-blind UV detectors is driven by its intrinsic advantages: (I) a very low dark current due to large potential barrier; (II) a high speed of operation; (III) a direct control of the quantum efficiency and speed through controlling the thickness of the intrinsic layer, and (IV) the device can operate under low to no bias. One of the greatest obstacles [12, 13] in these photodetectors is that the high activation energy of the

impurities (such as, Mg and Zn) results in a low concentration of free holes at room temperature.

The II-VI ZnS wide band gap semiconductor alloys have wide applications in fabricating technologically important solid state devices. The ZnS_xSe_{1-x} and ZnS_xTe_{1-x} semiconductor alloys are used to fabricate optoelectronic devices in blue-green spectral region since they have direct band gaps in the range of 2.75 – 3.66 eV and 2.10 – 3.66 eV [14]. These II-VI semiconductors can be grown lattice-matched on substrates such as Si, GaAs and GaP, making them potential candidates for high efficiency multi-junction solar cells and other applications in silicon technology. Due to the fact that 80% of the band offset between the corresponding binary constituents of the ternary alloy is in the conduction band when quantum wells are formed, $Zn_xCd_yMg_{1-x-y}S$-based quantum structures have recently found important applications in inter-subband devices, such as, quantum cascade lasers and quantum well photodetectors [15].

1.1.3 Narrow Band Gap Alloys and Their Applications

The narrow band gap alloy refers to the material with a band gap that is comparatively smaller than that of silicon. These band gaps are typically in the infrared region, i. e. near infrared with wavelength in the range of 0.78-3 μm, mid infrared with wavelength in the range of 3-50 μm and far infrared with wavelength in the range of 50-1000 μm. The narrow band gap alloys, such as, GaAsSb and HgCdTe can be used for infrared detectors and thermoelectrics.

One particular important narrow band gap semiconductor is the GaAsSb system, which allows Heterojunction Bipolar Transistors to operator in the terahertz (THz) range of frequencies. For example, the staggered band lineup at the GaAsSb/InP base-collector

junction not only eliminates the electron blocking problem but also allows electrons to be launched from the base to the collector at very high initial energies [16]. Moreover, GaAsSb grown at low temperature can also be used as a substitute for those traditional materials in THz applications.

The field of narrow band gap II-VI semiconductors is almost dominated by HgCdTe (MCT), although many potential alternatives, such as, InAsSb, PhSnSe and HgMnTe, have been suggested and discussed [17, 18]. The reasons that MCT is still the main infrared material are the following: (I) The band gap of MCT can be made to cover all infrared regions by varying the composition; (II) The lattice constant of MCT almost undergoes no change during the variation of the composition; (III) The material has direct band gap transitions and large absorption coefficient which allow the quantum efficiency to be 100%; (IV) Long minority carrier lifetimes result in low thermal noise allowing high-performance detectors to be made at the highest operating temperatures reported for infrared detectors of comparable wavelengths. All these advantages originate from the energy band structures of the material and they apply to all the situations whatever device architectures are used.

1.1.4 Solar Cell Materials

Solar cell is one very important application of semiconductors and their alloys. A brief overview on materials for solar cell production is given in Figure 1.3 [19]. Silicon is the leading material in solar cell production due to its abundance, maturity of technology and high conversion efficiency. However, due to its limitations as an indirect band gap semiconductor, many more materials are proposed and discussed, such as, CdTe and $Cu(In_{1-x}Ga_x)(S_{1-y}Se_y)_2$ (CIGS).

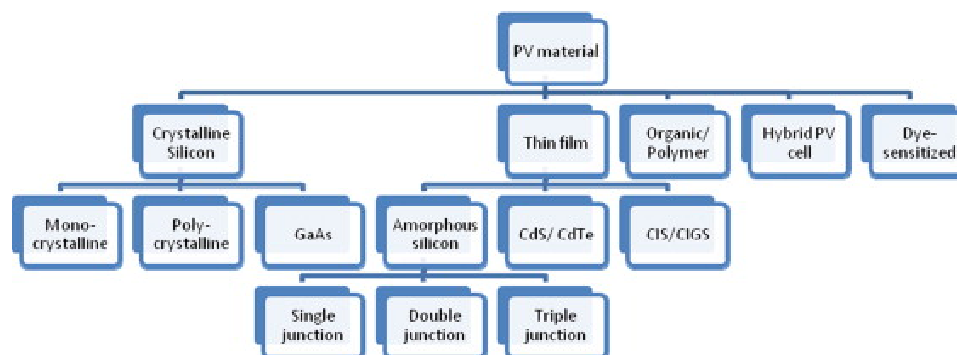

Figure 1.3 Chart of PV solar cell materials [19].

Silicon is the second easiest raw material that can be found on earth and has been widely used in developing solar cells. Monocrystalline silicon based solar cells have been reported to have the highest efficiency of more than 20%. In order to reduce the cost of monocrystalline silicon, polycrystalline silicon cell is developed which has minor flaws in the metal contamination and crystal structure and therefore the efficiency of polycrystalline silicon cell is relatively lower. In thin film technology, amorphous silicon is very more popular than other materials, such as, CdTe and CIGS, due to its higher efficiency. Amorphous silicon is a non-crystalline allotropic form of silicon and has 40 times higher rate of light absorption than monocrystalline silicon. The advantage of its disordered structure is the high band gap of about 1.7 eV [19].

GaAs is another solar cell material which has high efficiency, lower thickness and ideal band gap of 1.43 eV. Efficiency of GaAs solar cell can be improved by alloying it with certain materials, such as, Al, In, P and Sb. GaAs is lighter and has higher heat resistance compared to polycrystalline and monocrystalline silicon. However, GaAs material and manufacturing can be costly and therefore it is normally used for space applications due to its superior radiation hardness and excellent device performance at high temperatures [20].

CdTe has an ideal band gap of 1.45 eV and high absorption coefficient and has thus produced high efficiency of 15% [21]. It is also known for its stability for a long duration. However, this technology faces some problems that are related to the environment as well as the lack of Tellurium (Te). As an *n*-type semiconductor [22]It has been shown by experiments that doping of copper (Cu) into CdS layer will improve the photoconductivity. Moreover, the CdSTe interlayer formed between *n*-CdS and *p*-CdTe is believed to benefit the solar cell performance including its efficiency.

CIGS solar cell is still in its developing phase and is set to compete with silicon solar cells in performance. An efficiency of 20% for CIGS solar cell has been recorded [23]. Its band gap can be tuned to be close to ideal value by adjusting the composition of In or Ga atoms. For example, the band gap for ternary compounds $CuInSe_2$, $CuGaSe_2$ and $CuInS_2$ are 1.05, 1.68 and 1.65 eV, respectively. The absorption coefficient of $CuInSe_2$ is greater than 10^5 cm^{-1} [19]. One disadvantage with CIGS solar cell is that it contains expensive element, In, and its window layer, CdS, contains toxic element Cd. Recently, new quaternary semiconductor alloys, such as, $Cu_2ZnSn(S,Se)_4$ and $Cu_2ZnGe(S,Se)_4$, have been proposed for the substitution of CIGS since they have similar ideal band gaps and high absorption coefficient, but contain only inexpensive elements [24, 25]. However, many fundamental properties of these quaternary semiconductor alloys are not yet known.

1.2 Theory of First-Principles Calculations

1.2.1 Theoretical Background

The basic ideas of the First-principles calculations are based on the Born-Oppenheimer Approximation and the Hartree Fock Theory.

1.2.1.1 Born-Oppenheimer Approximation. The Hamiltonian of a many-body system can be written as [3],

$$H = \sum_{I=1}^{N} \frac{\vec{P}_I^{\,2}}{2M_I} + \sum_{i=1}^{N_e} \frac{\vec{p}_i^{\,2}}{2m} + \sum_{i>j} \frac{e^2}{\left|\vec{r}_i - \vec{r}_j\right|} + \sum_{I>J} \frac{Z_I Z_J e^2}{\left|\vec{R}_I - \vec{R}_J\right|} - \sum_{i,I} \frac{Z_I e^2}{\left|\vec{R}_I - \vec{r}_i\right|} \tag{1.1}$$

where $\vec{r}_i$, $\vec{r}_j$ are the positions of *i*th and *j*th electrons. $\vec{R}_I$, $\vec{R}_J$ are the positions of *I*th and *J*th ions. Z_I, Z_J are the atomic numbers of *I*th and *J*th ions. $\vec{p}_i$ and $\vec{P}_I$ are the momentum of *i*th electron and *I*th ion. m, M_I are the masses of electron and *I*th ion. e is the electron charge. In Equation (1.1), the first and second terms are the kinetic energy of ions and electrons. Third, fourth and last terms are the Coulomb interactions between electron and electron, ions and ion, electron and ion. To solve this many-body Hamiltonian, the Born-Oppenheimer Approximation [3] states that: (I) The electronic wavefunction depends on the nuclear positions $\vec{R}_I$ but not on their velocities, that is, the nuclear motion is so much slower than the electron motion that nuclear can be treated as fixed; (II) The nuclear motion sees a smeared out potential from the speedy electrons. From this approximation, the electron Hamiltonian can be decoupled out as follows:

$$H = \sum_{i=1}^{N_e} \frac{\vec{p}_i^{\,2}}{2m} + \sum_{i>j} \frac{e^2}{\left|\vec{r}_i - \vec{r}_j\right|} - \sum_{i,I} \frac{Z_I e^2}{\left|\vec{R}_I - \vec{r}_i\right|} \tag{1.2}$$

1.2.1.2 Hartree Fock Theoy. To solve the simplified many-body Hamiltonian, Hatree Fock theory [26] assumes that the wavefunction is given by a single Slater determinatnt of N spin-orbits as:

$$\Psi = \begin{vmatrix} \varphi_1(x_1) & \varphi_1(x_2) & \cdots & \varphi_1(x_N) \\ \varphi_2(x_1) & \varphi_2(x_2) & \cdots & \varphi_2(x_N) \\ \vdots & \vdots & \ddots & \vdots \\ \varphi_N(x_1) & \varphi_N(x_2) & \cdots & \varphi_N(x_N) \end{vmatrix} \tag{1.3}$$

where the variable x is the coordinates of the electrons. φ is the normalized electron wavefunction. Note that Ψ is antisymmetric with respect to an interchange of any two electron locations. Insert this wavelength into Equation (1.2) and minimize the Hamiltonian using Lagrange multiplier ε with respect to φ will yield:

$$\frac{\delta}{\delta\varphi}\left[< \hat{H} > - \sum_j \varepsilon_j \int \left|\varphi_j\right|^2 d\vec{r} \right] = 0 \tag{1.4}$$

Further simplification of the equation yields a set of one-electron equations as follows:

$$-\frac{1}{2}\Delta\varphi_i(\vec{r}) + V_{ion}(\vec{r})\varphi_i(\vec{r}) + U(\vec{r})\varphi_i(\vec{r}) = \varepsilon_i\varphi_i(\vec{r}) \tag{1.5}$$

where V_{ion} is the local ionic potential and $U(\vec{r})$ is a non-local potential. The full Hartree Fock Equations are given by:

$$\begin{aligned} e^2 \sum_{j \neq i} \int \frac{\left|\varphi_j(\vec{r}')\right|}{\left|\vec{r} - \vec{r}'\right|} d^3\vec{r}' \varphi_i(\vec{r}) - e^2 \sum_{j, j \neq i} \Delta_{S_{zi}S_{zj}} \int \frac{\varphi^*{}_j(\vec{r}')\varphi_i(\vec{r}')}{\left|\vec{r} - \vec{r}'\right|} d^3\vec{r}' \varphi_j(\vec{r}) \\ + \left(-\frac{\hbar^2}{2m}\Delta - \frac{Ze^2}{\vec{r}} \right)\varphi_i(\vec{r}) = \varepsilon_i\varphi_i(\vec{r}) \end{aligned} \tag{1.6}$$

The left hand side of the equations consists of four terms. The third and fourth terms denote the kinetic energy and electron-ion potential. The first term, or Hartree term,

is simply the electrostatic potential originating from the charge distribution of N electrons. The second term is the exchange term. The equation set (1.6) converts the many-body Hamiltonian into a number of one electron Hamiltonians and neglects the correlation between electrons. The Hartree Fock Equations, in general, yield too wide band gaps and too small band widths in semiconductor band structure calculations.

1.2.2 Density Functional Theory

The fundamental principle underlying the density functional theory is that the ground state energy of a many electron system can be represented by a functional of its electron density and is obtained by minimizing the energy with respect to the density.

1.2.2.1 Hohenberg-Kohn Theorem. The core of Hohenberg-Kohn theorem [27] is that the many electron system can be determined by the particle density $n(\vec{r})$. The original frame of density functional theory was proposed by Thomas and Fermi in 1927, known as Thomas Fermi model [27]. Hohenberg and Kohn greatly improved the DFT theory by the following two theorems: (I) The ground state energy of a many-body system is a unique functional of the particle density $E_0 = E[n(\vec{r})]$; (II) The functional $E[n(\vec{r})]$ has its minimum relative to variations of the particle density $\delta n(\vec{r})$ at the equilibrium condition $n_0(\vec{r})$.

Compare to Hartree Fock Equations, the Hohenberg-Kohn theorem considers the correlation between electrons. Its mathematical form can be written as follows:

$$E[n(\vec{r})] = F[n(\vec{r})] + \int n(\vec{r}) V_{ext}(\vec{r}) d\vec{r} \tag{1.7}$$

1.2.2.2 Kohn-Sham Equation. In order to find the solution of Equation (1.7), Kohn and Sham [27] separated $F\left[n(\vec{r})\right]$ into three distinct parts as follows:

$$E\left[n(\vec{r})\right]=T_s\left[n(\vec{r})\right]+\frac{1}{2}\iint\frac{n(\vec{r})n(\vec{r}')}{|\vec{r}-\vec{r}'|}d\vec{r}d\vec{r}'+E_{XC}\left[n(\vec{r})\right]+\int n(\vec{r})V_{ext}(\vec{r})d\vec{r} \tag{1.8}$$

where $T_s\left[n(\vec{r})\right]$ is the kinetic energy of a non-interacting electron gas with density $n(\vec{r})$. $E_{XC}\left[n(\vec{r})\right]$ is the exchange-correlation energy function. Using Lagrange multiplier and the normalization constraint on the electron density, $\int n(\vec{r})d\vec{r}=N$, the energy function $E\left[n(\vec{r})\right]$ can be rewritten as:

$$\frac{\delta}{\delta n(\vec{r})}\left[E\left[n(\vec{r})\right]-\mu\int n(\vec{r})d\vec{r}\right]=0 \tag{1.9}$$

Combining Equation (1.8) with Equation (1.9) , one can obtain:

$$\frac{\delta T_s\left[n(\vec{r})\right]}{\delta n(\vec{r})}+V_{eff}(\vec{r})=\mu \tag{1.10}$$

$$V_{eff}(\vec{r})=V_{ext}(\vec{r})+\int\frac{n(\vec{r}')}{|\vec{r}-\vec{r}'|}d\vec{r}'+\frac{\delta E_{XC}\left[n(\vec{r})\right]}{\delta n(\vec{r})} \tag{1.11}$$

With the above Equations (1.8)-(1.11), in order to find the ground state energy, E_0, and the ground state particle density, n_0, of a many-body system, it is only needed to solve the one electron Schrodinger Equation:

$$\left(-\frac{1}{2}\Delta + V_{eff}\left(\vec{r}\right)\right)\varphi_i\left(\vec{r}\right) = \varepsilon_i\varphi_i\left(\vec{r}\right) \tag{1.12}$$

Kohn-Sham Equations provide a theoretically exact solution for finding the ground state energy of an interacting many-body system. The only remaining question here is that the form of the exchange-correlation functional $E_{XC}\left[n\left(\vec{r}\right)\right]$ is unknown.

1.2.3 Exchange-Correlation Functional

Currently the exchange-correlation functional $E_{XC}\left[n\left(\vec{r}\right)\right]$ is most commonly approximated with the Local Density Approximation (LDA) [28] and Generalized-Gradient Approximation (GGA) [29].

In LDA, the exchange-correlation functional is given by

$$E_{XC}^{LDA}\left[n\left(\vec{r}\right)\right] = \int n\left(\vec{r}\right)\varepsilon_{XC}^{homo}\left(n\left(\vec{r}\right)\right)d\vec{r} \tag{1.13}$$

where $\varepsilon_{XC}^{homo}\left(n\left(\vec{r}\right)\right)$ is the exchange-correlation energy of a homogeneous electron gas with density $n\left(\vec{r}\right)$ and can be calculated from Quantum Monte Carlo methods. The LDA often works surprisingly well in more homogeneous systems and over-binds molecules and solids. However, it is very inaccurate in strongly correlated system where an independent particle picture breaks down.

To better simulate the charge density distribution, GGA improves the exchange-correlation functional of LDA by including the charge density gradient,

$$E_{XC}^{GGA}\left[n\left(\vec{r}\right)\right] = \int n\left(\vec{r}\right)\varepsilon_{XC}^{homo}\left(n\left(\vec{r}\right)\right)d\vec{r} + \int f\left[n\left(\vec{r}\right), \nabla n\left(\vec{r}\right)\right]d\vec{r} \tag{1.14}$$

where f is the correction chosen to satify one or several known limits for E_{XC}. There are two strategies for determining f: (I) Adjust f such that it satisfies most known properties of the exchange-correlation hole and energy; (II) Fit f to a large data-set with exactly known binding energies of atoms and molecules. Strategy (I) is to be preferred. Since GGA involves the charge density gradient, it predicts better results than LDA for the strongly correlated systems.

1.2.4 Pseudopotentials

The electron wavefunctions have rapid oscillations at the region near to the nuclei and consequently very large cut-off energy and basis set which will make the computation prohibitive. Fortunately, studies show that only the valence electrons participate in the correlations between atoms and core electrons can be assumed to be fixed. Based on this assumption, a pseudopotential can be constructed with two parts as shown in Figure 1.4. In the region near the nuclei, a pseudowavefunction with no rapid oscillation is used to replace the real electron wavefunction and in the valence electron region, it maintains the same as the real electron wavefunction.

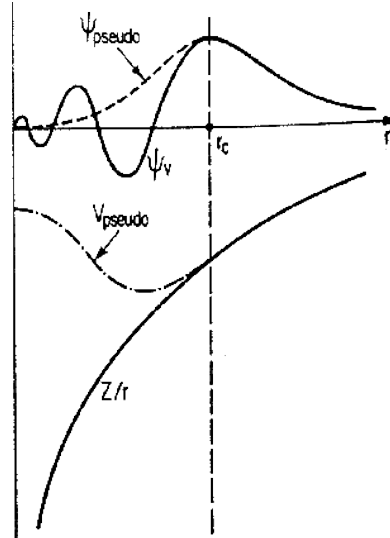

Figure 1.4 A schematic illustration of all-electron potentials (solid lines) and pseudopotentials (dashed lines) and their corresponding wavefunctions. The all electron potentials and pseudopotentials match at the region $r > r_c$ [30].

There are three commonly used pseudopotentials: norm-conserving pseudopotentials [31], ultrasoft pseudopotentials [32] and Projected Augmented Wave (PAW) method [33]. The norm-conversing pseudopotentials are constructed such that they match the true potentials in the valence electron region and yield the same charge densities. In addition, the integral of the squared amplitudes of the real and pseudopotential in the core region must be identical. This type of pseudopotentials usually requires high cut-off energies. The ultrasoft pseudopotentials are constructed such that they match the true pseudopotentials at the valence electron region. However, in the core region, instead of norm conservation, a generalized orthonormality condition is introduced to make the pseudowavefunctions as soft as possible. Therefore, the cut-off energies using ultrasoft pseudopotentials are dramatically reduced. The PAW method is a combination of pseudopotential and linear augmented plane wave method. It treats the shallow core electrons, such as, *d* and *f* electrons, as valence electrons. In this thesis, the ultrasoft

pseudopotential and PAW method are used to predict the electronic and optical properties of ternary and quaternary semiconductor alloys.

1.3 Dissertation Framework

As has been outlined, semiconductor multi-ternary (binary, ternary and quaternary) alloys have been extensively used in electronic and optoelectronic devices, such as solar cells. The quality and efficiency of devices are determined by the properties of these alloys. This dissertation studies the crystal structures, mechanical, electronic and optical properties of some multi-ternary alloys. This dissertation is organized as follows:

In Chapter 2, the existing model, in the literature, that relates the average shear modulus with the bond length and Phillips' ionicity has been extended to derive new models for the average Young's modulus, shear modulus and Young's modulus on (111) plane for diamond and zincblende crystals. The models are also used to predict the elastic constants of ternary semiconductors.

Chapter 3 investigates the properties of GaP_xSb_{1-x} and InP_xSb_{1-x} for various structures and compositions using first-principles method. The structure relaxation and band structure parameters, such as, crystal field splitting and band gap, are calculated and compared with experimental values.

In Chapter 4, studies of the properties of the CdS_xTe_{1-x} interlayer in CdS/CdTe solar cells, using first-principles calculations, are presented. The properties, including crystal field splitting, spin-orbit splitting, density of states and bowing parameters, are calculated and compared between different ordered and disordered structures.

Chapter 5 presents the effects of spontaneous Y2 ordering on the optical fingerprints of five III-V ternary semiconductor alloys. The trends of these optical

fingerprints are qualitatively explored. The results presented in this chapter can be used to predict the degree of ordering for ternary semiconductor alloys.

In Chapter 6, a general expression for the pressure dependent energy gap of a number of III-V and II-VI ternary semiconductor alloys are derived based on the previous work by Phillips and Van Vectchen. The trends of the pressure coefficient are analyzed with respect to the bond length and ionicity.

In Chapter 7, the electronic and optical properties of quaternary semiconductor alloys Cu_2ZnGeS_4, $Cu_2ZnGeSe_4$ and $Cu_2ZnGeTe_4$ are calculated. These materials are believed to be new substitutes for CIGS solar cells. This is the first work to systematically explore the basic properties, such as, crystal structures, electronic band structures and optical spectra, of these compounds

The last chapter is designated to be the conclusions of the dissertation and the blueprints for the future work.

CHAPTER 2

MECHANICAL PROPERTIES OF BINARY AND TERNARY SEMICONDUCTORS

2.1 Overview

As one of the most fundamental properties of materials, the research on elastic modulus, i.e., bulk modulus, shear modulus and Young's modulus is critical in order to understand the physical structures and mechanical behavior of materials. In fact, the ongoing research for superhard materials makes the study of elastic modulus more attractive because it is generally believed that harder materials should also have larger elastic modulus as in the case of diamond. It is also suggested that the ratio of bulk modulus to shear modulus is a critical parameter to address the fragility and brittle-ductile transition properties of materials [34]. Similarly, Young's modulus plays a significant role in the assessment of the fracture mechanics of materials. As semiconductor research advances from three dimensions (bulk) to two dimensions (thin films) and to one dimension (nanowire), shear modulus and Young's modulus become more important.

Inter dependencies of these elastic moduli are through elastic constants which are the fundamentals of almost all properties of materials. In experiments, these elastic constants are usually extrapolated from the experimental results of elastic modulus. In theoretical calculations, only first-principles calculations are generally used to evaluate these elastic constants. Due to the computational complexities and the associated cost of first principle calculations, researchers are always interested in developing simple analytical models for the elastic modulus.

In this chapter, the existing models on the bulk and average shear modulus are introduced. New expressions are proposed for shear modulus and Young's modulus on the

crystal (111) plane as well as the average Young's modulus for diamond and zincblende crystals. The proposed models are used to predict the elastic constants of III-V & II-VI ternary semiconductor alloys. This study on the elastic properties is one of the important prerequisites for the discussion of electronic properties and the derivation of the pressure coefficient of energy gaps in later chapters.

2.2 Existing Models on Bulk and Shear Modulus

One semi-empirical approach to determine the bulk modulus, B, of diamond and zincblende semiconductors was proposed by Cohen [35, 36] as the following:

$$B = (1972 - 220I)d^{-3.5} \tag{2.1}$$

where, d (in Å) is the bond length between two nearest neighbor atoms. I is an empirical ionicity factor defined by Cohen to account for the reduction in bulk modulus arising from increased charge transfer. The values of I are 0, 1 and 2, respectively, for group IV, III-V and II-VI semiconductors. Results of the calculation, based on Equation (2.1), yield a surprisingly good agreement with the experimental data [35, 36].

Recently, Kamran et al. [37] replaced the empirical ionicity factor I with a more physics-based Phillips' ionicity [38] and obtained a similar expression as in Equation (2.1). They also extended the ideas and developed similar expressions for the average shear modulus:

$$B = \frac{\kappa_2 - \lambda_2 f_i}{d^{3.5}} \tag{2.2}$$

$$G = \frac{\kappa_1 - \lambda_1 f_i}{d^{5.5}} \tag{2.3}$$

where κ_1, κ_2 and λ_1, λ_2 are constants. In recent calculations of average shear modulus, Kamran et al. [37] proposed that diamond and zincblende group IV, III-V and II-VI covalent crystals can be split into two groups (group *a* and *b*) with different fitting coefficients. In their work, diamond and grey tin are placed in group *a* while Si and Ge belong to group *b*. AlN and ZnS are put into group *a* while GaN, InN, ZnSe and ZnTe are put into group *b*.

2.3 Development of New Expressions

Following the ideas of the existing models on bulk and shear modulus, new expressions can be derived for shear modulus and Young's modulus on (111) plane as well as the average Young's modulus for diamond and zincblende crystals.

Young's modulus (E) can be experimentally determined from the slope of a stress-strain curve obtained from tensile tests performed on a material. The stress is the derivative of the elastic potential energy of the internal forces with respect to the strain. In elastic deformation, the potential energy is the same as the internal energy. Therefore, Young's modulus at the equilibrium state can be expressed in terms of the second derivative of the internal energy with respect to strain as follows:

$$E = \frac{\partial^2 U}{\partial \gamma^2} \tag{2.4}$$

where, U is the internal energy and γ is the strain. Similar expression for shear modulus G has also been developed by Roundy et al. [39] in their study on Al and Cu.

In general, the elastic deformation generated during the tensile tests will change the bond strengths of both core and valence electrons and, consequently, the internal energy levels. However, the bond strength in the core regime is so tightly bonded that the effect of the small elastic deformation on the inner core bond strength is negligible compared to that on the bond strength of valence electrons. Phillips [38] proposed a bonding-antibonding average energy gap E_g to describe the bond strength of valence electrons. This energy gap is separated into two parts: the homopolar energy gap E_h which characterizes the strength of pure covalent bond and the heteroploar energy gap C which characterizes the strength of pure ionic bond. Hence, the average energy gap is given by:

$$E_g^2 = E_h^2 + C^2 \quad (2.5)$$

Thus, $E_g = E_h$ for group IV covalent crystals/elements such as diamond and Si. Generally speaking, the ionic bonding arises from the long-range electrostatic force which undergoes no variation under small elastic deformation [38]. Cohen [35, 36] showed the independence of ionic energy gap C on lattice constant as well as the elastic modulus. Therefore, the internal energy in Equation (2.4), as stated above, characterized by valence bond strengths, can be simply replaced by E_h which, in Phillips' argument [38], is given as follows:

$$E_h = \frac{39.74}{d^{2.5}} \quad (2.6)$$

where, d is the bond length in Å. E_h is in units of eV. The strain, γ, in Equation (2.4), is usually expressed in a Taylor expansion formalism which, under small elastic deformation,

depends linearly on lattice constant and bond length. Based on the above argument, the following relation can be obtained for the Young's modulus:

$$E \propto d^{-4.5} \quad (2.7)$$

Noting that the Cohen's ionicity factor is empirical, it is convenient to adopt Phillips' ionicity [38] which is shown to have a decreasing linear trend with elastic modulus [40]. Based on this argument, the expression for Young's modulus is developed as follows:

$$E = \frac{\alpha - \beta f_i}{d^{4.5}} \quad (2.8)$$

where, α and β are constants, and f_i is Phillips' ionicity, defined by the terms in Equation (2.5) as $f_i = C^2 / E_g^2$. Similar derivation was applied to bulk modulus and average shear modulus by Cohen [35] and Kamran et al. [37] respectively. This theory on homopolar energy gap and ionicity for covalent crystals has also been adopted to develop relations for other mechanical properties such as hardness [41] and significant success has been demonstrated. However, it is found that Kamran et al. [37] used the experimental data of many crystals with hexagonal structure or the data along typical crystal directions to derive the coefficients in Equation (2.3). Therefore, the work in this chapter revised their results and extracted coefficients that are more reliable for materials.

The procedure to obtain the general expressions for elastic modulus is the following: firstly, the constants in Equations (2.3) and (2.8) are interpolated using some experimental data of covalent crystals with diamond and zincblende structures. The obtained expressions are then tested by comparing their predicted results with other

available experimental or theoretical data. Good accord with experiment indicates that the interpolated equations do reflect the correlations between bond length, ionicity and elastic modulus. The resulting expression for average Young's modulus and shear modulus are given as follows:

$$E_V = \frac{\alpha_V - \beta_V f_i}{d^{4.5}} = \frac{8539 - 6105.56 f_i}{d^{4.5}} \tag{2.9a}$$

$$G_V = \frac{\kappa_V - \lambda_V f_i}{d^{5.5}} = \frac{8591.48 - 6035.47 f_i}{d^{5.5}} \tag{2.9b}$$

It is worthwhile to mention that these two average elastic moduli in Equations (2.9a) and (2.9b) are typically for polycrystals since, in a polycrystal material, the anisotropy of single crystals is averaged out to yield an isotropic material. Significant attention has been paid to the isotropy of materials because it is believed that superhard materials should be homogenous and have an isotropic lattice with small bond length. In reality, all diamond and zincblende covalent crystals are anisotropic. However, the three-fold symmetry on (111) plane in these crystals leads to the assumption of fairly isotropic properties on this plane and, therefore, provides a path to study the isotropic properties of these crystals. It has been verified that the Young's modulus and shear modulus are isotropic on silicon (111) plane [42]. Recent work also shows that the elastic properties on the (111) plane are planar isotropic [43]. These factors enable the application of Equations (2.3) and (2.8) to determine the Young's modulus and shear modulus of diamond and zincblende covalent crystals on the (111) plane. The resulting expressions are as follows:

$$E_{111} = \frac{\alpha_{111} - \beta_{111} f_i}{d^{4.5}} = \frac{9166.18 - 7845.87 f_i}{d^{4.5}} \quad (2.10a)$$

$$G_{111} = \frac{\kappa_{111} - \lambda_{111} f_i}{d^{5.5}} = \frac{7539.44 - 5807.16 f_i}{d^{5.5}} \quad (2.10b)$$

The units for elastic modulus are in GPa and bond lengths are in Å. The correlations between elastic modulus, bond length and ionicity are plotted in Figures 2.1 and 2.2. The comparisons between the values from the modeled equations and other experimental and calculated data based on first-principles are listed in Table 2.1.

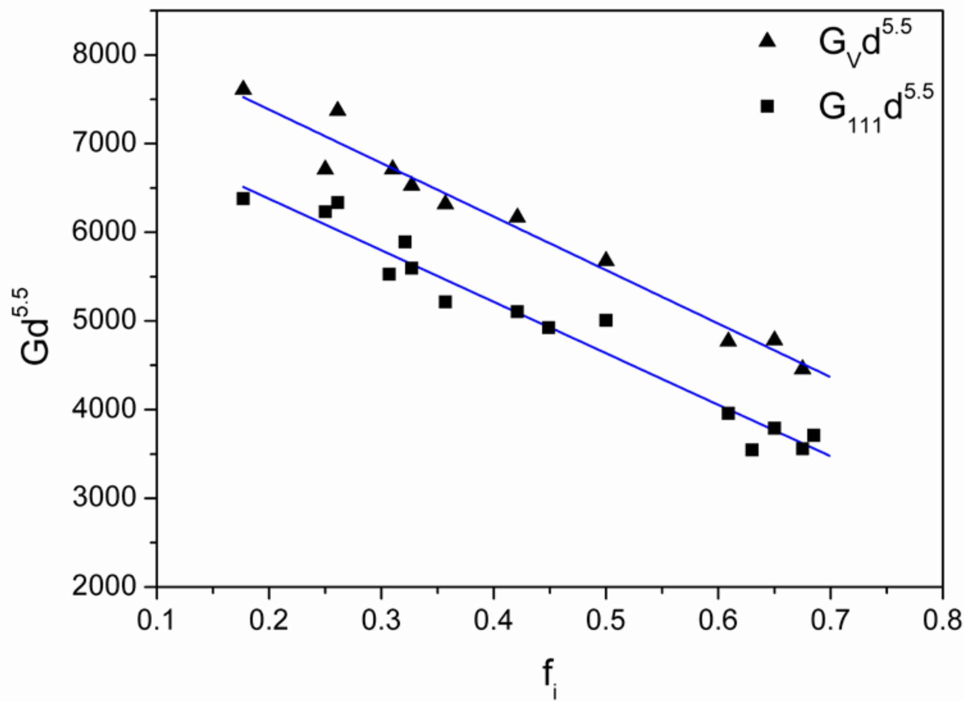

Figure 2.1 Correlations between $Gd^{5.5}$ and ionicty f_i. Triangle and square points are experimental data. Solid lines are plotted using Equations (2.9b) and (2.10b).

Table 2.1 Calculated Elastic Moduli and Comparison with Experimental Results

Crystal	d [1]	f_i [38]	C [38]	G_V (exp) [44]	G_V (cal)	G_{111} (exp) [44]	G_{111} (cal)	E_V (exp) [44]	E_V (cal)	E_{111} (exp) [1]	E_{111} (cal)
C	1.55	0	0	535.7	771.34 (725.61)	508.93	676.88 (634.79)	1144.6,	1188.27 (1131.41)	1165	1275.55 (1134.92)
Si	2.35	0	0	70.8	78.20 (70.99)	62	68.62 (62.10)	171.8	182.64 (168.91)	169	196.06 (169.43)
Ge	2.45	0	0	56.6	62.18 (56.45)	49.47	54.57 (49.38)	136	151.41 (140.03)	137.1	162.53 (140.46)
SiC	1.89	0.177	3.85	146[45] 231[46]	228.37	193.67[46]	197.66	363[45] 424 516[46]	427.40	423[45] 581[23] 603[46]	445.69
AlN	1.90	0.449	7.30		172.32	144.33[47]	144.50		322.74	302[48] 345	314.16
AlP	2.37	0.307	3.14	56.18[47]	59.11	48.5[47]	50.50	138.7[47]	138.32	138	140.24
AlAs	2.45	0.274	2.67		49.94		42.81		121.20	117.9	123.86
AlSb	2.66	0.25	2.07	31.1	32.83	28.89	28.22	79.4	86.37	84.7	88.73
GaN	1.96	0.5	7.64	140.2[47]	137.64	123.67[47]	121.12	267[49]	265.53	267	265.76
GaP	2.36	0.327	3.30	58	58.80	49.71	50.12	142.9	137.21	144	138.43
GaAs	2.45	0.31	2.90	48.8	48.86	41.57	41.73	120.4	118.30	121.3	119.86
GaSb	2.64	0.261	2.10	35.4	33.70	30.43	28.93	88	88.06	89.1	90.25
InN	2.16	0.578	6.78		73.85		60.53		156.60		144.76
InP	2.54	0.421	3.34	36.5	35.80	30.2	30.14	93.8	89.75	91.7	88.17
InAs	2.62	0.357	2.74	31.4	31.99	25.92	27.17	80.4	82.91	79.3	82.98
InSb	2.81	0.321	2.10	24.2	22.85	20.23	19.49	61.9	63.39	62.1	64.05
MgS	2.43	0.639	7.10		35.85		28.99		85.32	76.3	76.40

Table 2.1 Calculated Elastic Moduli and Comparison with Experimental Results (Continued)

Crystal	d [1]	f_i [38]	C [38]	G_V (exp) [44]	G_V (cal)	G_{111} (exp) [44]	G_{111} (cal)	E_V (exp) [44]	E_V (cal)	E_{111} (exp) [1]	E_{111} (cal)
ZnS	2.34	0.623	6.20	35.5	44.73	28.47	36.31	92.6	102.71	86.4	92.80
ZnSe	2.45	0.63	5.60	32.9	34.29	25.4	27.79	83.3	82.48	78.6	74.23
ZnTe	2.60	0.609	4.48	24.8	25.55	20.57	20.81	64	65.20	63.2	59.35
CdS	2.52	0.685	5.90	25.98[50]	27.51	22.9[50]	21.98	67.99[50]	67.81	50.9	59.02
CdSe	2.63	0.699	5.50	23.34[50]	21.38	20.63[50]	17.02	61.2[50]	54.96	46.5	47.37
CdTe	2.81	0.675	4.90	15.3	15.50	12.21	12.42	41	42.54	40	37.27
HgS	2.53	0.79	7.30		22.99		17.75		56.61	50.4	45.22
HgSe	2.63	0.68	5.00		21.81		17.45		56.16	42.2	49.04
HgTe	2.78	0.65	4.00	16.7[51]	16.29	13.23[51]	13.14	44.82[51]	44.62	40.3	39.70

In this table, G_{111} values are calculated from elastic constants. Also listed is the heteropolar energy gap C in Equation (2.5). Elastic modulus is in units of GPa, Bond length is expressed in Å.

Table 2.2 Calculations of Elastic Constants of Some Ternary Semiconductors for Composition 0.5 and Comparison with Available Experimental Data

	d [52]	f_i [52]	C [52]	B	C_{11} (exp)	C_{11} (cal)	C_{12} (exp)	C_{12} (cal)	C_{44} (exp)	C_{44} (cal)
GaInP[53]	2.456	0.378	3.333	81.95[54]	124	121.34	62	62.26	59	55.40
GaInAs[53]	2.534	0.395	3.198	67.42[54]	95	99.83	48	51.21	45	45.99
GaInSb[55]	2.725	0.235	1.827	46.4	74.6	72.88	32.2	33.16	34.5	34.96
CdZnTe[56]	2.725	0.604	4.086	45	60	60.53	38	37.23	23.8	25.47

2.4 Comparison with Experimental Data

In general, the calculated values of the elastic properties from Equations (2.9a), (2.9b), (2.10a) and (2.10b) show good accord with experimental data and other calculated results for zincblende group III-V & II-VI crystals. However, for group IV materials, a large discrepancy is observed. This is because of the fact that the Phillips' expression for E_h in Equations (2.5) and (2.6) is the optimized result for all the available cubic, hexagonal covalent materials and it is generalized to characterize the average optical gap of the material [38]. This optimization is not required for originally pure covalent group IV materials, such as diamond, Si and Ge, since $C = 0$ in Equation (2.5). Here, based on the power relations between elastic moduli and bond length as derived in Equations (2.9a), (2.9b), (2.10a) and (2.10b), new expressions can be proposed for all the four elastic moduli for group IV crystals. For average shear modulus: $G_V = 7799.55d^{-5.5}$, for shear modulus on (111) plane: $G_{111} = 6823.33d^{-5.5}$, while for average Young's modulus: $E_V = 7897d^{-4.5}$, and for Young's modulus on (111) plane: $E_{111} = 7921.51d^{-4.5}$. The coefficients of these four expressions for elastic modulus can be retrieved from the homopolar energy gap values determined from dielectric functions and lattice constants [35]. The calculated results are listed in parentheses in Table 2.1. For Si and Ge, the differences between experimental and calculated values are all within 3%. For diamond, the Young's modulus differs from experiment by 2.6% while the shear modulus differs by up to 35%. One possible reason is that the small bond length of diamond makes it incomparable to other heavier crystals in the periodic table [37, 40] or the s-p^3 hybridization and the high isotropy of diamond introduces certain different angular properties in diamond than in other materials. The anomaly in diamond suggests that the ionicity may not be the best parameter

to characterize the elastic modulus of various covalent crystals. One solution [57, 58] is to correlate the elastic modulus with the internal ionization energy because, in general, elastic deformation requires the bound electrons to cross the energy gap to contribute to excited states resulting in a reduction in the local bonding strength of valence electrons and, consequently, increase the polarizability and decrease the elastic modulus.

One interesting material is 3C-SiC which, in accordance with the composition of elements, belongs to group IV in the periodic table. According to the theory of ionicity and covalency, 3C-SiC is closer to group III-V partial covalent crystals. Experimental determination of the elastic constants of 3C-SiC is not even complete in the literature. This is due to the unavailability of single crystals of 3C-SiC material of the required size [46]. First-principles calculations of the elastic modulus of 3C-SiC are extremely scattered as listed in Table 2.1. In order to verify the properties of 3C-SiC, the elastic moduli of 3C-SiC have been calculated using Equations (2.9a), (2.9b), (2.10a) and (2.10b). The results are listed in Table 2.1. The equations for group IV crystals as proposed above are also used to calculate the elastic moduli of 3C-SiC. The results are as follows: $G_V = 236.76$ GPa, $G_{111} = 207.13$ GPa, $E_V = 452.54$ GPa and $E_{111} = 453.95$ GPa. Comparison of these two sets of calculated results with other available data is prone to show that 3C-SiC is much more similar to group III-V & II-VI partial covalent crystals than pure covalent group IV materials.

Since Phillips' homopolar energy gap E_h in Equation (2.5) is generalized to include broader range of crystals, the results of the calculations of group III-V and II-VI crystals, as shown in Table 2.1, are in excellent agreement with the available experimental and theoretical data based on first-principles methods in the literature. Some trends can be

observed from the calculated results. For common-cation system, ionicity decreases with increasing bond length. On the contrary, for common-anion system, ionicity increases with increasing bond length. These have also been investigated in the earlier work on group III-V and II-VI ternary semiconductors [52]. Despite different trends of the ionicity with bond length in various systems, elastic modulus always decreases with increasing bond length due to the large exponent in Equations (2.9a), (2.9b), (2.10a) and (2.10b). Therefore, elastic modulus is predominated by bond length and ionicity only plays an auxiliary influence. It is noteworthy that ZnS is an exception to the trend of the variation of ionicity with bond length in common-cation system. According to the trend, ZnS should have larger ionicity than ZnSe and ZnTe while its ionicity is much smaller. This is the reason for the calculated results of elastic modulus for ZnS to be always larger than the experimental values even within tolerable range.

2.5 Elastic Constants of Ternary Semiconductors

The proposed models for elastic modulus can be utilized to study the elastic properties of more complex materials with tetrahedral bonding. One good example is the ternary semiconductor alloys. They have attracted significant interest in recent years because of their applications in optoelectronics, including, photovoltaics. For example, CdZnTe has been studied extensively for use as an X-ray and Gamma ray detector due to its high photon attenuation coefficient and good charge transport properties. It is generally accepted that the isotropic elastic modulus are usually expressed by elastic constants through the following expressions:

$$B = 1/3(C_{11} + 2C_{12}) \tag{2.11a}$$

$$G_V = 1/5(C_{11} - C_{12} + 3C_{44}) \tag{2.11b}$$

$$G_{111} = 1/3(C_{11} - C_{12} + C_{44}) \tag{2.11c}$$

where C_{11}, C_{12} and C_{44} are the independent second order elastic constants of cubic crystals. Based on Equations (2.11a), (2.11b) and (2.11c), these elastic constants can be resolved in terms of bulk modulus B, average shear modulus G_V and shear modulus on (111) plane G_{111} as follows:

$$C_{11} = 1/3(3B + 9G_{111} - 5G_V) \tag{2.12a}$$

$$C_{12} = 1/6(6B - 9G_{111} + 5G_V) \tag{2.12b}$$

$$C_{44} = 1/2(5G_V - 3G_{111}) \tag{2.12c}$$

Equations (2.9b), (2.10b), (2.12a), (2.12b) and (2.12c) are used to extrapolate the elastic constants for group III-V & II-VI ternary semiconductor alloys. Bulk modulus can be calculated either from Equation (2.2) or taken from the available experimental data. Results of the calculations of elastic properties and comparison with experimental data are listed in Table 2.2. Good accord with the experimental data indicates that this approach can be applied to provide a theoretical prediction of elastic properties of other semiconductor alloys or more complex diamond or zincblende structure materials whose experimental data are unknown.

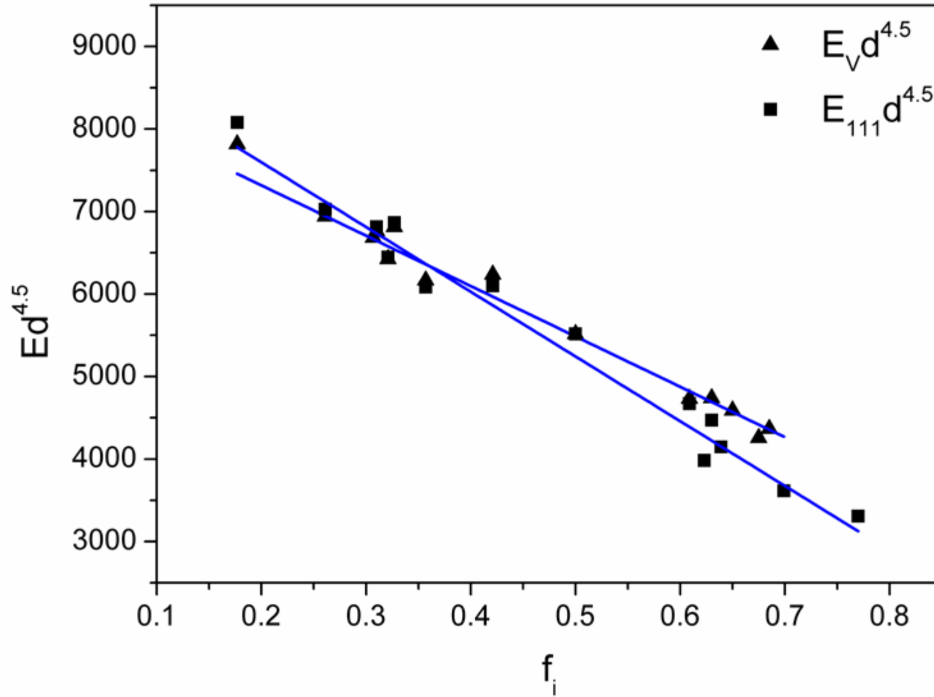

Figure 2.2 Correlations between $Ed^{4.5}$ and ionicity f_i. Triangle and square points are experimental data. Solid lines are plotted using Equations (2.9a) and (2.10a).

2.6 Summary

In this chapter, the existing work on average shear modulus has been corrected. New expressions are developed for average Young's modulus as well as shear modulus and Young's modulus on (111) plane for diamond and zincblende structure group IV, III-V & II-VI semiconductors. Analyses of the results of the new expressions show that the bond length dominates the elastic modulus while ionicity only plays an auxiliary role. The material 3C-SiC is shown to have elastic properties similar to that of partial covalent crystals other than pure covalent crystals. The corrected and newly proposed models on elastic modulus can be applied to derive elastic constants of some ternary alloys.

CHAPTER 3

PROPERTIES OF III-V TERNARY ALLOYS

When two zincblende binary compounds AB and AC are mixed to form the alloy AB_xC_{1-x}, the parent zincblende structure is generally inherited. However, the arrangement of atoms B and C can form periodic orderings. The types of orderings depend on the experimental growth temperature, growth rates, substrate orientation and so forth. One might expect important variations in the properties due to the different orderings.

In the previous chapter, models of the mechanical properties of ternary alloys, regardless of the crystal structures, were presented. In this chapter, the crystal ordered III-V ternary alloys, GaP_xSb_{1-x} and InP_xSb_{1-x}, are studied at composition 0.25, 0.5 and 0.75. A number of properties are addressed, including the following: (I) Qualitative relationship between structural relaxation and lattice mismatch; (II) Formation enthalpies; (III) Ordering-induced crystal field splitting; (IV) Alloy band gap and bowing coefficient.

3.1 Theoretical Background

Group III-V ternary semiconductor alloys have been studied for decades due to their technological applications such as optoelectronic devices and high-speed, low-power logic applications. For example, the adjustable band gap of GaP_xSb_{1-x} with composition makes it a potentially useful material in fiber optic communication systems [52]. The expected resonance enhancement of the hole impact ionization rate makes GaP_xSb_{1-x} a useful material for low-noise avalanche photodiodes utilizing hole injection [59]. InP_xSb_{1-x} is an interesting material for optical devices in the mid-infrared. The first mid-infrared lasers, using InPSb layers, have been reported by some groups [60, 61].

The III-V & II-VI ternary alloys can be divided into two categories: conventional alloys and unconventional alloys. The conventional alloys have small lattice mismatch between the binary constituents. For example, the lattice mismatch between AlAs and GaAs in compound $Al_xGa_{1-x}As$ is 0.14%. On the contrary, the unconventional alloys have large lattice mismatch between the binary constituents. For example, the lattice mismatch for GaP_xSb_{1-x} is 11.2%. The unconventional alloys are expected to have some anomalous properties [62-64], such as follows: (I) Structural anomaly at the percolation composition threshold; (II) Large and composition-dependent bowing parameter; and (III) Composition dependent interband transition intensities.

The research in the literature has focused on the properties of conventional alloys for various structures and properties of unconventional alloys for random structures. As unconventional ternary alloys, the crystal ordering structures have been observed in both GaP_xSb_{1-x} and InP_xSb_{1-x}. Therefore, this chapter investigates the properties of these two alloys for all possible ordered structures.

3.2 Ordered Structures of Ternary Alloys

The Landau-Lifshitz theory [65] on phase transitions provides rules to select a number of ordered structures which can interconvert, under well-defined constraints, into disordered phases of the same composition. The selection rules are follows: (I) The space group of the ordered structure must be a sub-group of that of the disordered alloy, and (II) The ordered structure must be associated with an ordering vector located at a special *k* point of the parent space group. For a ternary semiconductor alloy, AB_xC_{1-x}, there are five generally observed ordered structures derived from zincblende structure of the binary constituents (AB and AC): For composition 0.5-0.5, layered tetragonal CuAu-I like (CA, $P\bar{4}m2$, No.

115) structure, layered trigonal CuPt (CP, $R3m$, No. 160) structure and chalcopyrite (CH, $I\bar{4}2d$, No. 122) structure while for composition 0.25-0.75 and 0.75-0.25, Famatinite (FM, $I\bar{4}2m$, No. 121) structure and Luzonite like (LZ, $P\bar{4}3m$, No. 215) structure. Details of these structures can be found in References [66] and [67]. Figure 3.1 shows the crystal structures of these five orderings.

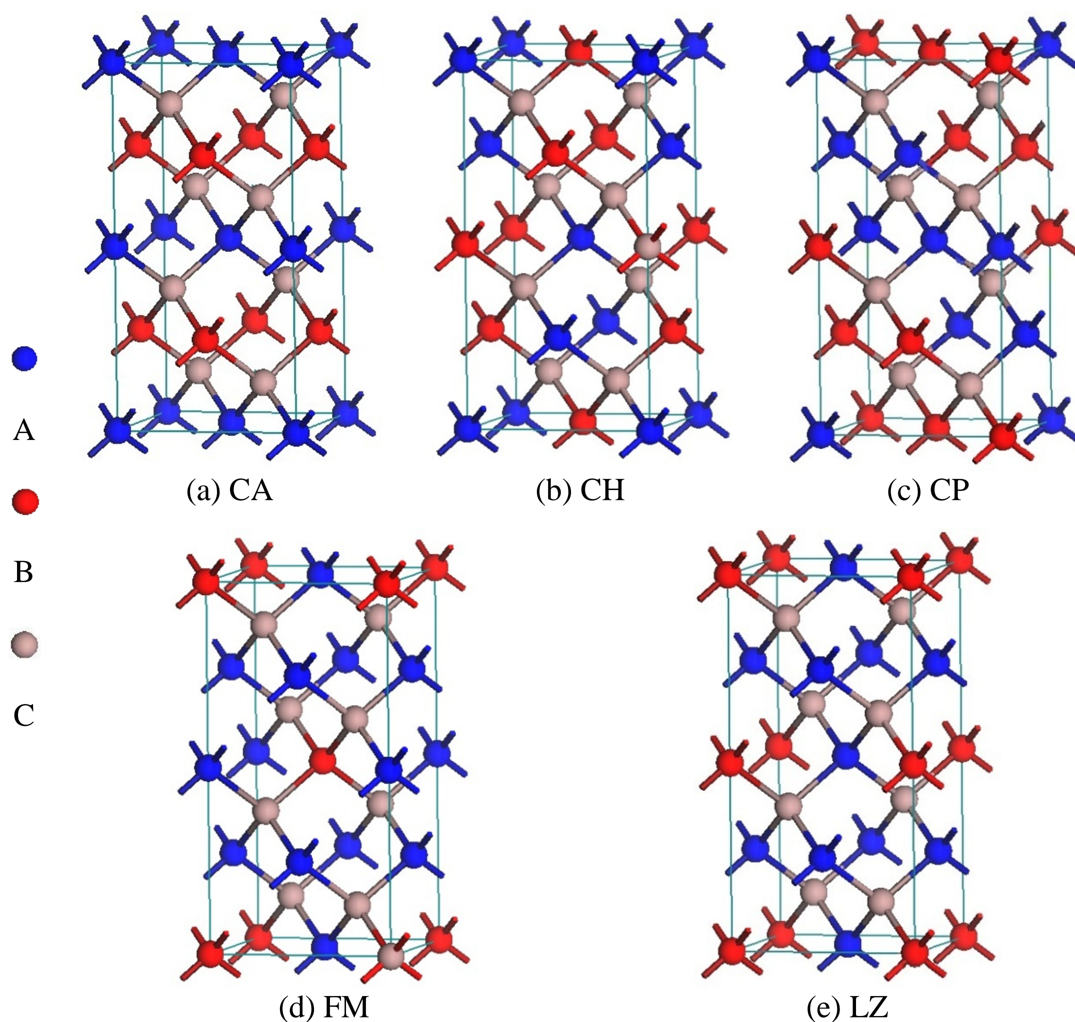

Figure 3.1 Crystal structures of ordered ternary semiconductor alloys $A_xB_{1-x}C$ at compositions 0.25, 0.5 and 0.75.

The sets of structures in Figure 3.1 can be organized into three groups according to the ordering vectors: (I) For the (0, 0, 1) ordering vector, there is CA structure at composition 0.5 and LZ structure at composition 0.25 and 0.75; (II) For the (2, 0, 1) ordering vector, there is CH structure at composition 0.5 and FM structure at composition 0.25 and 0.75; (III) For the (1, 1, 1) ordering vector there is CP structure at composition 0.5.

3.3 Structural Properties

The first-principles total energy minimization approach is applied to obtain the structural parameters of each ordered structure. The calculated lattice constants of the alloys, in accord with experimental data [68, 69], follow a linear function with the alloy compositions. Results are given in Tables 3.1 and 3.2. Some interesting features can be found in these calculations:

3.3.1 Lattice Relaxation

The standard zincblende structure has ideal tetragonal distortion parameter $\eta = 1$ and cell internal relaxation parameter $\mu = 0.25$, corresponding to fully relaxed structure. The deviations of these two parameters from their ideal values reflect how well the alloy is structurally relaxed. The calculated results, in Tables 3.1 and 3.2, show that the deviations of these two parameters from their ideal values in GaPSb compounds are larger than those in InPSb compounds. This is due to the fact that the lattice mismatch between the binary constituents in GaPSb (11.2%) is larger than that in InPSb (9.8%). This indicates that alloys with larger lattice mismatch between their constituents will be less relaxed.

3.3.2 Bimodal Behavior

It is observed that the bond length in ordered conventional alloys such as GaAsSb and AlGaAs is not uniformly distributed. But, instead, it exhibits a bimodal behavior [70]. In this work, the bond lengths in GaPSb and InPSb compounds have been calculated. The results of bond lengths in In alloys are listed below (units: Å):

ZB:	R(In-P)=2.525	R(In-Sb)=2.795
CA:	R(In-P)=2.576	R(In-Sb)=2.754
CH:	R(In-P)=2.539	R(In-Sb)=2.773
CP:	R(In-P)=2.500	R(In-Sb)=2.728 (×3)
	R(In-P)=2.611 (×3)	R(In-Sb)=2.820

Instead of average, the bond lengths exhibit a bimodal distribution. The short bonds in CA and CH structures are, in general, smaller while the long bonds are greater than those in the corresponding zincblende binary constituents. This local structure property indicates the importance of distortion and internal relaxation parameters in releasing the cell internal strain energy. Four different bonds (singlet and triplet) are observed in CP structure because there are more degrees of freedom to vary in that crystal relaxation. Similarly, singlet and doublet bonds are found in FM structure for composition 0.25 and 0.75.

3.4 Formation Enthalpies

The formation enthalpy ΔH of alloy AB_xC_{1-x} is defined in terms of the fully relaxed total energies E of the alloy and binary components as follows:

$$\Delta H(x) = E(AB_xC_{1-x}) - xE(AB) - (1-x)E(AC) \tag{3.1}$$

The calculated results of ΔH are presented in Tables 3.1 and 3.2. The following features can be found:

3.4.1 Structure Dependence

The calculated formation enthalpies show the trend ΔH (CP)> ΔH (CA)> ΔH (CH) for composition x=0.5, suggesting that the alloys favor CH structure as their stable ground state structure rather than CA and CP structures. In experiment, the Transmission Electron Diffraction (TED) pattern [71] shows a CA ordering mixed with disordered structure in GaPSb alloy. To check this partial ordering structure, the formation enthalpy of disordered $GaP_{0.5}Sb_{0.5}$ alloy has been calculated using Special Quasirandom Structures (SQS8) model [72]. It is found that ΔH (CA)> ΔH (SQS8)> ΔH (CH), indicating, as in experiment, a high possibility of finding a CA and random mixed structure. Similarly, ΔH (LZ)> ΔH (FM) suggests that FM structure is more stable than LZ structure. For a given ordering, such as CA and LZ along (100) direction, the dependence of formation enthalpy on composition is also observed.

3.4.2 Trend from Ga to In Cation

For a given structure, The calculated values show that the formation enthalpy decreases from GaPSb to InPSb compounds. This is due to the smaller lattice mismatch and smaller bulk modulus [42] in InPSb compounds. This smaller lattice mismatch leads to smaller strain energy and thus smaller formation enthalpy. This trend is consistent with the conclusion of lattice relaxation in Section 3.3.1 that alloys with larger lattice mismatch will be less relaxed.

Table 3.1 LDA Calculated Properties of GaP_xSb_{1-x}

Alloys	Structure	a (Å)	η	μ	ΔH (eV/atom)	Δ_{CF} (eV)	E_g (eV)	E_g (eV) (LDA+C)	b (eV)
$GaP_{0.75}Sb_{0.25}$	FM	5.554	0.998	0.268	0.039	0.042	0.832	1.56	3.306
$GaP_{0.75}Sb_{0.25}$	LZ	5.561	1.000	0.263	0.060	0	0.327	1.06	5.996
$GaP_{0.5}Sb_{0.5}$	CA	5.725	1.004	0.224	0.071	0.265	0.156	0.80	3.377
$GaP_{0.5}Sb_{0.5}$	CH	5.711	0.994	0.213	0.029	-0.082	0.891	1.52	0.438
$GaP_{0.5}Sb_{0.5}$	CP	5.735	1.002	0.234	0.084	0.523	-0.731	-0.10	6.923
$GaP_{0.25}Sb_{0.75}$	FM	5.882	0.998	0.231	0.027	0.012	0.365	0.90	0.98
$GaP_{0.25}Sb_{0.75}$	LZ	5.889	1.000	0.236	0.048	0	0.147	0.68	2.143

LDA+C refers to the LDA corrected band gap.

Table 3.2 LDA Calculated Properties of InP_xSb_{1-x}

Alloys	Structure	a (Å)	η	μ	ΔH (eV/atom)	Δ_{CF} (eV)	E_g (eV)	E_g (eV) (LDA+C)	b (eV)
$InP_{0.75}Sb_{0.25}$	FM	5.981	0.998	0.268	0.026	0.017	0.203	0.81	0.884
$InP_{0.75}Sb_{0.25}$	LZ	5.987	1.000	0.262	0.041	0	0.048	0.65	1.711
$InP_{0.5}Sb_{0.5}$	CA	6.142	1.003	0.225	0.049	0.195	-0.290	0.25	1.738
$InP_{0.5}Sb_{0.5}$	CH	6.132	0.995	0.217	0.020	-0.082	0.067	0.60	0.313
$InP_{0.5}Sb_{0.5}$	CP	6.147	1.002	0.234	0.059	0.517	-0.841	-0.31	3.946
$InP_{0.25}Sb_{0.75}$	FM	6.292	0.998	0.233	0.019	-0.001	-0.161	0.29	0.438
$InP_{0.25}Sb_{0.75}$	LZ	6.297	1.000	0.237	0.033	0	-0.291	0.16	1.129

LDA+C refers to the LDA corrected band gap.

3.4.3 Alloy Mixture

The calculated results in Tables 3.1 and 3.2 show that the formation enthalpy does not monotonically decrease from GaP to GaSb. Instead, ΔH is smaller in $GaP_{0.25}Sb_{0.75}$ and $GaP_{0.75}Sb_{0.25}$ and larger in $GaP_{0.5}Sb_{0.5}$. The same phenomenon is also found in In compounds. This is because the equal amount mixture of binary constituents induces more strain energy in the ternary systems and therefore larger formation enthalpy. This also explains the observation of large-range miscibility gap in experiments.

3.5 Electronic Properties and Bowing Parameter

Tables 3.1 and 3.2 also show the LDA calculated electronic properties (i.e., crystal field splitting, band gap) and bowing parameters. Together listed are the LDA corrected [73] band gaps in order to compare with experimental values since LDA underestimates the band gap. The bowing parameters are calculated using the uncorrected band gaps.

3.5.1 Crystal Field Splitting

According to the perturbation theory, for a given structure, an alloy with larger valence band offset between its binary components will have larger crystal field splitting. For a given alloy, the crystal field splitting induced by structure effect can be described by $(\Delta V)^2 / \left[\varepsilon_m(k_1) - \varepsilon_n(k_2)\right]$ [70]. Here, ΔV is the coupling matrix determined by the binary constituents' potential difference and bond length mismatch. The energy denominator refers to the energy difference between the binary components' unperturbed states before folding. The details of the folding relation can be found in Reference [70]. With these two facts, the calculated results can be explained as follows: (I) Amongst the

different structures, the following relation holds: Δ_{CF} (CP)> Δ_{CF} (CA)> Δ_{CF} (CH). This is because the energy difference $\varepsilon_m(k_1)-\varepsilon_n(k_2)$ of these structures follows an opposite sequence. For example, the energy difference ($\Gamma_{15v}-L_{3v}=0.925$ eV) of CP structure of alloy $GaP_{0.5}Sb_{0.5}$ is much smaller than the energy difference ($\Gamma_{15v}-X_{5v}=2.56$ eV) of its CA structure. The available experimental energy levels [1] have been listed in Table 3.3; (II) For a given structure, there always is Δ_{CF} (GaPSb)> Δ_{CF} (InPSb) due to the same trend in band offset: GaPSb (1.04 eV) > InPSb (0.92 eV); (III) The negative crystal field splitting in CH structure is because the stronger ($\Gamma_{15v}-W_{3v}$) coupling than ($\Gamma_{15v}-X_{5v}$) coupling makes the Γ_{4v} above Γ_{5v} state [74].

Table 3.3 Experimental Valence Band Energy Levels (in eV) of Binary Constituents, GaP, GaSb, InP and InSb

	GaP	GaSb	InP	InSb
Γ_{15v}	-0.08	-0.75	-0.11	-0.80
L_{3v}	-1.13	-1.55	-1.00	-1.40
X_{5v}	-2.85	-3.10	-2.00	-2.40
Γ_{1c}	2.90	0.81	1.43	0.24
L_{1c}	2.64	1.10	2.04	1.00
X_{1c}	2.35	1.72	2.30	1.70

3.5.2 Band Gap

The calculated values of direct Γ point band gaps for all the calculated alloy compounds have the following trend: E_g (CH)> E_g (CA)> E_g (CP) and E_g (FM)> E_g (LZ). This structure induced difference in band gap can also be explained in terms of the perturbation

theory used for crystal field splitting. However, the denominator energy difference will be mainly contributed by the conduction energy levels (Table 3.3) [1]. The energy difference in CP structure ($\Gamma_{1c} - L_{1c} = 0.015$ eV) in $GaP_{0.5}Sb_{0.5}$ is smaller than the energy difference in CA structure ($\Gamma_{1c} - X_{1c} = 0.18$ eV), resulting in a greater band gap narrowing and hence a smaller band gap in CP phase. Similarly, the largest band gap in CH structure is due to the greatest ($\Gamma_{1c} - W_{1c}$) difference compared to CA and CP structure. The same mechanism can also explain the band gap comparison between FM and LZ structures. Comparison between Table 3.1 and Table 3.2 also shows that the band gaps of GaPSb compound are always larger than those of InPSb compounds.

3.5.3 Bowing Parameter

The band gap $E_g(x)$ of a random AB_xC_{1-x} alloy is described by a bowing function as follows:

$$E_g(x) = xE_g(AB) + (1-x)E_g(AC) - bx(1-x) \tag{3.2}$$

where, b is the bowing parameter. $E_g(AB)$ and $E_g(AC)$ are the band gaps of binary constituents AB and AC, respectively. Results in Tables 3.1 and 3.2 show that the bowing parameters for these two systems depend strongly on the structures, that is, b (CP)> b (CA)> b (CH) and b (LZ)> b (FM). This is due to the different identities of the repelling states and the different symmetry properties. The calculations of GaPSb compound ordering along (001) plane shows that the bowing parameter increases by 58% from $GaP_{0.25}Sb_{0.75}$ to $GaP_{0.5}Sb_{0.5}$, and 78% from $GaP_{0.5}Sb_{0.5}$ to $GaP_{0.75}Sb_{0.25}$. For InPSb compound, the bowing parameter increases by 54% from $InP_{0.25}Sb_{0.75}$ to $InP_{0.5}Sb_{0.5}$. The

reason for this large and composition-dependent bowing parameter is attributed to the large differences between the two constituents in their lattice constants and energy levels.

3.6 Comparison with Experiments and Other Calculations

For the formation enthalpy, Fedders et al. [75] derived a model in terms of bond distortions and macroscopic elastic properties which predicts results that are in good accord with experiments. The model finds the formation enthalpies of $GaP_{0.5}Sb_{0.5}$ to be 0.053 eV and $InP_{0.5}Sb_{0.5}$ as 0.056 eV, in good agreement with the calculated values of CA structure. This comparison of formation enthalpy may suggest that the CA structure can serve as the representative structure other than CH and CP structures.

For GaPSb compounds, Stringfellow group reported [69] a low temperature photoluminescence peak at 1.394 eV for sample $GaP_{0.73}Sb_{0.27}$, and a fitted bowing parameter of 3.8 eV. Absorption spectra measurements [76] from the same group observed single-line peaks at 1.14 eV for $GaP_{0.53}Sb_{0.47}$ and 1.625 eV for $GaP_{0.76}Sb_{0.24}$ with bowing parameter 3.11 eV. In the calculation of this work, the CA and LZ structures of GaPSb compounds suggest that $GaP_{0.5}Sb_{0.5}$ and $GaP_{0.75}Sb_{0.25}$ should have band gaps of 0.8 and 1.06 eV and bowing parameter of 3.377 eV. The reason that their reported band gaps are larger than the predicted values is due to the fact that the structures of their samples are CA and disorder mixture and the band gap of random structure is larger than that of CA structure [74]. Room temperature photoluminescence and optical transmission measurements [77] observed a peak at energy 0.845 eV which is identified as band gap transition $E_0\left(\Gamma_v - \Gamma_{1c}\right)$, in agreement with the calculated data.

For InPSb compound, Jou et al. [78] found, via low temperature photoluminescence measurements, a direct band gap transition at an energy of 0.62 eV for $GaP_{0.69}Sb_{0.31}$ compared with the predicted value of 0.65 eV for composition 0.75-0.25. Their fitting to all the experimental data yields a band gap 0.35 eV for compound $InP_{0.5}Sb_{0.5}$ and bowing parameter 1.83 eV, in accord with the predicted value of 0.25 eV for band gap and 1.738 eV for bowing parameter. Similarly, photoluminescence and absorption spectra measurements, by Reihlen et al. [79], suggest a band gap of 0.445 eV for $InP_{0.577}Sb_{0.423}$ with bowing parameter of 1.52 eV. It is to be noted here that neglecting the spin-orbital interaction makes the calculated band gap to deviate from the experimental values.

3.7 Summary

In this chapter, the crystal relaxations, formation enthalpies and electronic properties of GaP_xSb_{1-x} and InP_xSb_{1-x} are discussed for various structures and compositions. GaP_xSb_{1-x} is found to be less relaxed than InP_xSb_{1-x} compounds. The formation enthalpy is found to be maximum at composition x=0.5. The crystal field splitting and band gap are larger in GaP_xSb_{1-x} than in InP_xSb_{1-x}. This has been explained in terms of the energy repulsion rules. All the properties are found to be strongly structure and composition dependent. Good accord between the calculated results and experimental values are obtained.

CHAPTER 4

PROPERTIES OF II-VI TERNARY ALLOYS

Two ordered III-V ternary alloys (GaP_xSb_{1-x} and InP_xSb_{1-x}) have been studied in Chapter 3. Properties that are investigated include: structure, formation enthalpy, crystal field splitting, energy gap and optical bowing parameters. In this chapter, the study is extended to the II-VI ternary alloys. The alloy CdS_xTe_{1-x} is used as the example. Different from the two alloys studied in last chapter CdS_xTe_{1-x} contains heavy atoms Cd and Te. Therefore, the Spin-Orbit (SO) splitting and its bowing parameter will be considered in this chapter. Moreover, a new Y2 ordered structure is included in the calculation. All the properties of the ordered structures are compared with those of the disordered structure.

4.1 Theoretical Background

Thin film CdS/CdTe solar cells have ideal band gap and high absorption coefficient. High energy conversion efficiencies up to 16% [80] have been achieved. The inter-diffusion between the CdS window layer and CdTe absorber layer leads to the formation of a mixed CdS_xTe_{1-x} interfacial layer. This layer is generally believed to be beneficial to the solar cell performance. Through interfacial layer formation, (I) the large strain energy due to the lattice mismatch (10.7%) between CdS and CdTe can be largely relieved; (II) the degree of inter-diffusion will certainly shifts the electrical junction away from the metallurgical interface and reduce the defect density at the interface [81]; (III) the adjustable band gap (E_g) with respect to the alloy composition will result in changes in the open-circuit voltage

V_{oc} and thus the efficiency of the solar cells. Unfortunately, despite the significant benefits from CdS_xTe_{1-x} alloy, many fundamental properties of this system are not yet understood. These fundamental properties include the following:

(I) The possible sublattice crystal orderings and their effects on the properties of alloys. A short-range ordering in CdS_xTe_{1-x} has been observed recently by a room temperature Raman spectroscopy measurement [82]. However, theoretical studies have only discussed the properties of this alloy for random structure. Therefore, it is worthwhile to address the possible crystal orderings and their effects on the properties of this system.

(II) The sign of the SO splitting (Δ_{SO}) bowing parameter $b(\Delta_{SO})$. The composition variation of the spin-orbit splitting can be fitted to the form:

$$\Delta_{SO}(x) = \overline{\Delta}_{SO}(x) - x(1-x)b(\Delta_{SO}) \tag{4.1}$$

where, $\overline{\Delta}_{SO}$ is the concentration-weighted average SO splitting. Controversy has existed for long time on the sign of $b(\Delta_{SO})$. Most of the early experimental studies [70] reported positive values, e. g. GaPAs (0.175 eV), InPAs (0.357 eV), GaInP (0.101 eV) and GaInAs (0.144 eV). Later on [83, 84], some negative values have been reported, e. g. ZnSeTe (-0.59 eV) and GaInP (-0.05 eV). Therefore, it is interesting to find out the SO splitting and its bowing parameter of CdS_xTe_{1-x} alloys.

(III) Dependence of band gap and its bowing parameter b on the alloy composition. For most semiconductor alloys, the bowing parameter is nearly independent of composition x. However, for alloys with large size and chemical disparity between its constituents, the bowing parameter could be strongly composition dependent [85].

Therefore, it is interesting to see whether the bowing parameter varies with composition in CdS_xTe_{1-x} compounds.

In order to answer these questions, this chapter studies systematically the electronic structures of CdS_xTe_{1-x} compounds. Calculation involves the properties including the following: (I) The crystal orderings and alloy formation energy; (II) Crystal field (CF) splitting Δ_{CF} and SO splitting Δ_{SO}; (III) The alloy band gaps and bowing parameters; (IV) Density of states.

4.2 Special Quasirandom Structures

Structural models, such as, Monte Carlo approach and large scale pseudopotential method used in the calculations of properties of random alloys have to involve either rather large number of configurations or large cell sizes to mimic the randomness. These models attempt to approach the random correlation functions between atoms by statistical means. However, these techniques are impractical for first-principles calculations.

In the Special Quasirandom Structures (SQS) theory [72], the first step is to specify a set of correlation functions that mimics the random alloy in a hierarchical manner, and then find the structures corresponding to that set of correlation functions. This theory, therefore, can mimic the random alloys using periodic structures with small number of atoms. Based on the level of randomness, the SQS method generated cells can be characterized as SQSN, where N is the number of atoms in the primitive cells. Specifically, SQS2 refers to zincblende structure; SQS4 refers to Y2 ordered structure (Figure 4.1a). Amongst the generated SQSN structures, SQS8 (Figure 4.1b) is accurate enough to mimic the behavior of random alloys. In this chapter, the properties of ordered CdS_xTe_{1-x} for

composition 0.5, i. e., CA, CH, CP and Y2, are compared with the properties of random SQS8 structure. The properties of LZ structure are compared with those of SQS8 structure for composition 0.25 and 0.75.

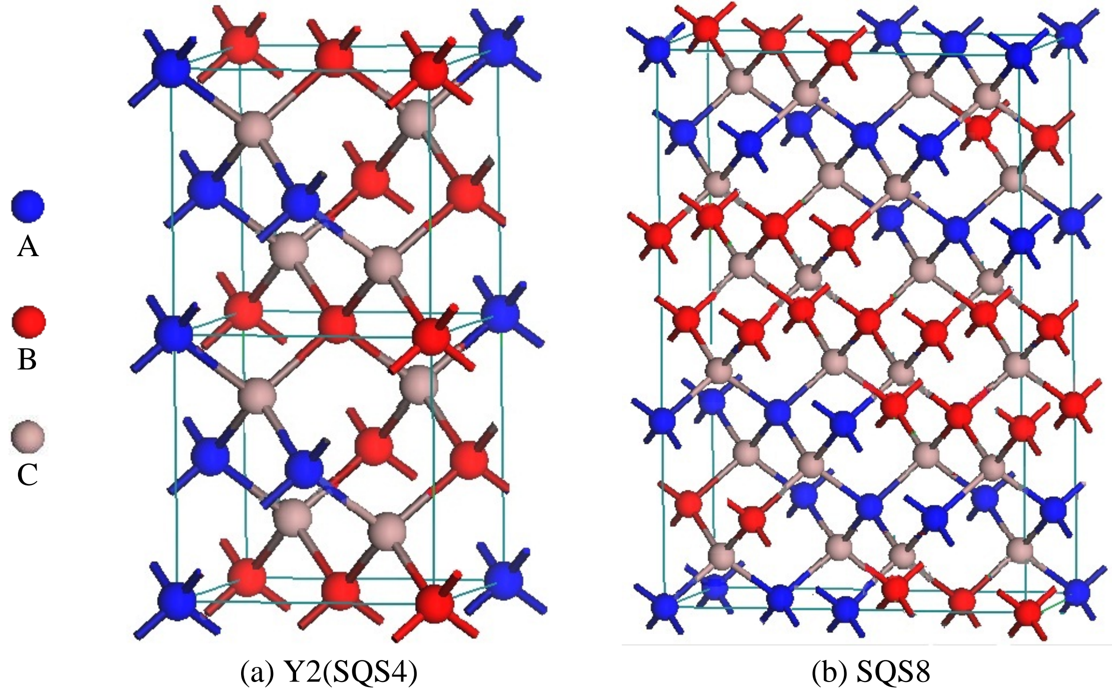

Figure 4.1 The crystal structures of alloy $A_xB_{1-x}C$ at composition 0.5: (a) Y2 ordered structure and (b) SQS8 random structure.

4.3 Ground State Structure

The calculated properties of ordered and disordered $CdS_{0.5}Te_{0.5}$ are listed in Table 4.1. It is found that the formation energy, defined as, $\Delta E = E(x) - \overline{E}(x)$, follows the trend: ΔE (CP)> ΔE (CA)> ΔE (SQS8)> ΔE (Y2)> ΔE (CH), indicating that CH is the ground state structure and contains lower strain energy and Madelung energy. It is noteworthy that the difference of formation energies between Y2 ordering and disordered SQS8 structures can be as small as 2 meV/atom. This suggests a possible ordered and disordered mixed

structure. Indeed, recent Raman Spectroscopy measurements [82] have reported a short-range ordering in random CdS_xTe_{1-x} system.

4.4 Crystal Field Splitting

It is known that the CF splitting Δ_{CF} and SO splitting Δ_{SO} separate the triply degenerate valance band maximum states into a singly and a doubly degenerate states. Δ_{CF} and Δ_{SO} of all the ordered and disordered structures have been extracted, as given in Table 4.1, using the Hopfield quasicubic model [86]. Δ_{CF} is defined to be positive if the doubly degenerate states are above the nondegenerate state. According to the perturbation theory and the folding relations, Δ_{CF} is inversely proportional to the difference of the unperturbed energy levels of the end-point binary constituents before folding into new states of the ordered ternary compounds [70]. Based on this theory, the crystal ordering effects on the CF splitting can be explained in terms of the energy levels of the binary constituents, as listed in Table 4.2 [87]. From Table 4.1, one can find that: (I) For the ordered structures, the following relation holds: Δ_{CF} (CP)> Δ_{CF} (CA)> Δ_{CF} (CH)> Δ_{CF} (Y2). This is because the energy difference follows the opposite trend. For example, the energy difference in CH ($\Gamma_{15v} - W_{3v} = 2$ eV) is larger than $\Gamma_{15v} - X_{5v} = 1.68$ eV in CA and $\Gamma_{15v} - L_{3v} = 0.67$ eV in CP ordering; (II) The CF splitting in CH ordering is small and negative due to the fact that the stronger ($\Gamma_{15v} - W_{3v}$) coupling than ($\Gamma_{15v} - X_{5v}$) coupling makes the Γ_{4v} above Γ_{5v} state; (III) Different from CA, CP, and CH, the doubly degenerate state in Y2 ordering is further split by a small amount into two nondegenerate states due to the yet lower symmetry.

Table 4.1 Calculated Properties of $CdS_{0.5}Te_{0.5}$ at Various Structures

Structure	a (Å)	η	ΔE (eV/atom)	Δ_{CF} (eV)	Δ_{SO} (eV)	$b(\Delta_{SO})$ (eV)	E_g (eV)	b (eV)
CA	6.0961	0.996	0.038	0.230	0.566	-0.437	0.189(1.37)	1.843
CH	6.0893	0.997	0.019	-0.124	0.497	-0.161	0.524(1.70)	0.506
CP	6.1002	1.002	0.051	0.720	0.678	-0.885	-0.471(0.71)	4.485
Y2	6.0889	0.995	0.027	-0.422	0.551	-0.377	0.202(1.38)	1.792
SQS8	6.0914	0.995	0.029	-0.219	0.417	0.161	0.270(1.45)	1.518

Listed properties include: lattice constant, tetragonal distortion parameter, formation energy, CF splitting, SO splitting and its bowing parameter, band gap and optical bowing parameter. The HSE06 corrected band gaps are given in parenthesis.

Table 4.2 LDA Calculated Valence Band Energy Levels of CdS and CdTe, Relative to Valence Band Maximum

	Γ_{15v}	W_{3v}	X_{5v}	L_{3v}
CdS	0.00	-1.95	-1.66	-0.65
CdTe	0.00	-2.05	-1.70	-0.68

Table 4.3 Calculated Properties of CdS_xTe_{1-x} at Various Compositions Along (100) Ordering

Composition	a	Ω	$b(\Delta_{SO})$	b
x=0.25	6.2589	0.140	-0.265	1.291
x=0.5	6.0961	0.152	-0.437	1.843
x=0.75	5.9352	0.163	-0.466	1.819

The calculated properties include: lattice constant, interaction parameter, bowing parameter of SO splitting and band gap.

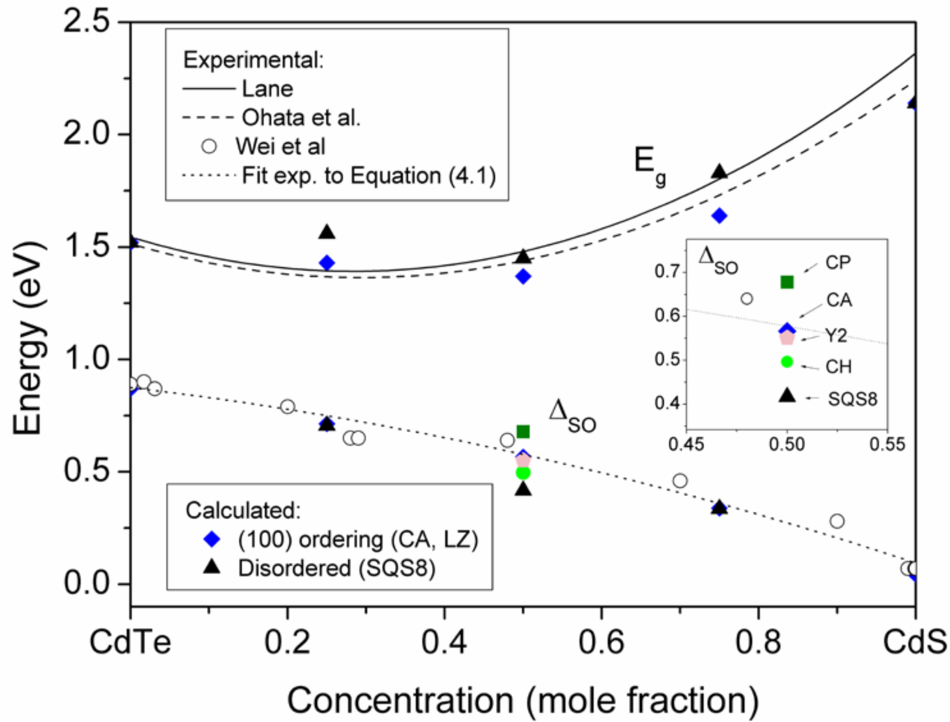

Figure 4.2 The effects of crystal ordering and composition on the spin-orbit splitting and band gap of CdS_xTe_{1-x}. Experimental values are plotted to compare with the calculated results.

4.5 Spin-Orbit Splitting and Band Gap

Earlier perturbation theory [88] treats the SO splitting Δ_{SO} as a disorder-induced effect and relates its bowing $b(\Delta_{SO})$ to the difference in *s-p* interaction of the alloy constituents. This theory predicts positive $b(\Delta_{SO})$. In order to explain some experimental observed negative bowing values [83, 84], Wei et al. [89] propose that interband *p-p* coupling enhances Δ_{SO} and dominates the value of $b(\Delta_{SO})$. From the calculated values in Table 4.1 for CdS_xTe_{1-x}, one can find the following: (I) The SO splitting shows strong ordering dependence. This indicates that the ordering geometry strongly affects the *s-p* and *p-p*

coupling; (II) Ordering structures yield negative $b(\Delta_{SO})$ and disordered structure yield a positive value. The ordering induced negative $b(\Delta_{SO})$ are consistent with the results of Wei et al. [89] and can be attributed to the intraband *p-p* coupling. The positive $b(\Delta_{SO})$ for disordered structure is due to the fact that the disorder effect mixes *d* state at the top of valence band with *p* states and this *p-d* hybridization reduces Δ_{SO}; (III) Largest $b(\Delta_{SO})$ is found in CP ordering and smallest is found in SQS8 structure. This suggests that the *p-d* coupling is strongest in SQS8 and weakest in CP ordering.

The calculated results also show that CP ordering has the smallest band gap (0.71 eV). This is due to the fact that the smallest ($\Gamma_{15v} - L_{3v}$) energy difference causes strongest repulsion in its energy levels. This repulsion lowers Γ_{1c} and raises Γ_{15v} states and thus results in smallest band gap. Similarly, CH ordering has the largest band gap relative to other structures. In principle, an ideal solar cell material should have a direct band gap around 1.3-1.5 eV. Therefore, experimental conditions should be controlled to avoid the formation of CP ordering.

4.6 Dependence on Alloy Composition

The composition effects can be studied by calculating the properties of CdS_xTe_{1-x} for composition 0.25, 0.5 and 0.75. The calculated lattice constants follow a simple linear function of composition x. The interaction parameter, $\Omega = \Delta E / x(1-x)$, increases with the increasing Te concentration. The SO splitting increases monotonically when the anion atomic number increases from S to Te. This is because the valence band has large anion *p* character, and the atomic SO splitting of the anion valence *p* state increases with the atomic

number [90]. The change in Δ_{SO}, however, is not linear function of the composition. Its bowing parameter $b(\Delta_{SO})$, as listed in Table 4.3, shows significant composition dependence. The calculations of band gap E_g show that initially, adding S into CdTe will actually reduce the band gap. Further increase in S concentration will eventually increase the band gap. This is due to the fact that at low S concentration, the bowing parameter b is larger than the band gap difference between CdS and CdTe. Results show that b and $b(\Delta_{SO})$ are both strongly composition dependent. However, b increases as $b(\Delta_{SO})$ decreases, unlike the scaling assumption used in the *s-p* model [88, 91].

The compositions and crystal orderings also have effects on the variations of the partial and total density of states (DOS) of CdS_xTe_{1-x}. As in Figure 4.3, for pristine CdS and CdTe, the top of the valence band is dominated by S 3*p* and Te 5*p* states, respectively, and the bottom of the conduction band is mainly derived from Cd 5*s* state. The DOS of ternary CdS_xTe_{1-x} can be seen as the combination of CdS and CdTe. With increasing Te concentration, the magnitude of Te states increases while the magnitude of S states decreases. It can also be found that: (I) The main Cd 4*d* peak red shifts from CdS to CdTe, implying that *p-d* coupling becomes weaker which explains the increase in SO splitting and the deduction of band gap; (II) The valence bandwidth increases with the mixing of CdS and CdTe and it reaches maximum at $CdS_{0.5}Te_{0.5}$, indicating the formation of CdS_xTe_{1-x} increases the mobility of holes generated by light irradiation and hence improves the solar cell performance. Calculation of DOS for various orderings (not graphed) for composition 0.5 shows that the CP ordering has widest valence bandwidth, followed by Y2 and disordered phases. Shifts of Cd 4*d* state shows that the *p-d* coupling is strongest in CH and disordered and weakest in CP ordering.

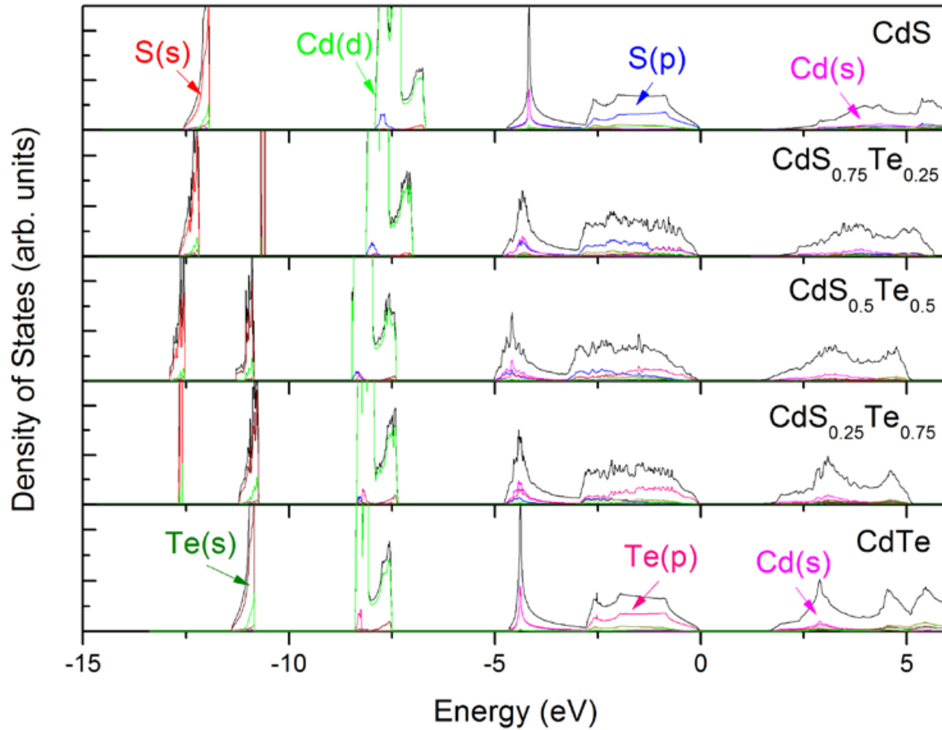

Figure 4.3 The calculated partial and total density of states of CdS_xTe_{1-x} at various compositions.

4.7 Comparison with Experiments

The calculated SO splitting and band gaps are compared with experimental data in Figure 4.2. Good agreement is found throughout the whole composition range. The only available data [92] on SO splitting was measured by room temperature ellipsometry. Fitting the experimental values to Equation (4.1) will yield a negative $b(\Delta_{SO})$ of -0.408 eV. Therefore, it is expected that the experimental samples are at least partially ordered. In order to have a direct comparison of the calculated band gaps with experiments [52, 93, 94], the LDA calculated results are corrected according to the Heyd-Scuseria-Ernzerhof hybrid functional calculations (HSE06) [95, 96] since LDA underestimates the absolute

band gaps. Comparison shows the following: (I) Amongst the ordered structures, (100) ordering (CA and LZ) is the best representation of the random alloy; (II) A small amount of Te in CdS can drastically reduce its band gap. This is because the impurity limit of Te substitution on S site leads to a localized isovalent impurity level [97]. The experimentally reported optical bowing parameters are around 1.7-1.88 eV [52, 94], well consistent with the calculated disordered and representative (100) ordering results.

4.8 Summary

In this chapter, the properties of CdS_xTe_{1-x} alloys have been investigated for various crystal orderings and compositions. Good agreement is seen between the calculated results and experimental data. The follow results are found: (I) CH is the ground state structure. Y2 ordering may occur in disordered structure due to small energy difference; (II) Ordering can significantly affect the SO splitting and energy gap; (III) Negative bowing parameter of spin-orbit splitting is found in ordered structure while positive value is found in disordered structure; (IV) The bowing parameters of energy gap and SO splitting are both strongly ordering and composition dependent. However, the bowing parameter of energy gap increases with decreasing bowing parameter of SO splitting.

CHAPTER 5

FINGERPRINTS OF Y2 ORDERING IN III-V TERNARY ALLOYS

The properties of fully ordered and fully disordered III-V & II-VI ternary semiconductor alloys have been studied in the previous two chapters. However, due to the experimental conditions, alloys are usually synthesized at a partially ordered structure. In this chapter, a method is provided to determine the properties of an alloy at any degree of ordering. Five ternary alloys with partial Y2 ordering are discussed, i. e. $Al_xGa_{1-x}As$, $Ga_xIn_{1-x}As$, $Ga_xIn_{1-x}P$, $GaAs_xSb_{1-x}$ and InP_xSb_{1-x}. Reported here are the fingerprints, including valence band splittings and band gap narrowing (the ordering induced band gap reduction relative to the random alloy), $\Delta E_g(\eta) = E_g(\eta) - E_g(0)$, of these five Y2 ordered compounds at partial and full degree of ordering. The physical factors that affect the fingerprints will be pointed out and the trends will be graphed. To generalize the research in Chapter 4, the properties of materials in Y2 ordering will also be compared with properties of these materials in other observed orderings in a brief manner. The calculated data in this chapter can be useful in analyzing experimental observations and deriving the ordering parameters of partially ordered samples.

5.1 Spontaneous Y2 Ordering

Spontaneous Y2 ordering of isovalent $A_xB_{1-x}C$ semiconductor alloys has been observed in vapor phase growth of several III-V systems [98-103]. However, the fundamental properties of this ordering have not been systematically studied. The ordered phase consists of alternate cation monolayer planes $A_{x+\eta/2}B_{1-x-\eta/2}$ and $A_{x-\eta/2}B_{1-x+\eta/2}$ stacked

along the [110] direction, where $0 \le \eta \le 1$ is the long range order parameter. η=1 corresponds to the fully ordered phase (Figure 5.1a) and $\eta = 0$ corresponds to the fully disordered phase. The degree of ordering depends on the experimental conditions, such as, the growth temperature and pressure, growth rates and substrate orientation etc.

When a zincblende disordered alloy forms the long-range ordered Y2 phase, the unit cell is increased and the Brillouin zone is reduced. The point group symmetry is changed from T_d to C_{2v}. These lead to a series of experimental observable changes in materials properties, including new photoluminescence and electroreflectance peak [100, 101], new x-ray diffraction spots at (1/2, 1/2, 0) [98, 99], new pressure deformation potential [104] and the shift in absorption edge [98]. In this work, the study focuses on the changes of optical properties near the absorption edge. These changes are due to the fact that, in the ordered phase, the Γ, X and Σ points in the zincblende binary constituents all fold into the Γ point at the Y2 Brillouin zone (Figure 5.1b). These folding relations couple the states that have the same symmetry and this coupling splits the degenerate states in the random alloys.

5.2 Hopefield Quasicubic Model

In the absence of spin-orbit (SO) splitting, the valence band maximum (VBM) of the random alloy is a triply degenerate state with Γ_{15v} symmetry (Figure 5.2a). In Y2 ordering, this state splits into a single state Γ_{1v} and a doubly degenerate state. The doubly degenerate state splits further into two single states Γ_{2v} and Γ_{3v} due to the yet lower symmetry (Figure 5.2b). In the presence of SO splitting, the amount of splitting becomes more significant.

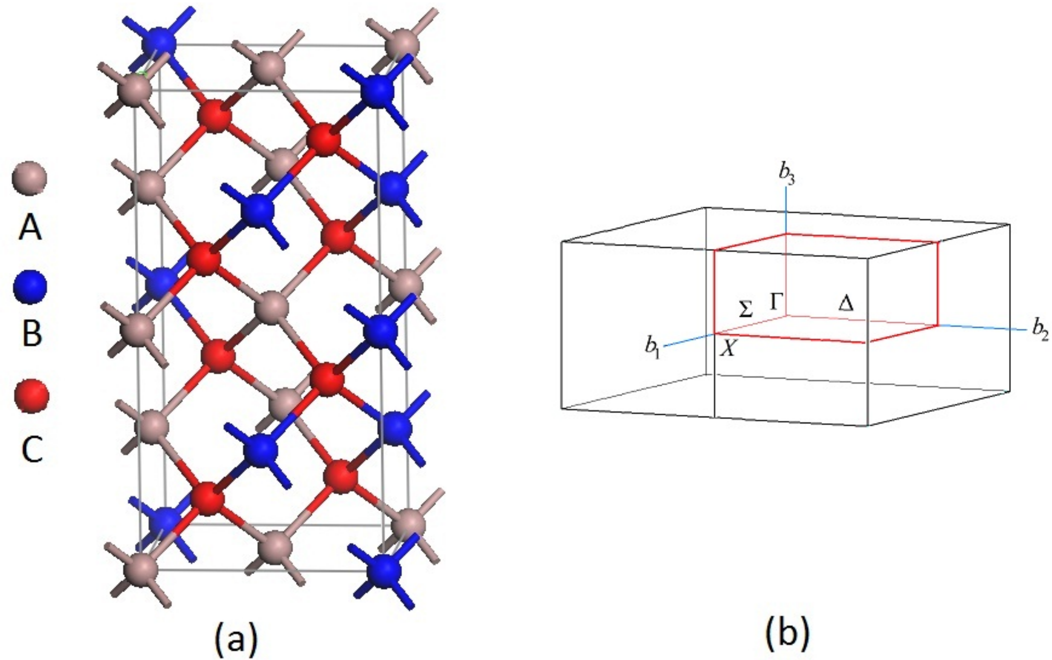

Figure 5.1 (a) The crystal structure of ternary alloy $A_xB_{1-x}C$ in Y2 ordering; (b) The Brillouin zone of the Y2 ordered superlattice.

The valence band splittings can be expressed, in terms of the energies of the top three valence band states, $E_1(\Gamma_{1v})$, $E_2(\Gamma_{2v})$ and $E_3(\Gamma_{3v})$, as follows:

$$\Delta E_{12}(\eta) = E_1(\Gamma_{1v}) - E_2(\Gamma_{2v})$$
$$\Delta E_{13}(\eta) = E_1(\Gamma_{1v}) - E_3(\Gamma_{3v}) \tag{5.1}$$

The Hopfield quasicubic model [86] states that $\Delta E_{12}(\eta)$ and $\Delta E_{13}(\eta)$ can be expressed by

$$\Delta E_{12}(\eta) = \frac{1}{2}\left[\Delta_{SO}(\eta) + \Delta_{CF}(\eta)\right] - \frac{1}{2}\left\{\left[\Delta_{SO}(\eta) + \Delta_{CF}(\eta)\right]^2 - \frac{8}{3}\Delta_{SO}(\eta)\Delta_{CF}(\eta)\right\}^{\frac{1}{2}} \tag{5.2a}$$

$$\Delta E_{13}(\eta)=\frac{1}{2}\left[\Delta_{SO}(\eta)+\Delta_{CF}(\eta)\right]+\frac{1}{2}\left\{\left[\Delta_{SO}(\eta)+\Delta_{CF}(\eta)\right]^2-\frac{8}{3}\Delta_{SO}(\eta)\Delta_{CF}(\eta)\right\}^{\frac{1}{2}} \quad (5.2b)$$

where $\Delta_{SO}(\eta)$ is the SO splitting and $\Delta_{CF}(\eta)$ is the ordering-induced Crystal-Field (CF) splitting in the absence of SO splitting. $\Delta_{CF}(\eta)$ is defined to be negative if the doubly degenerate state is below the single state.

5.3 Fingerprints of Y2 Ordering

For a spontaneously formed partially ordered semiconductor alloy with $\eta \le 1$, the physical properties $P(x,\eta)$, such as, the CF splitting $\Delta_{CF}(\eta)$, the SO splitting $\Delta_{SO}(\eta)$ and the band gap $E_g(\eta)$, at composition x can be described by [105, 106]

$$P(x,\eta)=P(x,0)+\eta^2\left[P(X_\sigma,1)-P(X_\sigma,0)\right] \quad (5.3)$$

This equation shows that the property $P(x,\eta)$ of a semiconductor alloy $A_xB_{1-x}C$ can be calculated by (I) the corresponding properties $P(x,0)$ of the random structure at the same composition x, (II) the degree of ordering η, and (III) the difference of the property, $P(X_\sigma,1)-P(X_\sigma,0)$, between the fully ordered structure and random structure at composition $X_\sigma=0.5$.

According to Equations (5.1)-(5.3), if valence band splitting, $\Delta E_{12}(\eta)$, $\Delta E_{13}(\eta)$, and band gap, $E_g(\eta)$, are known independently, for example, from electroreflectance or photoluminescence spectra, the SO splitting $\Delta_{SO}(x,\eta)$ and CF splitting $\Delta_{CF}(x,\eta)$ can be derived according to Equation (5.2). Then the theoretically calculated differences in the SO

splitting, $\left[\Delta_{SO}(1)-\Delta_{SO}(0)\right]$, CF splitting, $\left[\Delta_{CF}(1)-\Delta_{CF}(0)\right]$, and the band gap narrowing, $\Delta E_g(\eta)$, can be used to derive the ordering parameter η using Equation (5.3). On the other hand, if η is available independently from experiment, such as x-ray diffraction, one can assess the valence band splitting, $\Delta E_{12}(\eta)$, $\Delta E_{13}(\eta)$, and band gap narrowing $\Delta E_g(\eta)$.

The results of the GGA calculations are shown in Table 5.1. The following results can be found:

(I) Ordering induces a decrease in band gap and CF splitting, but an increase in SO splitting in all the five alloy systems.

(II) $\left[\Delta_{SO}(1)-\Delta_{SO}(0)\right]$ is always positive. This is due to the fact that the VBM wave function of the ordered compounds, relative to the random alloy, is more localized on the cation atom with larger atomic number [90]. For common-anion systems, the two binary constituents have similar Δ_{SO}. Therefore, the ordering induced difference $\left[\Delta_{SO}(1)-\Delta_{SO}(0)\right]$ is rather small. However, the common-cation systems (e.g., $GaAs_{0.5}Sb_{0.5}$ and $InP_{0.5}Sb_{0.5}$) have relatively larger $\left[\Delta_{SO}(1)-\Delta_{SO}(0)\right]$, because they have larger anion atom Sb. The SO splitting increases monotonically when anion atomic number increases [90].

(III) As shown in Figure 5.3a, the CF splitting $\left[\Delta_{CF}(1)-\Delta_{CF}(0)\right]$ increases in the following sequence: $Ga_{0.5}In_{0.5}As \rightarrow Ga_{0.5}In_{0.5}P \rightarrow GaAs_{0.5}Sb_{0.5} \rightarrow InP_{0.5}Sb_{0.5}$. According to the perturbation theory, Δ_{CF} is proportional to the valence band offset and inversely proportional to the difference between the symmetric energy levels of binary constituents

[70]. The band offset of a semiconductor alloy AB_xC_{1-x} refers to the relative alignment of the valence band maxima of the corresponding constituents AB and AC. This can explain the trend in CF splitting. For example, the band offset [107] between GaAs and GaSb for $GaAs_{0.5}Sb_{0.5}$ (0.57 eV) is much larger than that between GaAs and InAs for $Ga_{0.5}In_{0.5}As$ (0.06 eV). Therefore, the perturbation and CF splitting in the valence bands are larger in $GaAs_{0.5}Sb_{0.5}$ than in $Ga_{0.5}In_{0.5}As$. Note that the band offset between AlAs and GaAs for $Al_{0.5}Ga_{0.5}As$ is rather large (0.51 eV). However, it has the smallest $\left[\Delta_{CF}(1)-\Delta_{CF}(0)\right]$ at Γ point of its Brillouin zone, as shown in Table 5.1 and Figure 5.3a. This is because $Al_{0.5}Ga_{0.5}As$ compound has an indirect band in this ordering.

(IV) The band gap narrowing $\Delta E_g(\eta)$ increases with the increasing of the alloy lattice mismatch between the binary constituents, as shown in Figure 5.3b. For example, the lattice mismatch between the binary constituents for $Al_{0.5}Ga_{0.5}As$ and $Ga_{0.5}In_{0.5}As$ are 0.14% and 6.92%, respectively, smaller than that of 9.88% between InP and InSb for $InP_{0.5}Sb_{0.5}$ compound. During the formation of the lattice mismatch alloys, the structure relaxation tends to shift the charge from the long bond to the short bond and thus reduce the repulsion between the symmetric energy levels. This repulsion lowers the Γ_{1c} state and raises the Γ_{VBM} state, resulting in a band gap narrowing. In alloys with larger lattice mismatch between the constituents, more charge is transferred and therefore the band gap narrowing is larger.

5.4 Comparison with Other Orderings

Numerous studies [108-111] on the ordering of the alloy $Ga_{0.5}In_{0.5}P$ have reported the CuPt structure and, however, ignored the Y2 ordering. This is due to the similarity between CuPt

Table 5.1 GGA Calculated Optical Fingerprints of Five III-V Alloys

Alloys	$Al_{0.5}Ga_{0.5}As$	$Ga_{0.5}In_{0.5}As$	$Ga_{0.5}In_{0.5}P$	$GaAs_{0.5}Sb_{0.5}$	$InP_{0.5}Sb_{0.5}$
$\Delta E_{12}(1)$	0.009	0.129	0.091	0.188	0.357
$\Delta E_{13}(1)$	0.318	0.385	0.169	0.643	0.701
$\Delta_{SO}(1)-\Delta_{SO}(0)$	0.001	0.005	0.013	0.021	0.052
$\Delta_{CF}(1)-\Delta_{CF}(0)$	-0.004	-0.094	-0.102	-0.213	-0.385
$\Delta E_g(1)$	-0.034	-0.093	-0.202	-0.274	-0.423

The calculated properties include: valence band splitting, $\Delta E_{12}(1)$ and $\Delta E_{13}(1)$, changes in spin-orbit splitting $\left[\Delta_{SO}(1)-\Delta_{SO}(0)\right]$, crystal field splitting $\left[\Delta_{CF}(1)-\Delta_{CF}(0)\right]$ and band gap $\Delta E_g(1)$. Values are given in units of eV.

Table 5.2 Calculated Properties of Five Fully Y2 Ordered Compounds

Alloys	Structure	a	Δ_{CF}	Δ_{SO}	$b(\Delta_{SO})$
$Ga_{0.5}In_{0.5}P$	Y2	5.6599	-0.102	0.104	-0.053
$Ga_{0.5}In_{0.5}P$	CA	5.6599	0.199	0.097	-0.023
$Ga_{0.5}In_{0.5}P$	CH	5.6599	-0.015	0.093	-0.008
$Ga_{0.5}In_{0.5}P$	CP	5.6599	0.232	0.103	-0.047
$GaAs_{0.5}Sb_{0.5}$	Y2	5.8746	-0.213	0.539	-0.084
$GaAs_{0.5}Sb_{0.5}$	CA	5.8927	0.085	0.549	-0.10
$GaAs_{0.5}Sb_{0.5}$	CH	5.8922	-0.013	0.521	-0.01
$GaAs_{0.5}Sb_{0.5}$	CP	2.8974	0.230	0.605	-0.33
$Al_{0.5}Ga_{0.5}As$	Y2	5.5659	-0.004	0.316	-0.005
$Ga_{0.5}In_{0.5}As$	Y2	5.8558	-0.094	0.343	-0.019
$InP_{0.5}Sb_{0.5}$	Y2	6.1740	-0.385	0.467	-0.208

Results of CA, CH and CP orderings of GaInP and GaAsSb are also listed for comparison. The units are Å for lattice constant a and eV for crystal field splitting Δ_{CF}, spin-orbit splitting Δ_{SO} and its bowing parameter $b(\Delta_{SO})$.

and Y2 orderings. They are built from the same (001) plane and differ only in the stacking of the subsequent planes. In fact, some reports [112, 113] have mistakenly attributed the extra features in the spectra originating from Y2 ordering into CuPt ordering. Moreover, the small difference between the formation enthalpies of CA and Y2 ordering in some alloys may also cause the co-existence of CA and Y2 orderings [99]. In view of these facts, here the optical fingerprints of Y2 ordering are compared here with those of CA, CP and CH structures. Results are listed in Table 5.2. The followings are found:

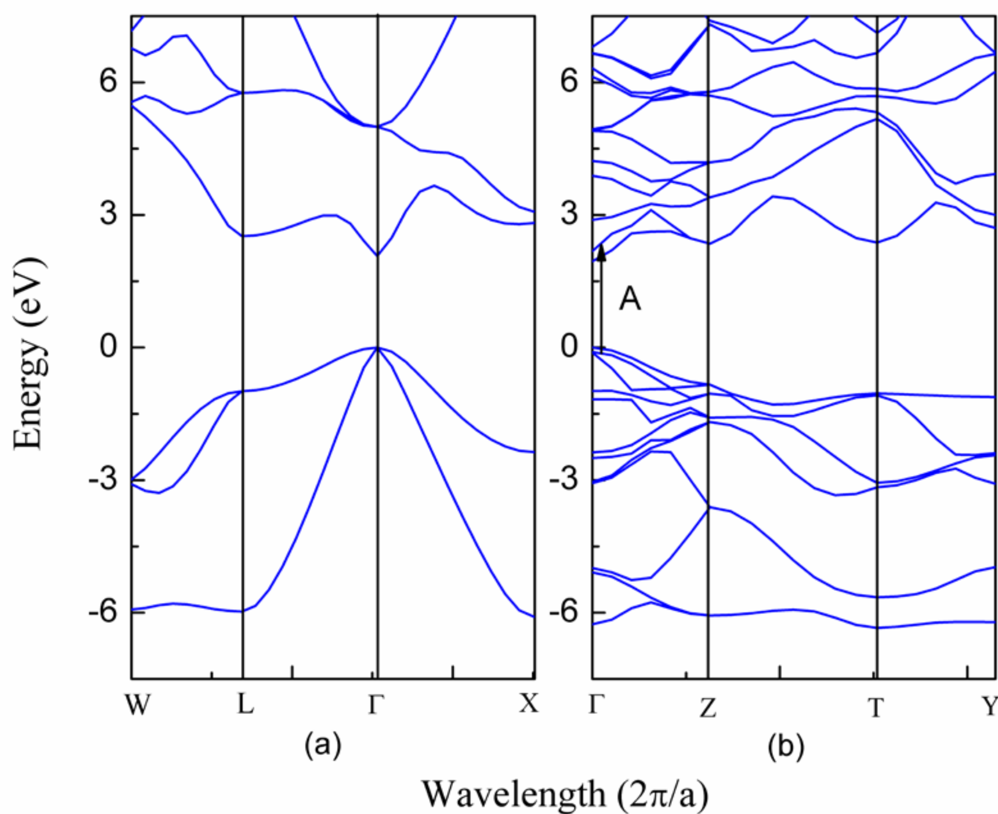

Figure 5.2 The band structures for the (a) random and (b) Y2 ordered $Ga_{0.5}In_{0.5}P$ alloy are plotted along the high symmetry lines in the Brillouin zone. The arrow A denotes the interband transition responsible for the anomalous peak at 2.2 eV in the electroreflectance spectra.

(I) Relative to other orderings, Y2 ordering has large and negative CF splitting Δ_{CF}. As it has been highlighted before, the ordering separates the triply degenerate states in random alloy into a single state and a doubly degenerate state. In CA and CP orderings, the doubly degenerate state is above the single state, resulting in a positive CF splitting. However, in CH and Y2 ordering, the doubly degenerate state is below the single state, resulting in a negative CF splitting. In Y2 ordering, the doubly degenerate state split further into two single states. Due to the smaller difference in the symmetric energy levels of the binary constituents in Y2 ordering than in CH ordering, the CF splitting is larger in Y2 ordering.

(II) The bowing parameter of SO splitting is negative in Y2 ordering. SO splitting reflects the way that bonding in solids redistributes the charge around the atomic cores of the constituents [38]. The sign of the SO splitting bowing parameter reflects the alloy environment and acts to enhance or diminish the magnitude of SO splitting beyond the linear average of the constituents. The calculation shows that the formation of Y2 ordering enhances the magnitude of Δ_{SO} and yields a negative SO splitting bowing parameter $b(\Delta_{SO})$. This is consistent with the result of CdS_xTe_{1-x} in the previous chapter and the upward concave bowing is attributed to the intraband *p-p* coupling.

5.5 Comparison with Experiments

Using electroreflectance spectroscopy method, Kurtz [100] found an anomalous peak at about 2.2 eV in spontaneously ordered $Ga_{0.5}In_{0.5}P$ alloy. This peak is attributed to the *X* point folding to Γ point in the first Brillouin zone due to the Y2 ordering. According to the calculated band structures, this peak corresponds to the transitions (denoted as A in Figure

5.2b) from the second and third VBM states to the second conduction band minimum (CBM) state. The calculated value for transition A is 2.27 eV, in good agreement with the experimental result of 2.2 eV. The band diagram, produced by Kurtz [100], using virtual crystal approximation method, suggests that Y2 ordering in $Ga_{0.5}In_{0.5}P$ shall result in a band gap narrowing of 0.17 eV. This value is close to the GGA calculated data of 0.202 eV. Using transmission electron microscopy and photoluminescence methods, Gomyo et al. [98] reported a band gap narrowing of 0.05 eV for $Ga_{0.5}In_{0.5}P$ due to the partial Y2 ordering. According to the calculations, the sample should have ordering η around 0.5.

The calculated values of valence band splittings, $\Delta E_{12}(1)$ =0.091 eV and $\Delta E_{13}(1)$=0.169 eV, for fully Y2 ordered $Ga_{0.5}In_{0.5}P$ are consistent with the results, 0.10 eV and 0.15 eV, reported by Lee et al. [114]. The calculated values of CF splitting and SO splitting are also in good accord with the available experimental results. For example, the reported [115] SO splitting for $Ga_{0.5}In_{0.5}As$ are 0.345 eV and 0.33 eV while the calculations obtained 0.343 eV. The calculated bowing parameter of SO splitting for $Ga_{0.5}In_{0.5}P$ is -0.053 eV. This value is very close to the measured result of -0.05 eV using the electroreflectance and wavelength modulation methods [84].

Recently, Wu et al. [102] reported the observation of Y2 ordering in $InP_{0.52}Sb_{0.48}$. Using reciprocal space mapping and extended x-ray absorption fine structure method, they found the structure parameter *c/a*=1.009. This is considerably larger than the predicted value of 0.997 (not listed) for $InP_{0.5}Sb_{0.5}$. However, they find that the strong distorted In-P and In-Sb bonds prevent the crystal lattice from complete relaxation. This may explain the difference between the calculated result and their measured value.

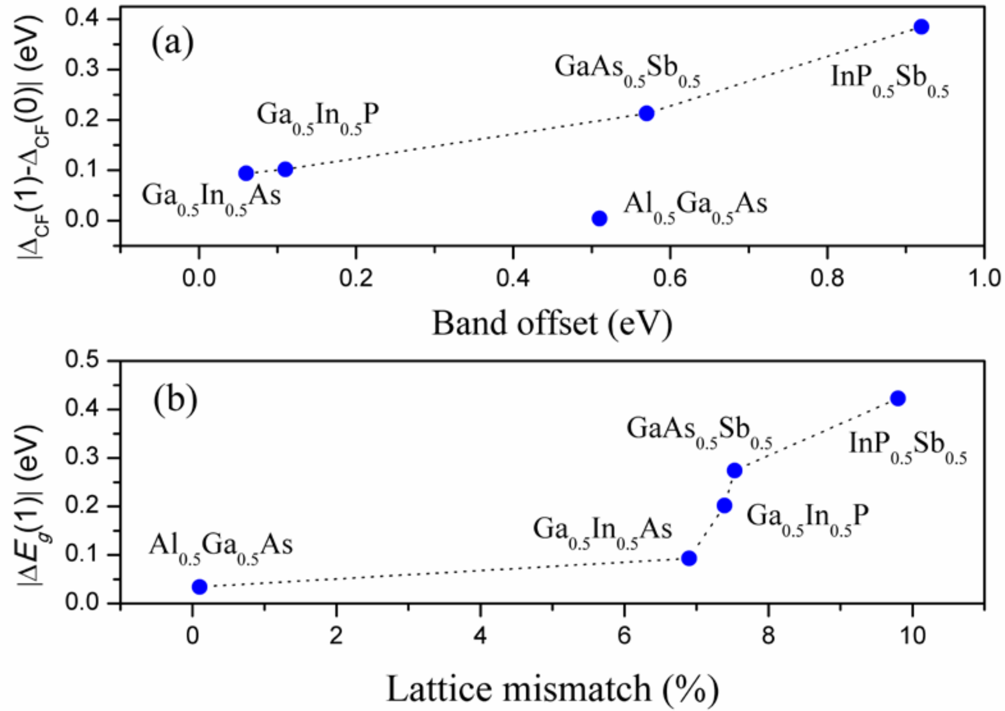

Figure 5.3 (a) Variation of the crystal field splitting $\left[\Delta_{CF}(1)-\Delta_{CF}(0)\right]$ with the band offset between alloys' binary constituents. (b) Variation of the band gap narrowing $\Delta E_g(1)$ with the alloys lattice mismatch.

5.6 Summary

The chapter has calculated the Y2 ordering induced changes in the optical fingerprints, including crystal field splitting, spin-orbit splitting, band gap and valence band splittings, for $Al_xGa_{1-x}As$, $Ga_xIn_{1-x}As$, $Ga_xIn_{1-x}P$, $GaAs_xSb_{1-x}$ and InP_xSb_{1-x} using first-principles calculations. These values for the five materials are provided as a function of the degree of long range order η. For the partially ordered samples, the trends of the changes in the crystal field splitting and band gap narrowing are explained. The change of spin-orbit splitting is found to be positive and small. For the fully ordered samples, Y2 ordering is

compared with other orderings. It is found that Y2 has a large and negative crystal field splitting and negative spin-orbit bowing parameter. The calculated data in this chapter can be useful in analyzing experimental results and deriving the ordering parameters of partially ordered samples.

CHAPTER 6

PRESSURE DEPENDENCE OF ENERGY GAP OF III-V & II-VI TERNARY SEMICONDUCTORS

6.1 Theoretical Background

Previous chapters have been dedicated to the studies of all fundamental (i.e., mechanical, electronic and optical) properties of III-V & II-VI binary and ternary semiconductors. During the fabrication of semiconductor devices and the industrial applications of sensors, the pressure dependence of the energy gaps of ternary alloys is always of great interest. In general, there has been very little data on the pressure dependence of the energy gap of ternary semiconductors and even within the limited available experimental data, there is a significant variation. For example, the pressure coefficient of the band gap of $Ga_{0.5}In_{0.5}P$, reported by Hakki and coworkers [116] is 13 meV/kbar, in contrast with the 8.4 meV/kbar obtained by Chen et al. [117]. Thus a theoretical approach is required to analyze the problem.

Except the first-principles calculations, empirical approaches have been developed to address some of these problems. The transition from binary compound semiconductors to ternary compound semiconductors requires the understanding of the bowing parameter [118]. As given in Chapter 3, the expression for the bowing parameter, c_{ABC}, of ternary compound AB_xC_{1-x} can be rewritten as:

$$E_g\left(x\right) = xE_g^{AB} + \left(1-x\right)E_g^{AC} - c_{ABC}x\left(1-x\right) \tag{6.1}$$

where, E_g^{AB} and E_g^{AC} are the energy gaps of binary compounds AB and AC, respectively. Hill [118] has ascribed the physical meaning of the bowing parameter to the nonlinear

dependence of the crystal potential on the properties of the component ions and derived the following expression:

$$c_{ABC} = \frac{Zer_{BC}}{4\pi\epsilon_0}\left[\frac{1}{r_B} - \frac{1}{r_C}\right]^2 exp\left(-\frac{1}{2}sr_{BC}\right) \tag{6.2}$$

in which, $Z = Z_B = Z_C$ is the valence number of ions B and C, r_B and r_C are the covalent radii of B and C, $r_{BC} = r_B + r_C$ and $s = 0.25$ is a screening constant. Differentiating Equation (6.2) with respect to pressure, Hill and Pitt [119] obtained the following expression:

$$\frac{dc_{ABC}}{dP} = \frac{1}{2\sqrt{3}}\frac{c_{ABC}}{r_B - r_C}\left[\frac{r_C}{r_B}a_{AB}\chi_{AB} - \frac{r_B}{r_C}a_{AC}\chi_{AC}\right] \tag{6.3}$$

where, a_{AB}, a_{AC} and χ_{AB}, χ_{AC} are lattice constants and compressibilities of compounds AB and AC, respectively. Based on this model, Hill and Pitt [119] calculated the pressure coefficients of the bowing parameters for a number of ternary semiconductors. However, in order to calculate the pressure dependent energy gap of ternary semiconductor AB_xC_{1-x} using this model, one has to use the experimental data for band gap pressure coefficients of binary compounds AB and AC, because, according to Equation (6.1):

$$\frac{dE_g(x)}{dP} = x\frac{dE_g^{AB}}{dP} + (1-x)\frac{dE_g^{AC}}{dP} - \frac{dc_{ABC}}{dP}x(1-x) \tag{6.4}$$

Van Vechten [120, 121] proposed a dielectric theory for tetrahedral compounds based on Phillips' spectroscopic theory of electronegativity difference [38]. The theory was successfully applied and generalized to a variety of areas in materials science,

including, band structures, alloy bowing parameters, elastic constants and so forth. Camphausen et al. [122] used this model to calculate the pressure coefficients of band gaps of nineteen binary semiconductors and appeared to yield good agreement between theoretical expectations and experimental results.

In this chapter, the Van Vechten's theory is modified to calculate the pressure dependence of energy gap of a number of group III-V and II-VI zincblende ternary semiconductors. The calculated results are compared with available data in the literature. The trends in the variations of the band gap and its pressure dependence will be discussed.

6.2 Modeling Pressure Dependent Band Gap of Ternary Alloys

In Van Vechten's dielectric theory [120, 121], the energy gap between the minimum conduction band and the maximum valence band, if the effect of *d*-state core is involved, is expressed as:

$$E_g^{'} = \left[E_{g,h} - \left(D_{av} - 1\right)\Delta E_g\right]\left[1 + \left(C / E_{g,h}\right)^2\right]^{\frac{1}{2}} \tag{6.5}$$

In this expression, $E_g^{'}$ is used to differentiate from the energy gap in Equation (6.1). $E_{g,h}$ is the homopolar gap for transition corresponding to particular energy gap and is assumed to be a power function of the nearest neighbor distance r given by $E_{g,h} \propto r^{s_1}$, where $s_1 = -2.75$. D_{av} is the factor that describes the lowering of *s*-like conduction band states caused by the effect of *d* states and the value is the skewed average of D_{av} values of the crystals containing the constituent atoms and the atom from the same row in the periodic table. For the first three rows in the periodic table, D_{av} is unity and Equation (6.5)

reduces to Phillips' pseudopotential theory [38]. ΔE_g is the correction related factor given by $\Delta E_g \propto r^{s_2}$, where $s_2 = -5.07$. C is the heteropolar gap produced by the anti-symmetric potential in the corresponding binary compounds. For binary compound AB, C is given by [120]:

$$C = b_p e^2 \left[\frac{Z_A}{r_A} - \frac{Z_B}{r_B} \right] exp\left(-k_s r\right) \tag{6.6}$$

For a ternary compound AB_xC_{1-x}, it can be generalized as follows:

$$C = b_p e^2 \left[\frac{Z_A}{r_A} - x\frac{Z_B}{r_B} - \left(1-x\right)\frac{Z_C}{r_C} \right] exp\left(-k_s r\right) \tag{6.7}$$

where, the pre-factor b_p is constant around 1.5, k_s is the radius-dependent Thomas-Fermi screening wave number, $r = r_A + x r_B + \left(1-x\right) r_C$ is the nearest neighbor distance.

From Equations (6.5) – (6.7), the pressure coefficients of the energy gap can be given by:

$$\begin{aligned} \frac{dE_g^{'}}{dP} = & \left[1+\left(C/E_{g,h}\right)^2\right]^{\frac{1}{2}} \left[\frac{dE_{g,h}}{dP} - \Delta E_g \frac{d\left(D_{av}-1\right)}{dP} - \left(D_{av}-1\right)\frac{d\Delta E_g}{dP} \right] \\ & + \left[\frac{E_g}{1+\left(E_{g,h}/C\right)^2} \right] \left[\frac{1}{C}\frac{dC}{dP} - \frac{1}{E_{g,h}}\frac{dE_{g,h}}{dP} \right] \end{aligned} \tag{6.8}$$

This Equation (6.8) is the same as the one derived by Camphausen et al. [122] and is applicable to both binary and ternary compounds. Camphausen et al. have proved that, even in non-ionic materials, $\frac{dC}{dP}$ is sufficiently small and can be considered to be

negligible while compared with the other terms in the expression. They further pointed out the expression for the correction term to be $D_{av} - 1 \propto r^{y}\left(1 - f_{i}\right)^{z}$, in which, f_i is the Phillips' ionicity [38] as introduced in Chapter 2. E_h is the average homopolar energy gap given as $E_h \propto r^{s_3}$, where $s_3 = -2.48$. s_1, s_2 and s_3 are constants determined from experimental values of two group IV elements [121]. Camphausen et al. [122] found that $y = 13$ and $z = 2.4$ by fitting the pressure coefficient of the energy gap of Ge.

In their later study, Van Vechten and Bergstresser [123] pointed out that the bowing parameter c_{ABC} of ternary compound AB_xC_{1-x} comprises of two parts. The first part, intrinsic bowing parameter c_i, originates from the variation of the average crystal potential under virtual crystal approximation which assumes periodic potential in the crystal. If one calculates the energy difference using Equation (6.5), the result, $E_g^{'ABC}$, will be different from the compositionally weighted average energy of the corresponding two binary compounds. This difference is the intrinsic bowing parameter. Another part, c_e, the extrinsic bowing parameter, arises from the real short range aperiodicity, and is the small deviation of the real potential from virtual periodic potential. In terms of this theory, the real energy gap in Equation (6.5) becomes the following:

$$E_g\left(x\right) = E_g^{'ABC} - c_e x\left(1 - x\right) \tag{6.9}$$

where, the intrinsic bowing parameter is included in the first term; the extrinsic bowing parameter is proposed by Van Vechten and Bergstresseras [123] as:

$$c_e = \frac{C_{BC}^2}{A} \tag{6.10}$$

$$C_{BC} = b_p e^2 \left| \frac{Z_B}{r_B} - \frac{Z_C}{r_C} \right| exp\left(-k_s r\right) \tag{6.11}$$

In the above Equation (6.10), the bandwidth parameter A is a constant for all compounds and found to be 0.98eV by fitting the extrinsic bowing parameter with C_{BC} for the ZnSTe system. C_{BC} is the fluctuation of the actual potential in the virtual crystal approximation which is different from C in Equation (6.7).

By summarizing the aforementioned equations, the following expression can be obtained for the pressure dependent band gap of ternary semiconductor AB_xC_{1-x}:

$$\begin{aligned} \frac{dE_g(x)}{dP} = \frac{1}{3B} \Bigg\{ & \left[1+\left(C/E_{g,h}\right)^2\right]^{\frac{1}{2}} \left[s_1 E_{g,h} - \left(D_{av}-1\right)\Delta E_g \left(y + \frac{2zs_3}{1+\left(E_h/C\right)^2} + s_2 \right)\right] \\ & - \frac{s_1 E_g(x)}{1+\left(E_{g,h}/C\right)^2} - 2x(1-x)c_e r \left(\frac{1}{b_p}\frac{db_p}{dr} - \frac{k_s}{4} - \frac{1}{r} \right) \Bigg\} \end{aligned} \tag{6.12}$$

In this expression, the first two terms on the right hand side stem from the pressure dependence of the band gap in virtual crystal approximation. The last term is the pressure dependence of the extrinsic bowing parameter. B is the bulk modulus of the ternary compound semiconductor.

Table 6.1 Calculated Properties of III-V & II-VI Ternary Semiconductors at Composition 0.5

Alloy	r [120] (A)	D_{av} [121]	C (eV)	c_e (eV)	c_{ABC} (eV)	c_{ABC} (exp) [124](eV)	f_i	E_g (eV)	E_g (exp) [125] (eV)	$\frac{dc_{ABC}}{dP}$ (meV/kbar)	$\frac{dc_{ABC}}{dP}$ [119] (meV/kbar)	$\frac{dE_g}{dP}$ (meV/kbar)	$\frac{dE_g}{dP}$ (exp) (mev/kbar)
GaPAs	2.404	1.183	3.090	0.186	0.399	0.175-0.21 0.54	0.319	2.217	2.048 2.15[126]	0.523	0.4	9.005	
GaPSb	2.508	1.223	2.327	1.647	2.768	2.7	0.247	1.244	0.845[77] 1.06	3.486	2.5	9.736	
GaAsSb	2.552	1.266	2.159	0.802	1.093	1.0-1.2 1.42-1.44	0.235	1.031	0.81[127] 0.763	2.726	2.5	11.400	12.25[128]
InPAs	2.586	1.308	3.445	0.119	0.174	0.09-0.38	0.455	1.039	0.819	-0.620	0.3	10.623	
InPSb	2.678	1.345	2.725	1.294	1.814	1.2-2.0	0.384	0.478	0.48[129] 0.36	3.423	1.2	11.277	
InAsSb	2.712	1.388	2.758	0.774	0.89	0.58-0.7	0.405	0.319	0.12	4.505	-1.0	12.271	
GaInP	2.456	1.203	3.333	0.315	0.737	0.39-0.76	0.378	2.026	1.98[126] 1.9 2.19[130]	-2.026	0.3	8.939	8.4[117] 8.8[131] 13[116]
GaInAs	2.534	1.288	3.198	0.307	0.527	0.32-0.6	0.395	1.056	0.813[132] 0.75	1.165	0.3	10.880	10.95[133]
GaInSb	2.730	1.366	1.827	0.177	0.283	0.36-0.43	0.235	0.587	0.34 0.43[134]	1.649	-0.6	13.894	16[135]
AlGaN	1.964	1.070	10.624	0.097	4.051	0.25-1.78	0.670	8.358	4.48[136] 3.12[137]	-1.131		3.607	3.24[137] 4[136]
AlGaP	2.361	1.070	3.215	0.009	-0.031	0, 0.49	0.317	4.051	3.34 2.38[138]	-0.339		5.608	
AlGaAs	2.441	1.173	2.795	0.014	0.0126	-0.127-1.183	0.293	2.337	2.94 2.158[139]	0.654		8.887	9.15[140] 10.85[141]
ZnSSe	2.398	1.153	5.885	0.349	0.506	0.456-0.68	0.627	3.743	3.08	3.118	0.8	6.180	
ZnSTe	2.493	1.169	4.905	2.476	3.144	2.4-3[142] 3.75[125]	0.586	2.626	2.36[143] 2.061	7.387	6.6	5.633	

Table 6.1 Calculated Properties of III-V & II-VI Ternary Semiconductors at Composition 0.5 (Continued)

Alloy	r [120] (A)	D_{av} [121]	C (eV)	c_e (eV)	c_{ABC} (eV)	c_{ABC} (exp) [124](eV)	f_i	E_g (eV)	E_g (exp) [125] (eV)	$\frac{dc_{ABC}}{dP}$ (meV/kbar)	$\frac{dc_{ABC}}{dP}$ [119] (meV/kbar)	$\frac{dE_g}{dP}$ (meV/kbar)	$\frac{dE_g}{dP}$ (exp) (mev/kbar)
ZnSeTe	2.549	1.191	4.623	1.041	1.189	1.23-1.7[142]	0.584	2.606	2.3[144] 2.12	4.658	1.6	6.920	7.6[145]
CdSSe	2.590	1.247	6.416	0.291	0.399	0.53[142]	0.745	2.670	2.25[146] 1.95	-0.997	1.6	5.576	4-6[147]
CdSTe	2.674	1.265	5.511	2.345	2.696	1.73-1.84[142]	0.716	1.810	1.58	6.212	2.3	4.751	6.2[148]
CdSeTe	2.722	1.287	5.159	1.001	1.04	0.755[142] 0.87[142]	0.708	1.864	1.047 1.48[149]	2.453	0.3	6.221	
CdZnS	2.442	1.179	6.524	0.170	0.491	0.3,0.6[142] 0.83[125]	0.693	3.611	2.89	-0.809		5.792	5.3[150]
CdZnSe	2.546	1.223	5.801	0.136	0.36	0.3,0.35[142] 0.387[125]	0.687	2.775	2.1	0.584		6.579	
CdZnTe	2.725	1.255	4.086	0.090	0.197	0.153-0.463[142]	0.604	2.113	1.85[151] 1.7	-0.646		8.356	

r is the nearest neighbor distance. D_{av} is the *d*-state effect parameter. C is the heteroplar energy gap. c_e is the external bowing parameter. f_i is the ionicity. c_{ABC} and $\frac{dc_{ABC}}{dP}$ is the bowing paremeter and its pressure coefficient. E_g and $\frac{dE_g}{dP}$ is the energy gap and its pressure coefficient.

Table 6.2 Comparison between Calculated Pressure Coefficients of Band Gap for Some Ternary Compounds for Compositions ≠ 0.5 and Al-compounds

	x	$\frac{dE_g}{dP}$ (meV/kbar)	$\frac{dE_g}{dP}$ (exp)[152] (meV/kbar)
$Cd_xZn_{1-x}Se$	0	7.564	7.2-7.5, 7.0[153]
	1	5.886	5.8, 5.5[140]
	0.73	6.586	3.54[154]
ZnS_xTe_{1-x}	0	8.606	10.5[155], 11.5
	1	6.355	5.8, 6.4[153],6.7[156]
	0.3	5.732	6.2[157]
$GaAs_xSb_{1-x}$	0	13.552	14.0
	1	10.61	8.5-12.6
	0.88	11.516	9.5[158]
$Al_xGa_{1-x}N$	0	5.224	3.6[140],4.0[159]
	1	1.423	4.7[140]
	0.5	3.607	3.24[137], 4[136]
$Al_xGa_{1-x}P$	0	7.662	9.7
	1	3.385	11.1[140]
	0.5	5.608	
$Al_xGa_{1-x}As$	0	10.61	8.5-12.6
	1	7.49	10.2
	0.5	8.887	9.15[140], 10.85[141]

6.3 Results and Discussion

The bowing parameter, energy gap and their pressure coefficients of III-V and II-VI ternary semiconductors, calculated from the above theory, are listed in Table 6.1 together with other parameters that are relevant for the present calculations.

6.3.1 Dependence of Pre-factor b_p on Pressure

In Van Vechten's dielectric theory [120], the pre-factor, b_p, is introduced to balance the overestimate of the Thomas-Fermi effect on dielectric screening at short distances. The dependence of this pre-factor on pressure, i.e., $\frac{r}{b_p}\frac{db_p}{dr}$, was proved to be approximately

2.0-2.5 for materials with ionicity larger than 0.93, while for partial covalent materials ($f_i < 0.93$), this dependence is much weaker. Since for all the ternary compounds considered in this chapter, ionicity is less than 0.72, $\frac{1}{b_p}\frac{db_p}{dr} = 0$ is assumed throughout the entire calculations.

6.3.2 Bulk Modulus of Ternary Alloys

As has been studied in Chapter 2, the bulk modulus of binary and ternary semiconductors can be expressed as:

$$B = kr^{-3.48} \tag{6.13}$$

In order to obtain the bulk modulus of ternary semiconductors, Equation (6.13) is fitted to all the available experimental data of binary compounds in the same group as those of the ternaries. For group III-V ternary semiconductors, it is found that the constant coefficient $k = 1726$ while for group II-VI, $k = 1491$. From the above equation, it is seen that the bulk modulus is inversely proportional to the nearest neighbor distance.

6.3.3 Trends in Pressure Coefficients of Energy Gap

For the common cation system, for example, GaInP, GaInAs, GaInSb (Ga:In::0.5:0.5), the pressure coefficient of the band gap increases with increasing nearest neighbor distance (Columns 13 and 2, respectively, in Table 6.1). In Equation (6.12), the pressure coefficient of the band gap is inversely proportional to the bulk modulus which according to Equation (6.13), is inversely proportional to the nearest neighbor distance. Therefore, the pressure coefficient of the band gap will increase with increasing nearest neighbor distance due to the decrease in bulk modulus. In general, pressure will cause a dilation of the lattice and

will lead to changes in its potential energy resulting in overlap of the energy levels which will subsequently lead to change in the energy gap. However, for the common-anion system, this trend is not so significant. For instance, the pressure coefficient increases in group III-V in the following order of common group V elements: (GaPAs, InPAs), (GaPSb, InPSb), (GaAsSb,InAsSb) while it decreases in group II-VI in the following order of common group VI elements: (ZnSSe, CdSSe), (ZnSTe, CdSTe), (ZnSeTe,CdSeTe). As discussed earlier, the decrease in bulk modulus will result in an increase in the pressure coefficient of the energy gap. In the studies on the predicted pressure coefficient of the energy gap, Wei and Zunger [140] have found that the *s-s* and *p-p* coupling will enhance while *p-d* coupling will reduce the pressure coefficients of the energy gap. Thus, it may be concluded that the trend in group III-V common-anion system is because the effect of *s-s*, *p-p* coupling and bulk modulus is stronger than the effect of *p-d* coupling, and vice versa for group II-VI common-anion system.

Another trend is that the pressure coefficient of the band gap decreases with increasing ionicity (Columns 13 and 8, respectively, in Table 6.1). In order to verify this correlation, comparison is made amongst compounds with similar bulk modulus due to similar nearest neighbor distance (Column 2 in Table 6.1), for example, GaPAs (2.404Å) with ZnSSe (2.398Å). For GaPAs and ZnSSe, the corresponding ionicities are 0.319 and 0.586 and pressure coefficients are 9.005 and 6.18 meV/kbar, respectively. Similar trends are also found in other comparisons. Combining these results with the above analysis, this trend also indicates that coupling effects could be reflected from ionicity.

Exceptions to the trend in the variation of the pressure coefficient of energy gap with ionicity and nearest neighbor distance appear in zinc and cadmium chalcogenide

common anion systems. This is due to the large bowing parameter (Column 6 in Table 6.1) and its pressure coefficient (Column 11 in Table 6.1) of ZnSTe and CdSTe. The bowing parameter pressure coefficient is 7.387 meV/kbar in ZnSTe compared with 3.118 meV/kbar and 4.658 meV/kbar in ZnSSe and ZnSeTe systems respectively. Similarly, the bowing parameter pressure coefficient for CdSTe is 6.212 meV/kbar compared with -0.997 meV/kbar for CdSSe and 2.453 meV/kbar for CdSeTe. These exceptions reflect the importance of bowing parameters in determining the electronic properties of ternary compounds and the invalidity of the well accepted linear interpolation rule which can be used to obtain the physical properties of ternary compounds from the linear interpolation of two binary compounds.

6.4 Comparison with Experiments

The agreement between the calculated results and the experimental data are generally good. All the calculations, presented in this chapter, have been performed for composition $x = 0.5$. However, some experimental values are only available for other compositions. These experimental values are listed and compared with the calculated results for the corresponding compositions in Table 6.2. For example, Zhao et al. [154] found that the pressure coefficient of band gap for $Cd_{0.73}Zn_{0.27}Se$ is 3.54 meV/kbar and the calculated value at this composition is about 6.586 meV/kbar. This difference may arise from the wurtzite structure of their experimental sample while all the calculations assume zincblende structures. The mechanism of the real difference of structure in determining the pressure coefficients is not yet theoretically well understood. However, the available data show that the pressure coefficient of wurtzite structure is generally less than that of zincblende structure. For example, in this case, experimental pressure coefficient of

wurtzite ZnSe is around 4.5 meV/kbar [160] while for zincblende ZnSe, the available data is 7.0-7.5 meV/kbar [152, 153] and the calculated result is 7.564 meV/kbar. The pressure coefficient of wurtzite CdSe is around 4.3 meV/kbar [161] and for zincblende structure is around 5.8 meV/kbar [140, 152] and the calculation shows 5.886 meV/kbar. Based on this analysis, the accuracy of the experiment by Zhao et al. is doubtable for their band gap pressure coefficient of wurtzite CdSe is 2.84±0.6 meV/kbar, much smaller than the generally accepted results. From the perspective of the above analyzed trends with respect to nearest neighbor distance and ionicity in the order: CdZnS, CdZnSe, CdZnTe, the result is also more reasonable. For ternary compound $ZnS_{0.3}Te_{0.7}$, Fang et al. [157] found the band gap pressure coefficient is about 6.2 meV/kbar. From their graphs, the pressure coefficient is almost invariable with respect to composition. This study calculates the system at $x = 0.3$ and finds that the value is 5.732 meV/kbar which is very close to their data within experimental uncertainty. Moreover, the band gap pressure coefficient for $GaAs_{0.88}Sb_{0.12}$ is reported by Prins et al. [158] as 9.5 meV/kbar and the calculated result shows value of 11.516 meV/kbar, close to GaAs.

In Table 6.2, the calculated AlGaN pressure coefficient 3.607 meV/kbar is very close to the reported experimental value 3.24 meV/kbar and 4 meV/kbar. However, the calculated binary AlN coefficient 1.423 meV/kbar, is much smaller than Wei's [140] first-principles calculations 4.7 meV/kbar. Similarly, the value for AlP is 3.385 meV/kbar compared with their 11.1 meV/kbar and for AlAs, this calculation yields 7.49 meV/kbar while the available experiment [152] value is 10.2 meV/kbar. The reason for this discrepancy has not yet been found.

A close investigation on the calculated energy gaps (Column 10 in Table 6.1) will find that they are in general larger than the experimental values and this discrepancy is even larger for Group II-VI than Group III-V. One possible origin for this result is the expressions of $E_{g,h}$ and ΔE_g in Equation (6.5) are obtained by fitting to the experimental data of non-ionic group IV materials. Similar as in the trend of the pressure coefficients, the data show that energy gap, in general, increases with decreasing nearest neighbor distance and increasing ionicity. Since the ionicity increases from group IV to III-V to II-VI, the calculated band gap values of these III-V and II-VI ternary semiconductors will be enhanced and larger than experimental values. The ionicity of group III-V ternary compounds is in the range 0.23-0.45, and the difference between the calculated results and experimental data is approximately in the range of 0-0.25 eV. The ionicity of group II-VI ternary compounds is around 0.58-0.72, and correspondingly, the energy gap discrepancy is about 0.3-0.8 eV.

The model proposed by Hill and coworkers has been discussed in the first section. Their calculated results for bowing parameter pressure coefficients are listed in Table 6.1 (Column 12) and comparisons show that their results are generally much smaller than those in the present work. This may be because they take the screening wave number in Equation (6.2) as a constant 0.25 which may not affect the accuracy of calculating the bowing parameter but will certainly affect the accuracy of the pressure coefficient of bowing parameter. It is also noted that they take a set of approximations in their calculations which may also result in the difference. The reason that they could fit their results to GaInP system is because the pressure coefficient of bowing parameter in this system as described

in Equation (6.4) is much smaller than its binary band gap coefficients which the authors took from experiments.

6.5 Temperature Coefficients of Ternary Alloys

Methods that are similar to this theory cannot be applied to temperature coefficients of ternary compounds by relating them to thermal expansion coefficients. This is because the temperature coefficient could be expressed as two terms: the effect of volume expansion which could be similarly derived from this theory and explicit temperature coefficient at constant volume which has to be calculated by other means. Yu and Cardona [162] have shown that the first term only contributes less than 20% of the total temperature coefficients.

6.6 Summary

The pressure dependence of the energy gap of a series of group III-V & II-VI ternary semiconductor compounds have been calculated in terms of a generalized expression of Van Vechten's dielectric theory. Good agreement is obtained between the calculated values with the available experimental data and other calculated results. The calculation shows the following: (I) The pressure coefficient of the energy gap increases with increasing nearest neighbor distance in common cation systems; (II) The pressure coefficient of the energy gap decreases with increasing ionicity; (III) The energy gap increases with decreasing nearest neighbor distance and increasing ionicity; (IV) The theory shows certain discrepancy in calculating energy gap due to its built-in assumptions.

CHAPTER 7

ELECTRONIC AND OPTICAL PROPERTIES OF I_2-II-IV-VI_4 QUATERNARY SEMICONDUCTORS

7.1 Theoretical Background

One of the most important applications of multi-ternary semiconductor alloys is the solar cell. The history of solar cell development is the history of searching for materials that can be used to produce better solar cells. These materials include Si, GaAs, CdTe and $CuIn_{1-x}Ga_xSe_2$ (CIGS). CIGS is thought to be the only substitute for Si solar cell due to its high efficiency. However, CIGS contains expensive element Indium (In) and also its window layer CdS contains toxic element Cadmium (Cd).

Recently, the I_2-II-IV-VI_4 series of quaternary chalcogenide semiconductors are of broad interest for their potential applications as photovoltaic absorbers [163-167], optoelectronic and thermoelectric materials [168-170]. For instance, Cu_2ZnSnS_4 based thin film solar cells have reached a conversion efficiency of over 6.7% [164]. Recently, a non-vacuum, slurry-based coating method and particle-based deposition, enabled the fabrication of $Cu_2ZnSn(S, Se)_4$ devices with over 9.6% efficiency [170]. Compared to the conventional CIGS absorbers, Cu_2ZnSnS_4 and $Cu_2ZnSnSe_4$ compounds only contain abundant, inexpensive and nontoxic elements and their band gaps are close to 1.5 eV, which is ideal for solar cell applications.

The wide applications increase the interest of studying many other members in the I_2-II-IV-VI_4 family, such as, the Ge-compounds: Cu_2ZnGeS_4, $Cu_2ZnGeSe_4$ and $Cu_2ZnGeTe_4$. In experiments, the physical properties [24, 171-174], such as, crystal orderings and lattice constants, of these compounds have been studied using x-ray diffraction method. Transmission [175] and absorption measurements [176] are conducted

to study the band gaps. Recently, the optical constants of Cu_2ZnGeS_4 have been reported by ellipsometry measurements [177]. In theoretical work, the structural and electronic properties of some compounds have been studied using first-principles calculations [178, 179]. However, the optical properties of these compounds have not yet been systematically addressed.

In this chapter, the electronic and optical properties of Cu_2ZnGeX_4 (X=S, Se and Te) quaternary compounds will be investigated through first-principles calculations. The electronic structures and density of states will be firstly calculated because it is known that the structures in the optical spectra are directly related to the band structure of the material itself. Then, the optical properties will be presented, including the dielectric function, refractive index, optical reflectivity and absorption spectra. The trends in the variation of the electronic and optical properties with the crystal structure and the group VI anion atomic number are explored qualitatively.

7.2 Crystal Structures

In Figure 7.1, the kesterite (KS) and stannite (ST) structures [180] are presented for Cu_2ZnGeX_4. KS structure ($I\bar{4}$, No. 82, Figure 7.1a) has its conventional unit cell four Cu atoms on the Wyckoff position $2a$ and $2c$, two Zn atoms on position $2d$, two Ge atoms on position $2b$, and eight X atoms on the $8g$ position. The cation positions have all S_4 point group symmetry, and X has C_1 symmetry. ST structure ($I\bar{4}2m$, No. 121, Figure 7.1b) has fthe equivalent Cu atoms on Wyckoff $4d$ position, two Zn atoms on $2a$, two Ge atoms on $2b$ and eight X atoms on the $8i$ position. The Cu atoms have S_4 point group

symmetry. The Zn and Ge atoms have D_{2d} point group symmetry. Eight X atoms have C_s point group symmetry.

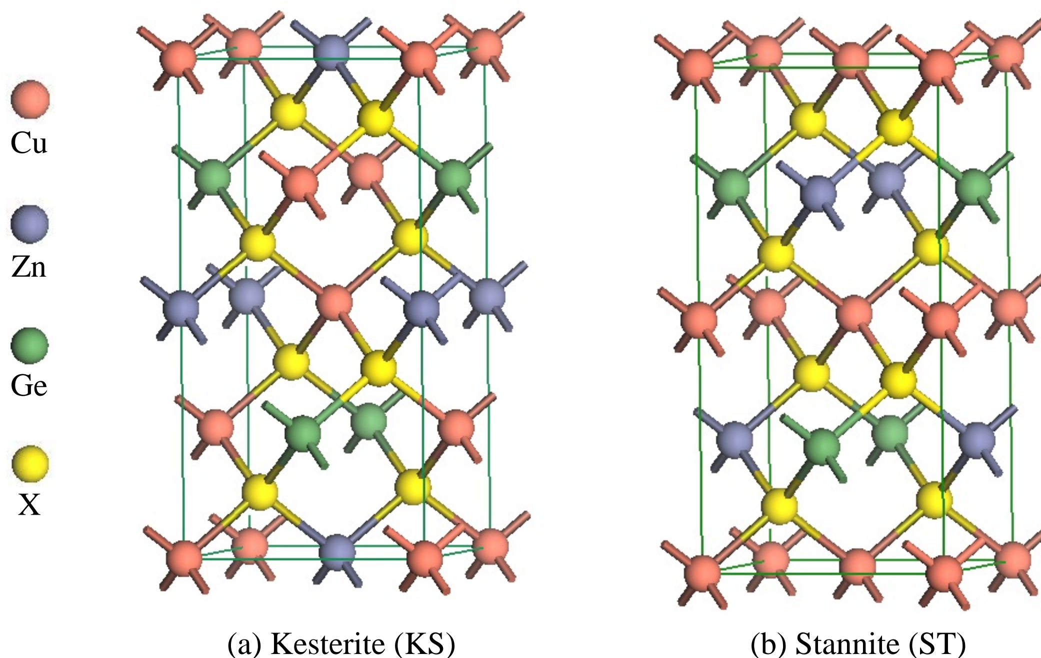

Figure 7.1 The crystal Structures of (a) kesterite (KS) and (b) stannite (ST) Cu_2ZnGeX_4.

It is to be noted that many of the experimental reports [24, 171-174] on these compounds claim that the synthesized samples have ST structure. For example, Parasyuk and co-workers [173, 174] synthesized Cu_2ZnGeS_4, $Cu_2ZnGeSe_4$ and $Cu_2ZnGeTe_4$ samples from high-purity elements and determined their crystal constants by X-ray diffraction. They claim that all the three samples crystallize in the ST structure. It is found that the calculated *c* parameters (Table 7.1) are in general larger than their reported values. This discrepancy between the experiments and the calculations is caused by the fact that the similarity of Cu and Zn atoms leads to the cation disorder in their experimental structures. Because the atomic numbers of Cu, Zn and Ge are close in the periodic table, experimentally, it is very difficult to detect the cation disorder by X-ray diffraction. In fact,

the partial cation disorder has been observed in Cu_2ZnSnS_4 sample instead by a recent neutron-diffraction measurement [166].

7.3 Electronic Properties

The calculated properties of Cu_2ZnGeS_4, $Cu_2ZnGeSe_4$ and $Cu_2ZnGeTe_4$ of KS and ST structures are listed in Table 7.1. Together listed are the available experimental values for comparison.

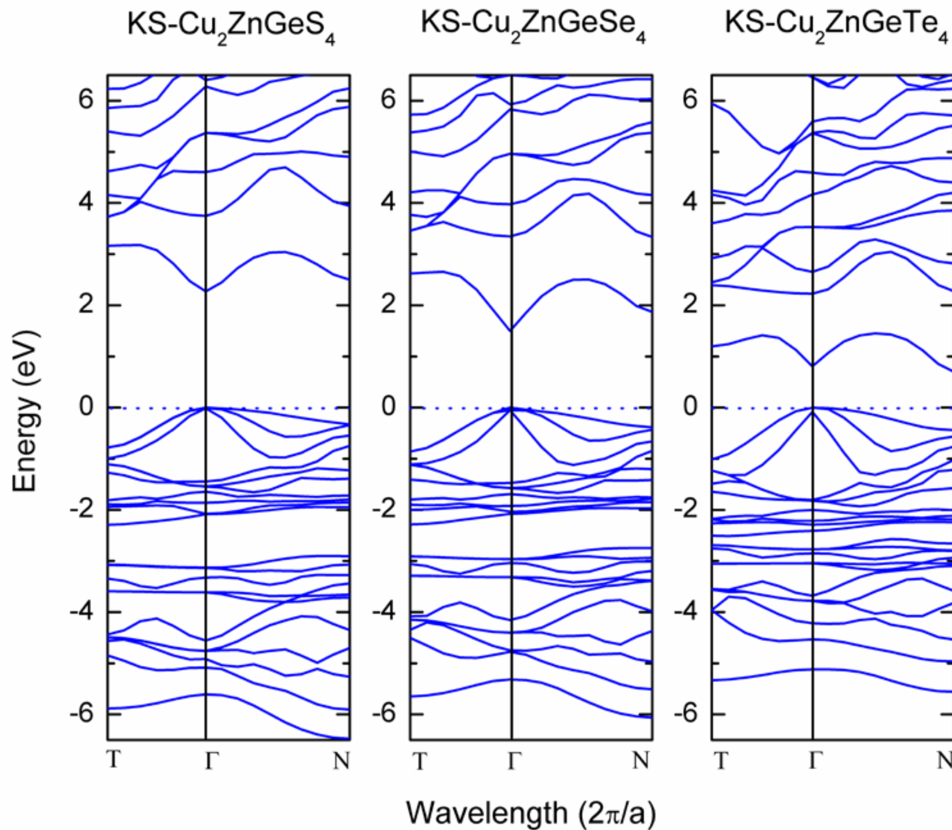

Figure 7.2 Calculated band structures along the high-symmetry lines in the first Brillouin zone: T(Z): $2\pi/a$ (0, 0, 0.5) → Γ : $2\pi/a$ (0, 0, 0) → N(A): $2\pi/a$ (0.5, 0.5, 0.5), for Cu2ZnGeS4, Cu2ZnGeSe4 and Cu2ZnGeTe4 in KS structure.

Table 7.1 Calculated Properties of Cu_2ZnGeX_4 (X=S, Se and Te)

	Cu_2ZnGeS_4			$Cu_2ZnGeSe_4$			$Cu_2ZnGeTe_4$		
	KS	ST	EXP.	KS	ST	EXP.	KS	ST	EXP.
a (Å)	5.264	5.328	5.270, 5.342	5.602	5.583	5.606, 5.610	6.102	6.094	5.954, 5.999
c (Å)	10.843	10.741	10.509,10.516, 10.540	11.259	11.325	11.04	12.126	12.220	11.848, 11.918
E_g (eV)	2.27	2.06	2.15, 2.28, 2.04	1.50	1.32	1.52, 1.29	0.81	0.55	—
E_{1A} (eV)	2.832	2.588	2.85, 2.87, 2.88	2.258	1.838	—	1.139	0.659	—
E_{1B} (eV)	3.946	3.751	4.03, 4.28, 4.34	3.483	3.171	—	2.214	1.793	—
n_0	2.61	2.63	—	2.90	3.00	—	3.73	4.23	—
ε_0	6.84	6.89	—	8.41	9.01	—	13.89	17.93	—
ε_∞	0.49	0.50	0.47, 0.49, 0.76	0.52	0.53	—	0.50	0.54	—

Calculated lattice constant a and c, band gap E_g and critical point threshold energy E_{1A} and E_{1B}, static optical constants. Experimental data (EXP) are listed for comparison, whereas "—" means no experimental data are currently available.

7.3.1 Band Structures

The band structures for the three compounds in KS structure are shown along the $\mathrm{T}(\mathrm{Z}) \rightarrow \Gamma \rightarrow \mathrm{N}(\mathrm{A})$ lines in Figure 7.2. All the band gap values are given in Table 7.1. It is found that the band structures of all the compounds are rather comparable. The lowest conduction band (CB) is a sole band at about 1-3 eV. This is very characteristic for I_2-II-IV-VI_4 family and it is also different from that of chalcopyrite CIGS and CIGSe compounds which have overlapping conduction bands [180]. The calculations indicate that the band gap decreases with the increasing anion atomic numbers [52]. For example, the band gap is 2.27 eV for KS-Cu_2ZnGeS_4 compared to 1.50 eV for KS-$Cu_2ZnGeSe_4$ and 0.81 eV for KS-$Cu_2ZnGeTe_4$. This is because the valence band maximum (VBM) is composed

of hybridized Cu 3*d* and group VI *p* states. The shallower atomic level of heavy anion atom results in higher VBM states, and therefore smaller band gaps. Comparison of the band structures between KS and ST structures shows that band gaps of the KS structure are in general larger than those of ST structure. This is due to the fact that the KS structure has larger anion displacements. For example, the anion displacement in $Cu_2ZnGeSe_4$ system is 0.2542 for KS structure compared to 0.2479 for ST structure [179]. The band gaps of these compounds range from 0.55 to 2.27 eV, covering a wide range of solar spectra. In particular, $Cu_2ZnSnSe_4$, with band gap values of 1.5 eV for KS and 1.32 eV for ST structure, is a potential candidate for photovoltaic applications.

7.3.2 Density of States

The density of states (DOS) of Cu_2ZnGeS_4 in KS and ST structures, $Cu_2ZnGeSe_4$ and $Cu_2ZnGeTe_4$ in KS structure are shown in Figure 7.3. From the calculated DOS, it can be clearly seen that the DOS of the KS and ST structures are quite similar. The upper VB DOS contains mainly the hybridization between *p* states from the anion atoms and 3*d* state from Cu atoms while the lower CB DOS consists mainly of the hybridization between cation *s* states and anion *p* states. Comparing the DOS between different structures and compounds, It is found that: (I) The valence band width of KS structure is slightly narrower than that of the ST counterpart. This is because the KS structure has longer Cu-VI (VI=S, Se and Te) bonds and hence larger anion displacement than the corresponding ST structure. Therefore, the hybridization between Cu 3*d* state and anion *p* state is weaker in the KS structure, leading to a narrower band width; (II) Analyzing the band structure in Figure 7.2 together with the DOS in Figure 7.3 shows that the lowest solo conduction band is derived from the Ge 4*s* and anion *p* states. The conduction band shifts to the lower energy when the anion

atomic number increases from S to Te; (III) In the valence band region, from -6 eV to -2.5 eV, there are bonding states consisting of anion *p* states hybridized with Cu 3*d* state. From -2.5 eV to 0 eV, there are anti-bonding states consisting of anion *p* states hybridized with Cu 3*d* state. The overlapping (at around -2.5 eV) between the *p*-*d* bonding and anti-bonding states increases when the group VI anion atomic number increases from S to Te.

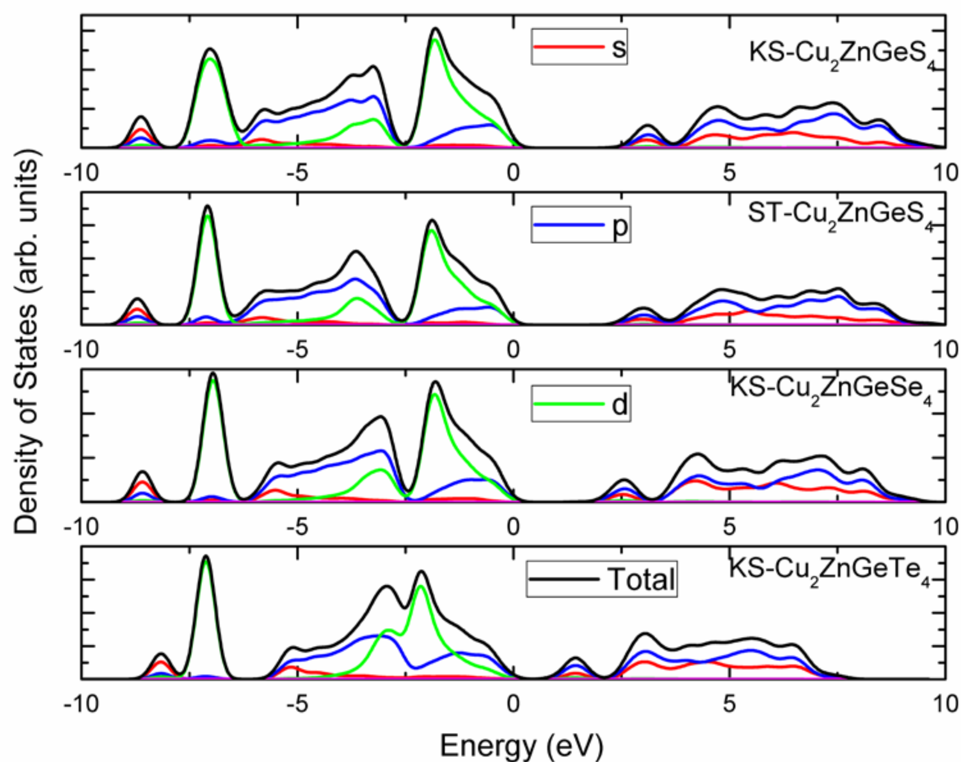

Figure 7.3 The partial and total DOS of Cu_2ZnGeS_4 in KS and ST structures, $Cu_2ZnGeSe_4$ and $Cu_2ZnGeTe_4$ in KS structure.

7.4 Optical Properties

7.4.1 Dielectric Functions and Interband Transitions

Figure 7.4 gives the dielectric function $\varepsilon(\omega)=\varepsilon_1(\omega)+i\varepsilon_2(\omega)$ of all the three compounds in KS and ST structures. Overall, the three compounds show similar dielectric functions over a broad range of energy. The main difference is that the spectrum shifts to lower energy region when the anion atomic number increases. In the lower energy region, the spectrum of $Cu_2ZnGeTe_4$ compound is above the other two materials while the spectrum of Cu_2ZnGeS_4 compound is above the others in the higher energy region. The spectra exhibit some critical point (CP) structures E_{1A}, E_{1B} labeled in Figure 7.4 and listed in Table 7.1. The E_{1A} and E_{1B} energy thresholds can be attributed to transitions at the high CPs N(A) and T(Z) of the first Brillouin zone. According to the band structures in Figure 7.2, it is found that E_{1A} and E_{1B} are 2.83 and 3.95 eV respectively for KS-Cu_2ZnGeS_4 while a recent ellipsometry measurement [177] shows 2.85-2.88 eV for E_{1A} and 4.03-4.34 eV for E_{1B}, as listed in Table 7.1. The calculated results are in good agreement with the experimental values. It is also interesting to analyze the shift in the spectra as a function of the anion atomic number in the three compounds. As it has been stated, the conduction band is derived from the hybridization of the Ge 4*s* and anion *p* states. When the anion atomic number increases (e. g. S$\rightarrow$Se$\rightarrow$Te), the Ge-VI hybridization becomes higher which shifts downward the CBM, and hence the spectrum moves toward the lower energy regime.

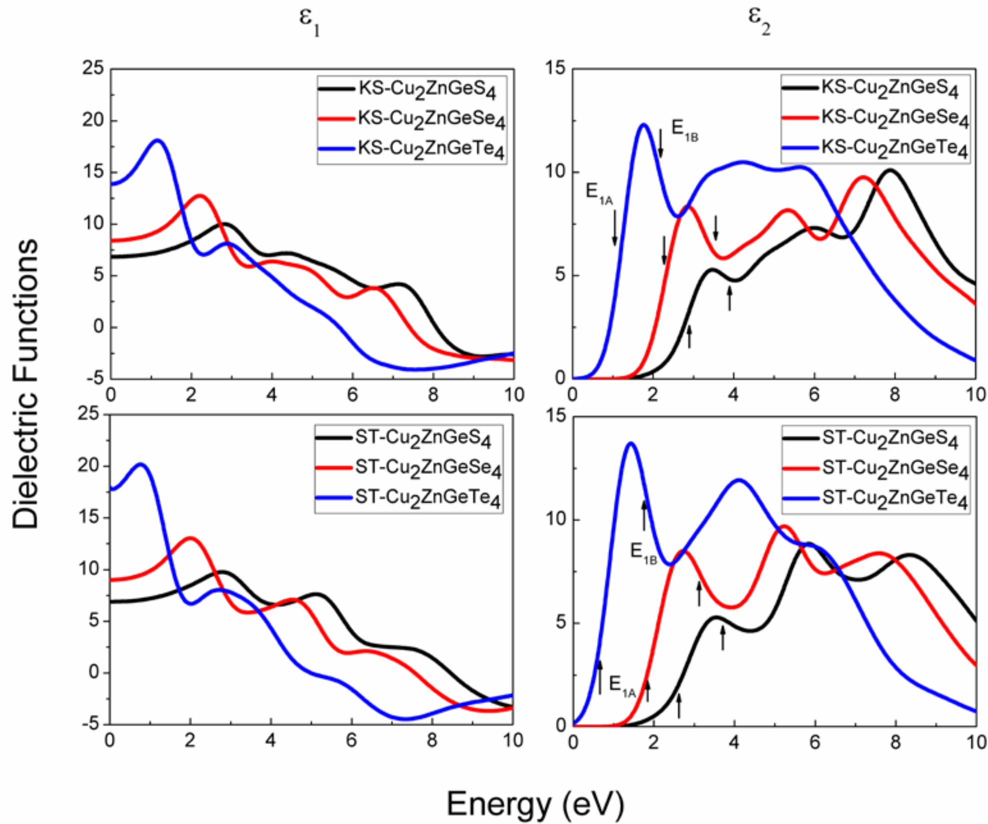

Figure 7.4 The dielectric function $\varepsilon(\omega)=\varepsilon_1(\omega)+i\varepsilon_2(\omega)$ of Cu_2ZnGeS_4, $Cu_2ZnGeSe_4$ and $Cu_2ZnGeTe_4$ in KS and ST structures. The left panels represent the real part $\varepsilon_1(\omega)$ and the right panels represent the imaginary part $\varepsilon_2(\omega)$. The optical transitions E_{1A} and E_{1B} are labeled in the $\varepsilon_2(\omega)$ spectra.

7.4.2 Refractive Index

The optical complex refractive index $\tilde{n} = n + ik$ that are of interest for the design of optoelectronic devices can be computed from dielectric functions [181]. Figure 7.5 presents the energy dependent n and k values of all the three compounds in KS and ST phases. In experiment, n and k of Cu_2ZnGeS_4 in the energy range from 1.4 to 4.7 eV are reported [177]. The calculated results are in good accord with the experimental values. For example, the calculated n at energy 1.4 eV is 2.73 compared to the corresponding 2.65

from experiment. The peak values from experiment at energy range of 2.4 -2.9 eV is 3.02 compared to the calculated 3.05-3.10 in Figure 7.5. It is found that the static refractive index (n_0 in Table 7.1) increases from sulfide to telluride compound and increases from KS to ST structure.

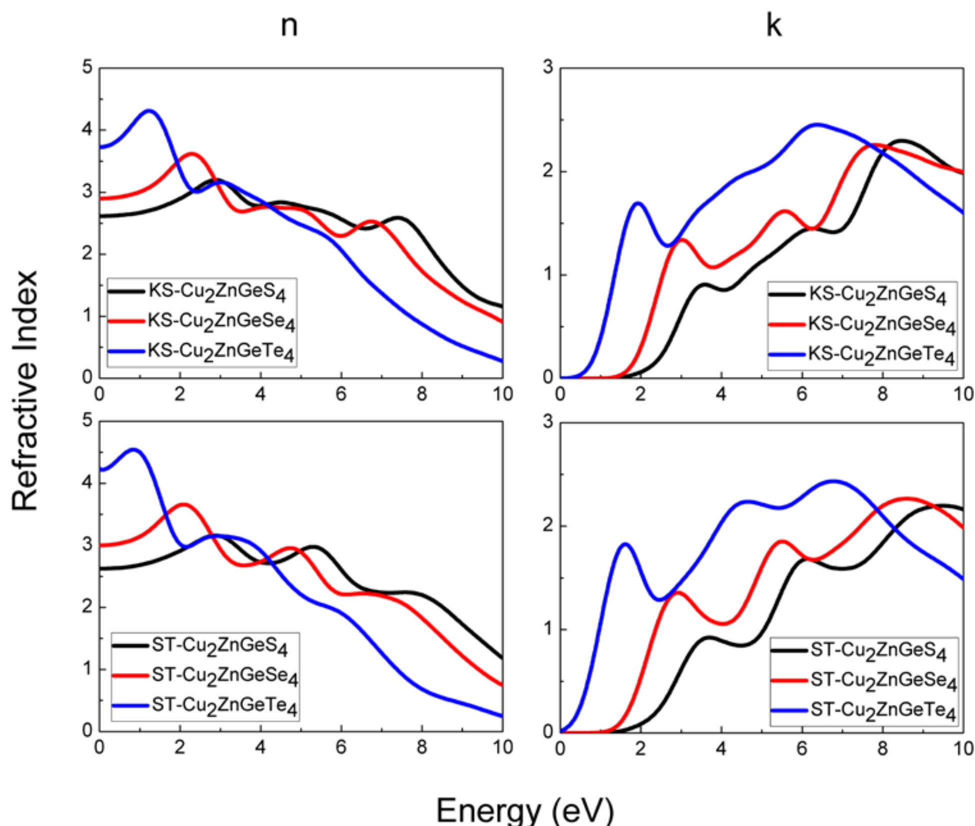

Figure 7.5 The complex refractive index of Cu_2ZnGeS_4, $Cu_2ZnGeSe_4$ and $Cu_2ZnGeTe_4$ in KS and ST structures. The left panels represent the refractive index *n* and the right panels represent the extinction coefficient *k*.

7.4.3 Absorption and Reflectivity

In Figure 7.6, the presented are the calculated results of the absorption coefficient α and normal incident reflectivity *R* for all the cases, which represent the linear optical response from the VBs to the lowest CBs. Due to the fact that the absorption and reflectivity are

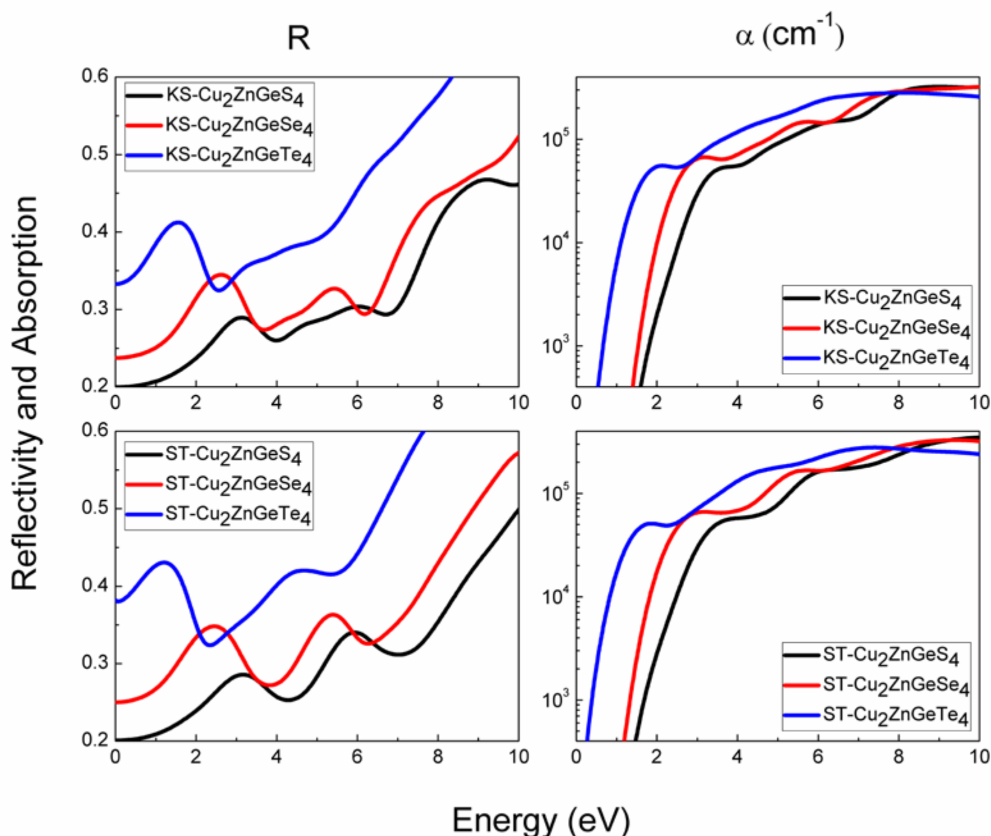

Figure 7.6 The normal incident reflectivity and absorption coefficient of Cu_2ZnGeS_4, $Cu_2ZnGeSe_4$ and $Cu_2ZnGeTe_4$ in KS and ST structures. The left panels represent the reflectivity R and the right panels represent the absorption coefficient α (cm^{-1}). The absorption coefficient is plotted in logarithm scale.

obtained from the dielectric function [181], all the compounds in this study have similar absorption spectra, although with different energy for the onset to absorption (i.e., the band gap energy). It is found that the Cu_2ZnGeS_4 compound has large band-edge absorption coefficient (about 5×10^4 cm^{-1}). At a given photon energy, the $Cu_2ZnGeTe_4$ compound has the largest absorption coefficient while the Cu_2ZnGeS_4 compound has the smallest value. Comparison with the calculated spectra of other materials [180, 182] shows that the absorption coefficient of Cu_2ZnGeX_4 is smaller than that of Cu_2ZnSnX_4 and Cu_2ZnTiX_4

has the largest absorption coefficient. This might indicates that the compounds with heavier group IV elements should have higher light transformation efficiency. It is noticed that, in the energy range of 1.5 – 4.0 eV, the reflectivity and absorption coefficient decreases for all the compounds. This energy region corresponds to the gap between the lowest solo CB and the upper CBs of the band structures in Figure 7.2, since the upper CBs do not contribute to the optical absorption in the low energy regime. This conduction band gap is a disadvantage for the band-edge absorption efficiency in KS and ST structures.

7.5 Summary

In this chapter, the electronic and optical properties of Cu_2ZnGeS_4, $Cu_2ZnGeSe_4$ and $Cu_2ZnGeTe_4$ in KS and ST structures are studied. Band structures and optical spectra such as the dielectric function, refractive index, absorption coefficient and reflectivity have been determined. It is found that the conduction band shifts downward and the overlapping between *p-d* bonding and anti-bonding states in the valence band increases when the system changes from Cu_2ZnGeS_4 to $Cu_2ZnGeSe_4$ and then $Cu_2ZnGeTe_4$. Some critical points in the optical spectra are assigned to the interband transitions according to the calculated band structures. The electronic structures and optical spectra are rather similar in shape for all the compounds. When anion atomic number increases from S to Te, the optical spectra shift to the low energy regime. A good agreement between the calculated results and the experimental data has been obtained.

CHAPTER 8

CONCLUSIONS AND FUTURE WORK

8.1 Conclusions

As one of the most fundamental properties, the elastic modulus and elastic constants of binary and ternary III-V & II-VI are modeled in this work based on the existing models for bulk modus and average shear modulus. New expressions are developed for the average Young's modulus as well as the shear modulus and Young's modulus on (111) plane for diamond and zincblende semiconductors. The proposed models provide a simple and accurate meaning to predict the elastic properties of new materials. It is found that the bond length between two nearest neighbor atoms dominates the elastic modulus while ionicity only plays a secondary role.

In Chapters 3 and 4, the crystal structures, formation enthalpies and electronic properties of alloys GaP_xSb_{1-x}, InP_xSb_{1-x} and CdS_xTe_{1-x} are studied using first-principles calculations. These alloys are studied for various structures (ordered: CA, CH, CP, Y2, FM, LZ; disordered: SQS8) and compositions (0, 0.25, 0.5, 0.75, 1). Comparison between GaP_xSb_{1-x} and InP_xSb_{1-x} shows that: (I) The formation enthalpy has maximum value at composition x=0.5; (II) The crystal field splitting and band gap are larger in GaP_xSb_{1-x} than in InP_xSb_{1-x}. In the study of CdS_xTe_{1-x} system, it is found that (I) CH is the ground state structure. Y2 ordering can occur in disordered structure due to small energy difference; (II) Ordering can significantly affect the SO splitting and energy gap; (III) Negative bowing parameter of spin-orbit splitting is found in ordered structure while positive value is found in disordered structure; (IV) the bowing parameters of energy gap and SO splitting are both

strongly ordering and composition dependent. However, the bowing parameter of energy gap increases with the decreasing of the bowing parameter of SO splitting.

It is realized that the work in Chapter 2 does not include the effects of detailed crystal structures and the work in Chapters 3 and 4 consider only the fully ordered and fully disordered structures. However, the experimental samples in general only contain spontaneous ordering to a certain degree. In Chapter 5, a recipe is given to calculate the properties of alloys for any degree of order. Five Y2 ordered III-V ternary alloys are used as examples. For the partially ordered samples, the trends in the Y2 ordering induced changes in the crystal field splitting and band gap narrowing are explored and explained in terms of the lattice mismatch and band offset between the binary constituents. The Y2 ordering induced change in the spin-orbit splitting is found to be positive and small. The calculated results in this chapter can be useful in analyzing experimental valence band structure results and deriving the ordering parameters for partially ordered samples.

Regarding the pressure effects during the fabrication of semiconductor alloys as well as their applications in high or low pressure conditions, Chapter 6 models the pressure dependence of the energy gap of a number of group III-V & II-VI ternary semiconductor alloys. In addition to the good agreement between the predicted results and the available experimental values, the pressure coefficient model also shows the following: (I) The pressure coefficient of the energy gap increases with increasing nearest neighbor distance in common cation system; (II) The pressure coefficient of the energy gap decreases with increasing ionicity; (III) The energy gap increases with decreasing nearest neighbor distance and increasing ionicity.

In the development of solar cell materials, the I_2-II-IV-VI_4 quaternary semiconductors have recently attracted much more attentions because they only contain abundant, nontoxic and inexpensive elements. However, the most fundamental properties, such as, the crystal and electronic structures, optical constants are still unknown. In Chapter 7, the electronic and optical properties of Cu_2ZnGeS_4, $Cu_2ZnGeSe_4$ and $Cu_2ZnGeTe_4$ in KS and ST structures are studied. Band structures and optical spectra such as the dielectric function, refractive index, absorption coefficient and reflectivity are determined. The critical points in the optical spectra are assigned to the interband transitions according to the calculated band structures. Moreover, it is found that: (I) The conduction band shifts downward and the overlapping between *p-d* bonding and anti-bonding states in the valence band increases when the system changes from Cu_2ZnGeS_4 to $Cu_2ZnGeSe_4$ and then $Cu_2ZnGeTe_4$; (II) The electronic structures and optical spectra are rather similar in shape for all the compounds; (III) When anion atomic number increases from S to Te, the optical spectra shift to the low energy regime.

8.2 Future Work

For the ternary semiconductor alloys, the study in Chapter 6 does not consider the detailed crystal orderings. In order to improve the work, the pressure dependence of the band gap and other properties at different crystal structures should be studied in the future. The study should also take into account the possible phase transitions induced when applying the pressure. As another important physical parameter in semiconductor manufacturing and applications, the temperature effects on the alloy properties, especially, band gap and transport, should be included in future work.

As has been stated before, the research in the I_2-II-IV-VI_4 quaternary semiconductors is still at the very early stage. The structural, electronic and optical properties of other members in the I_2-II-IV-VI_4 family should be further studied in order to select more potential candidates for solar cell absorbers.

REFERENCES

1. S. Adachi, *Handbook on physical properties of semiconductors*. *Vol. 2*. 2004: Kluwer Academic, New York, New York.

2. V. A. Elyukhin, V. M. Sanchez-R, and O. V. Elyukhina, *Self-assembling in* $Al_xGa_{1-x}N_yAs_{1-y}$ *alloys.* Applied Physics Letters, 2004. **85**(10): p. 1704-1706.

3. Y. Y. Peter, and M. Cardona, *Fundamentals of semiconductors: physics and materials properties. Ed. 3*. 2005: Springer-Verlag, Berlin, Germany.

4. J. D. Plummer, M. D. Deal, and P. B. Griffin, *Silicon VLSI Technology: Fundamentals, Practice and Modeling*. 2000: Prentice Hall, Upper Saddle River, New Jersey.

5. A. Piotrowski, P. Madejczyk, W. Gawron, K. Klos, J. Pawluczyk, J. Rutkowski, J. Piotrowski, and A. Rogalski, *Progress in MOCVD growth of HgCdTe heterostructures for uncooled infrared photodetectors*. Infrared Physics & Technology, 2007. **49**(3): p. 173-182.

6. H. Ibach, and H. Lüth, *Solid State Physics. Ed. 3*. 2003, Springer, Berlin, Germany.

7. H. G. B. Hicks, and D. F. Manley, *High purity GaAs by liquid phase epitaxy.* Solid State Communications, 1969. **7**(20): p. 1463-1465.

8. T. D. Moustakas, J. I. Pankove, and Y. Hamakawa. *Wide Band Gap Semiconductors*. 1992: Materials Research Society, Pittsburgh, Pennsylvania.

9. P. G. Neudeck, *Progress in silicon carbide semiconductor electronics technology.* Journal of Electronic Materials, 1995. **24**(4): p. 283-288.

10. M. Bhatnagar, and B. J. Baliga, *Comparison of 6H-SiC, 3C-SiC, and Si for power devices.* IEEE Transactions on Electron Devices, 1993. **40**(3): p. 645-655.

11. P. Kung, A. Yasan, R. McClintock, S. Darvish, K. Mi, and M. Razeghi, *Future of* $Al_xGa_{1-x}N$ *materials and device technology for ultraviolet photodetectors.* SPIE Proceedings. 2002. **4650**. p:199-206.

12. A. Saxler, W. C. Mitchel, P. Kung, and M. Razeghi, *Aluminum gallium nitride short-period superlattices doped with magnesium.* Applied Physics Letters, 1999. **74**(14): p. 2023-2025.

13. M. Suzuki, J. Nishio, M. Onomura, and C. Hongo, *Doping characteristics and electrical properties of Mg-doped AlGaN grown by atmospheric-pressure MOCVD*. Journal of Crystal Growth, 1998. **189-190**: p. 511-515.

14. M. Haase, J. Qiu, J. M. DePuydt, and H. Cheng, *Blue-green laser diodes.* Applied Physics Letters, 1991. **59**(11): p. 1272-1274.

15. L. Zeng, A. Cavus, B. X. Yang, M. C. Tamargo, N. Bambha, A. Gray, and F. Semendy, *Molecular beam epitaxial growth of lattice-matched* $Zn_xCd_yMg_{1-x-y}Se$ *quaternaries on InP substrates*. Journal of Crystal Growth, 1997. **175–176**(1): p. 541-545.

16. D. Pavlidis, *Wide-and narrow-bandgap semiconductor materials.* Thema Forschung, 2006. **2**: p. 38-41.

17. P. Capper, J. Garland, and I. M. Baker, *HgCdTe photovoltaic infrared detectors*, in Mercury Cadmium Telluride, 2010, John Wiley & Sons, Hoboken, New Jersey. p. 447-467.

18. P. Capper, *Narrow-bandgap II–VI semiconductors: Growth*, in Springer Handbook of Electronic and Photonic Materials, 2007, Springer-Verlag, Berlin, Germany. p. 303-324.

19. V. V. Tyagi, N. A. A. Rahim, N. A. Rahim, and J. A. L. Selvaraj, *Progress in solar PV technology: Research and achievement.* Renewable and Sustainable Energy Reviews, 2013. **20**: p. 443-461.

20. P. A. Iles, *Evolution of space solar cells.* Solar Energy Materials and Solar Cells, 2001. **68**(1): p. 1-13.

21. J. Britt, and C. Ferekides, *Thin-film CdS/CdTe solar cell with 15.8% efficiency.* Applied Physics Letters, 1993. **62**(22): p. 2851-2582.

22. S. S. Hegedus, and B. E. McCandless, *CdTe contacts for CdTe/CdS solar cells: Effect of Cu thickness, surface preparation and recontacting on device performance and stability*. Solar Energy Materials and Solar Cells, 2005. **88**(1): p. 75-95.

23. I. Repins, M. A. Contreras, B. Egaas, C. DeHart, J. Scharf, C. L. Perkins, B. To, and R. Noufi, *19.9%-efficient ZnO/CdS/*$CuInGaSe_2$ *solar cell with 81.2% fill factor.* Progress in Photovoltaics: Research and Applications, 2008. **16**(3): p. 235-239.

24. K. Doverspike, K. Dwight, and A. Wold, *Preparation and characterization of copper zinc germanium sulfide selenide (*$Cu_2ZnGeS_{4-y}Se_y$*)*. Chemistry of Materials, 1990. **2**(2): p. 194-197.

25. Q. Guo, H. W. Hillhouse, and R. Agrawal, *Synthesis of* Cu_2ZnSnS_4 *nanocrystal ink and its use for solar cells.* Journal of the American Chemical Society, 2009. **131**(33): p. 11672-11673.

26. A. Szabo, and N. S. Ostlund, *Modern Quantum Chemistry: Introduction to Advanced Electronic Structure Theory*. 1989: Dover, New York, New York.

27. R. G. Parr, and W. Yang, *Density-Functional Theory of Atoms and Molecules*. 1989: Oxford University Press, Oxford, UK.

28. W. Kohn, and L. J. Sham, *Self-consistent equations including exchange and correlation effects.* Physical Review, 1965. **140**(4A): p. A1133-A1138.

29. J. P. Perdew, and Y. Wang, *Accurate and simple analytic representation of the electron-gas correlation energy*. Physical Review B, 1992. **45**(23): p. 13244-13249.

30. M. C. Payne, M. P. Teter, D. C. Allan, T. A. Arias, and J. D. Joannopoulos, *Iterative minimization techniques for ab initio total-energy calculations: molecular dynamics and conjugate gradients*. Reviews of Modern Physics, 1992. **64**(4): p. 1045-1097.

31. D. R. Hamann, M. Schlüter, and C. Chiang, *Norm-Conserving Pseudopotentials.* Physical Review Letters, 1979. **43**(20): p. 1494-1497.

32. K. Laasonen, A. Pasquarello, R. Car, C. Lee and D. Vanderbilt, *Car-Parrinello molecular dynamics with Vanderbilt ultrasoft pseudopotentials*. Physical Review B, 1993. **47**(16): p. 10142-10153.

33. P. E. Blöchl, *Projector augmented-wave method.* Physical Review B, 1994. **50**(24): p. 17953-17979.

34. G. N. Greaves, A. L. Greer, R. S. Lakes and Rouxel, *Poisson's ratio and modern materials.* Nature Materials, 2011. **10**(11): p. 823-837.

35. M. L. Cohen, *Calculation of bulk moduli of diamond and zinc-blende solids*. Physical Review B, 1985. **32**(12): p. 7988-7991.

36. M. L. Cohen, *Predicting useful materials.* Science, 1993. **261**(5119): p. 307-308.

37. S. Kamran, K. Chen, and L. Chen, *Semiempirical formulae for elastic moduli and brittleness of diamondlike and zinc-blende covalent crystals*. Physical Review B, 2008. **77**(9): p. 094109-094113.

38. J. C. Phillips, *Bonds and bands in semiconductors*. 1973: Academic Press, New York, New York.

39. D. Roundy, C. R. Krenn, M. L. Cohen, and J. W. Morris, *Ideal shear strengths of fcc aluminum and copper.* Physical Review Letters, 1999. **82**(13): p. 2713-2716.

40. R. M. Martin, *Elastic properties of ZnS structure semiconductors.* Physical Review B, 1970. **1**(10): p. 4005-4011.

41. F. Gao, J. He, E. Wu, S. Liu, D. Yu, D. Li, S. Zhang, and Y. Tian, *Hardness of covalent crystals.* Physical Review Letters, 2003. **91**(1): p. 015502-015505.

42. D. Chen, and N. Ravindra, *Elastic properties of diamond and zincblende covalent crystals.* Emerging Materials Research, 2013. **2**(1): p. 58-63.

43. D. N. Lee, *Elastic properties of thin films of cubic system.* Thin Solid Films, 2003. **434**(1): p. 183-189.

44. G. Simmons, and H. Wang, *Single Crystal Elastic Constants and Calculated Aggregate Properties: A Handbook, Ed. 2*. 1971. MIT Press, Cambridge, Massachusetts.

45. D. H. Lee, and J. D. Joannopoulos, *Simple scheme for deriving atomic force constants: Application to SiC.* Physical Review Letters, 1982. **48**(26): p. 1846-1849.

46. W. R. L. Lambrecht, B. Segall, M. Methfessel, and M. Schilfgaarde, *Calculated elastic constants and deformation potentials of cubic SiC.* Physical Review B, 1991. **44**(8): p. 3685-3694.

47. T. Azuhata, T. Sota, and K. Suzuki, *Elastic constants of III-V compound semiconductors: Modification of Keyes' relation.* Journal of Physics: Condensed Matter, 1996. **8**(18): p. 3111-3119.

48. M. Sherwin, and T. Drummond, *Predicted elastic constants and critical layer thicknesses for cubic phase AlN, GaN, and InN on β -SiC*. Journal of Applied Physics, 1991. **69**(12): p. 8423-8425.

49. Q. Xiong, N. Duarte, S. Tadigadapa, and P. C. Eklund, *Force-deflection spectroscopy: A new method to determine the Young's modulus of nanofilaments*. Nano Letters, 2006. **6**(9): p. 1904-1909.

50. E. K. Deligoz, K. Colakoglu, and Y. Ciftci, *Elastic, electronic, and lattice dynamical properties of CdS, CdSe, and CdTe.* Physica B: Condensed Matter, 2006. **373**(1): p. 124-130.

51. T. Alper, and G. Saunders, *The elastic constants of mercury telluride.* Journal of Physics and Chemistry of Solids, 1967. **28**(9): p. 1637-1642.

52. D. Chen, and N. M. Ravindra, *Pressure dependence of energy gap of III–V and II–VI ternary semiconductors.* Journal of Materials Science, 2012. **47**(15): p. 5735-5742.

53. A. De Bernabe, C. Prieto, L. Gonzalez, and A. G. Every, *Elastic constants of $In_xGa_{1-x}As$ and $In_xGa_{1-x}P$ determined using surface acoustic waves.* Journal of Physics: Condensed Matter, 1999. **11**(28): p. L323-L327.

54. C. Y. Yeh, A. B. Chen, and A. Sher, *Formation energies, bond lengths, and bulk moduli of ordered semiconductor alloys from tight-binding calculations*. Physical Review B, 1991. **43**(11): p. 9138-9151.

55. N. Bouarissa, *Compositional dependence of the elastic constants and the Poisson ratio of $Ga_xIn_{1-x}Sb$*. Materials Science and Engineering: B, 2003. **100**(3): p. 280-285.

56. P. Maheswaranathan, R. J. Sladek, and U. Debska, *Elastic constants and their pressure dependences in $Cd_{1-x}Mn_xTe$ with $0<x<0.52$ and in $Cd_{0.52}Zn_{0.48}Te$*. Physical Review B, 1985. **31**(8): p. 5212-5216.

57. T. Brinck, J. S. Murray, and P. Politzer, *Polarizability and volume.* The Journal of Chemical Physics, 1993. **98**(5): p. 4305-4306.

58. J. J. Gilman, *Electronic Basis of the Strength of Materials*. 2003: Cambridge University Press, Cambridge, UK.

59. O. Hildebrand, W. Kuebart, and M. Pilkuhn, *Resonant enhancement of impact in $Ga_{1-x}Al_xSb$.* Applied Physics Letters, 1980. **37**(9): p. 801-803.

60. S. R. Kurtz, R. M. Biefeld, L. R. Dawson, K. C. Baucom, and A. J. Howard, *Midwave (4 μm) infrared lasers and light-emitting diodes with biaxially compressed InAsSb active regions*. Applied Physics Letters, 1994. **64**(7): p. 812-814.

61. R. J. Menna, D. R. Capewell, R. U. Martinelli, P. K. York, and R. E. Enstrom, *3.06 μm InGaAsSb/InPSb diode lasers grown by organometallic vapor‐phase epitaxy*. Applied Physics Letters, 1991. **59**(17): p. 2127-2129.

62. L. Bellaiche, S. H. Wei, and A. Zunger, *Localization and percolation in semiconductor alloys: GaAsN vs GaAsP.* Physical Review B, 1996. **54**(24): p. 17568-17576.

63. L. Bellaiche, S. H. Wei, and A. Zunger, *Composition dependence of interband transition intensities in GaPN, GaAsN, and GaPAs alloys*. Physical Review B, 1997. **56**(16): p. 10233-10240.

64. S. H. Wei, and A. Zunger, *Giant and composition-dependent optical bowing coefficient in GaAsN alloys.* Physical Review Letters, 1996. **76**(4): p. 664-667.

65. L. D. Landau, and E. M. Lifshits, *Statistical physics*. 1969: Pergamon Press, Oxford, UK.

66. A. A. Mbaye, D. M. Wood, and A. Zunger, *Stability of bulk and pseudomorphic epitaxial semiconductors and their alloys.* Physical Review B, 1988. **37**(6): p. 3008-3024.

67. Y. C. Yeo, M. F. Li, T. C. Chong, P. Y. Yu, *Theoretical study of the energy-band structure of partially CuPt-ordered $Ga_{0.5}In_{0.5}P$*. Physical Review B, 1997. **55**(24): p. 16414-16419.

68. M. Behet, B. Stoll, and K. Heime, *Lattice-matched growth of InPSb on InAs by low-pressure plasma MOVPE.* Journal of Crystal Growth, 1992. **124**(1): p. 389-394.

69. M. J. Jou, Y. T. Cheng, H. R. Jen, and G. B. Stringfellow, *Organometallic vapor phase epitaxial growth of a new semiconductor alloy:* $GaP_{1-x}Sb_x$. Applied physics letters, 1988. **52**(7): p. 549-551.

70. S. H. Wei, and A. Zunger, *Band gaps and spin-orbit splitting of ordered and disordered* $Al_xGa_{1-x}As$ *and* $GaAs_xSb_{1-x}$ *alloys*. Physical Review B, 1989. **39**(5): p. 3279-3304.

71. G. B. Stringfellow, *Ordered structures and metastable alloys grown by OMVPE.* Journal of Crystal Growth, 1989. **98**(1): p. 108-117.

72. S. H. Wei, L. G. Ferreira, J. E. Bernard, and A. Zunger, *Electronic properties of random alloys: Special quasirandom structures*. Physical Review B, 1990. **42**(15): p. 9622-9649.

73. F. Bechstedt, and R. Del Sole, *Analytical treatment of band-gap underestimates in the local-density approximation.* Physical Review B, 1988. **38**(11): p. 7710-7716.

74. S. H. Wei, and A. Zunger, *Band-gap narrowing in ordered and disordered semiconductor alloys.* Applied physics letters, 1990. **56**(7): p. 662-664.

75. P. A. Fedders, and M. W. Muller, *Mixing enthalpy and composition fluctuations in ternary III–V semiconductor alloys.* Journal of Physics and Chemistry of Solids, 1984. **45**(6): p. 685-688.

76. E. H. Reihlen, M. J. Jou, D. H. Jaw and G. B. Stringfellow, *Optical absorption and emission of GaP1-xSbx alloys*. Journal of Applied Physics, 1990. **68**(2): p. 760-767.

77. H. Shimomura, T. Anan, and S. Sugou, *Growth of AlPSb and GaPSb on InP by gas-sthece molecular beam epitaxy.* Journal of Crystal Growth, 1996. **162**(3): p. 121-125.

78. M. J. Jou, Y. T. Cheng, H. R. Jen, and G. B. Stringfellow, *OMVPE growth of the new semiconductor alloys* $GaP_{1-x}Sb_x$ *and* $InP_{1-x}Sb_x$. Journal of Crystal Growth, 1988. **93**(1): p. 62-69.

79. E. H. Reihlen, M. J. Jou, Z. M. Fang, and G. B. Stringfellow, *Optical absorption and emission of* $InP_{1-x}Sb_x$ *alloys.* Journal of Applied Physics, 1990. **68**(9): p. 4604-4609.

80. T. Aramoto, S. Kumazawa, H. Higuchi, T. Arita, S. Shibutani, T. Nishio, J. Nakajima, M. Tsuji, A. Hanafusa, T. Hibino, K. Omira, H. Ohyama, and M.

Murozono, *16.0% efficient thin-film CdS/CdTe solar cells.* Japanese Journal of Applied Physics, 1997. **36**(10): p. 6304-6305.

81. D. Wang, Z. Hou, and Z. Bai, *Study of interdiffusion reaction at the CdS/CdTe interface.* Journal of Materials Research, 2011. **26**(05): p. 697-705.

82. A. Fischer, L. Anthony, and A. D. Compaan, *Raman analysis of short-range clustering in laser-deposited CdS_xTe_{1-x} films*. Applied Physics Letters, 1998. **72**(20): p. 2559-2561.

83. A. Ebina, M. Yamamoto and T. Takahashi, *Reflectivity of $ZnSe_xTe_{1-x}$ single crystals.* Physical Review B, 1972. **6**(10): p. 3786-3791.

84. H. Lange, J. Donecker, and H. Friedrich, *Electroreflectance and wavelength modulation study of the direct and indirect fundamental transition region of $In_{1-x}Ga_xP$*. Physica Status Solidi (B), 1976. **73**(2): p. 633-639.

85. D. Chen, and N. M. Ravindra, *Structural, thermodynamic and electronic properties of GaP_xSb_{1-x} and InP_xSb_{1-x} alloys.* Emerging Materials Research, 2013. **2**(2): p. 109-113.

86. J. J. Hopfield, *Fine structure in the optical absorption edge of anisotropic crystals.* Journal of Physics and Chemistry of Solids, 1960. **15**(1): p. 97-107.

87. O. Zakharov, A. Rubio, X. Blasé, M. L. Cohen, and S. G. Louie, *Quasiparticle band structures of six II-VI compounds: ZnS, ZnSe, ZnTe, CdS, CdSe, and CdTe*. Physical Review B, 1994. **50**(15): p. 10780-10787.

88. D. J. Chadi, *Spin-orbit splitting in crystalline and compositionally disordered semiconductors*. Physical Review B, 1977. **16**(2): p. 790-796.

89. S. H. Wei, and A. Zunger, *Negative spin-orbit bowing in semiconductor alloys.* Physical Review B, 1989. **39**(9): p. 6279-6282.

90. P. Carrier, and S. H. Wei, *Calculated spin-orbit splitting of all diamondlike and zinc-blende semiconductors: Effects of $p_{1/2}$ local orbitals and chemical trends*. Physical Review B, 2004. **70**(3): p. 035212-035212-9.

91. J. A. Van Vechten, O. Berolo, and J. C. Woolley, *Spin-orbit splitting in compositionally disordered semiconductors.* Physical Review Letters, 1972. **29**(20): p. 1400-1403.

92. K. Wei, F. H. Pollak, J. L. Freeouf, D. Shvydka, and A. D. Compaan, *Optical properties of $CdTe_{1-x}S_x(0 \leqslant x \leqslant 1)$: Experiment and modeling.* Journal of Applied Physics, 1999. **85**(10): p. 7418-7425.

93. D. W. Lane, *A review of the optical band gap of thin film CdS_xTe_{1-x}*. Solar Energy Materials and Solar Cells, 2006. **90**(9): p. 1169-1175.

94. K. Ohata, J. Saraie, and T. Tanaka, *Optical energy gap of the mixed crystal* CdS_xTe_{1-x}. Japanese Journal of Applied Physics, 1973. **12**(10): p. 1641-1642.

95. J. Heyd, G. E. Scuseria, and M. Ernzerhof, *Hybrid functionals based on a screened Coulomb potential.* The Journal of Chemical Physics, 2003. **118**(18): p. 8207-8215

96. J. Heyd, G. E. Scuseria, and M. Ernzerhof, *Erratum: "Hybrid functionals based on a screened Coulomb potential" [J. Chem. Phys. 118, 8207 (2003)].* The Journal of Chemical Physics, 2006. **124**(21): p. 219906-219906-1.

97. S. H. Wei, S. B. Zhang, and A. Zunger, *First-principles calculation of band offsets, optical bowings, and defects in CdS, CdSe, CdTe, and their alloys*. Journal of Applied Physics, 2000. **87**(3): p. 1304-1311.

98. A. Gomyo, T. Suzuki, K. Kobayashi, S. Kawata, I. Hino, and T. Yuasa, *Evidence for the existence of an ordered state in* $Ga_{0.5}In_{0.5}P$ *grown by metalorganic vapor phase epitaxy and its relation to band gap energy*. Applied Physics Letters, 1987. **50**(11): p. 673-675.

99. T. S. Kuan, T. F. Kuech, W. I. Wang, and E. L. Wilkie, *Long-range order in* $Al_xGa_{1-x}As$. Physical Review Letters, 1985. **54**(3): p. 201-204.

100. S. R. Kurtz, *Anomalous electroreflectance spectrum of spontaneously ordered* $Ga_{0.5}In_{0.5}P$. Journal of Applied Physics, 1993. **74**(6): p. 4130-4135.

101. S. Ruvimov, P. Werner, K. Scheerschmidt, U. Gosele, J. Heydenreich, U. Richter, N. N. Ledentsov, M. Grundmann, D. Bimberg, V. M. Ustinov, A. Yu Egorov, P.S. Kopev, and Z. I. Alferov, *Structural characterization of (In,Ga)As quantum dots in a GaAs matrix.* Physical Review B, 1995. **51**(20): p. 14766-14769.

102. C. Wu, Z. Feng, W. Chang, C. Yang, and H. Lin, *Bond lengths and lattice structure of* $InP_{0.52}Sb_{0.48}$ *grown on GaAs.* Applied Physics Letters, 2012. **101**(9): p. 091902-091902-4.

103. Z. Zhong, J. H. Li, J. Kulik, P. C. Chow, A. G. Norman, A. Mascarenhas, J. Bai, T. D. Golding, and S. C. Moss, *Quadruple-period ordering along [110] in a* $GaAs_{0.87}Sb_{0.13}$ *alloy*. Physical Review B, 2001. **63**(3): p. 033314.

104. A. Franceschetti, and A. Zunger, *Pressure dependence of optical transitions in ordered GaP/InP superlattices.* Applied Physics Letters, 1994. **65**(23): p. 2990-2992.

105. S. H. Wei, D. B. Laks, and A. Zunger, *Dependence of the optical properties of semiconductor alloys on the degree of long-range order*. Applied Physics Letters, 1993. **62**(16): p. 1937-1939.

106. S. H. Wei, and A. Zunger, *Erratum: Dependence of the optical properties of semiconductor alloys on the degree of long-range order. [Appl. Phys. Lett. 62, 1937 (1993)]*. Applied Physics Letters, 1993. **63**(9): p. 1292-1292.

107. S. H. Wei, and A. Zunger, *Calculated natural band offsets of all II-VI and III-V semiconductors: Chemical trends and the role of cation d orbitals*. Applied Physics Letters, 1998. **72**(16): p. 2011-2013.

108. C. S. Baxter, R. F. Broom, and W. M. Stobbs, *The characterization of the ordering of MOVPE grown III–V alloys using transmission electron microscopy*. Surface Science, 1990. **228**(1): p. 102-107.

109. C. S. Baxter, W. M. Stobbs, and J. H. Wilkie, *The morphology of ordered structures in III–V alloys: inferences from a TEM study*. Journal of Crystal Growth, 1991. **112**(2): p. 373-385.

110. E. Morita, M. Ikeda, O. Kumagai, and K. Kanedo, *Transmission electron microscopic study of the ordered structure in GaInP/GaAs epitaxially grown by metalorganic chemical vapor deposition*. Applied Physics Letters, 1988. **53**(22): p. 2164-2166.

111. T. Suzuki, A. Gomyo, S. Iijima, K. Kobayashi, S. Kawata, I. Hino, and T. Yuasa, *Band-gap energy anomaly and sublattice ordering in GaInP and AlGalnP grown by metalorganic vapor phase epitaxy*. Japanese Journal of Applied Physics, 1988. **27**(11): p. 2098-2106.

112. M. Kondow, H. Kakibayashi, S. Minagawa, Y. Inoue, T. Nishino, and Y. Hamakawa, *Influence of growth temperature on crystalline structure in $Ga_{0.5}In_{0.5}P$ grown by organometallic vapor phase epitaxy*. Applied physics letters, 1988. **53**(21): p. 2053-2055.

113. T. Nishino, Y. Inoue, Y. Hamakawa, M. Kondow, and S. Minagawa, *Electroreflectance study of ordered $Ga_{0.5}In_{0.5}P$ alloys grown on GaAs by organometallic vapor phase epitaxy*. Applied physics letters, 1988. **53**(7): p. 583-585.

114. K. Lee, S. Lee, and K. J. Chang, *Optical properties of ordered $In_{0.5}Ga_{0.5}P$ alloys*. Physical Review B, 1995. **52**(22): p. 15862-15866.

115. T. W. Nee, and A. K. Green, *Optical properties of InGaAs lattice-matched to InP*. Journal of Applied Physics, 1990. **68**(10): p. 5314-5317.

116. B. W. Hakki, A. Jayaraman, and C. K. Kim, *Band structure of InGaP from pressure experiments*. Journal of Applied Physics, 1970. **41**(13): p. 5291-5296.

117. J. Chen, J. R. Sites, I. L. Spain, M. J. Hafich, and G. Y. Robinson, *Band offset of GaAs/$In_{0.48}Ga_{0.52}P$ measured under hydrostatic pressure*. Applied physics letters, 1991. **58**(7): p. 744-746.

118. R. Hill, *Energy-gap variations in semiconductor alloys.* Journal of Physics C: Solid State Physics, 1974. **7**(3): p. 521-526.

119. R. Hill, and G. D. Pitt, *The pressure and temperature dependence of electron energy-gaps in semiconductor alloys*. Solid State Communications, 1975. **17**(6): p. 739-742.

120. J. A. Van Vechten, *Quantum dielectric theory of electronegativity in covalent systems. I. Electronic dielectric constant*. Physical Review, 1969. **182**(3): p. 891-905.

121. J. A. Van Vechten, *Quantum dielectric theory of electronegativity in covalent systems. II. Ionization potentials and interband transition energies*. Physical Review, 1969. **187**(3): p. 1007-1020.

122. D. L. Camphausen, G. A. N. Connell, and W. Paul, *Calculation of energy-band pressure coefficients from the dielectric theory of the chemical bond.* Physical Review Letters, 1971. **26**(4): p. 184-188.

123. J. A. Van Vechten, and T. K. Bergstresser, *Electronic structures of semiconductor alloys.* Physical Review B, 1970. **1**(8): p. 3351-3358.

124. I. Vurgaftman, J. R. Meyer, and L. R. Mohan, *Band parameters for III–V compound semiconductors and their alloys.* Journal of Applied Physics, 2001. **89**(11): p. 5815-5875.

125. S. Adachi, *Properties of semiconductor alloys: Group-IV, III-V and II-VI semiconductors. Vol. 28*. 2009: Wiley, Hoboken, New Jersey.

126. J. W. Nicklas, and J. W. Wilkins, *Accurate ab initio predictions of III–V direct-indirect band gap crossovers.* Applied Physics Letters, 2010. **97**(9): p. 091902-091902-3.

127. W. T. Tsang, T. H. Chiu, S. N. G. Chu, and J. A. Ditzenberger, *GaSbAs/AlGaSbAs superlattice lattice matched to InP prepared by molecular beam epitaxy*. Applied Physics Letters, 1985. **46**(7): p. 659-661.

128. R. Teissier, D. Sicault, J. C. Harmand, G. Ungaro, G. Le Roux, and L. Largeau, *Temperature-dependent valence band offset and band-gap energies of pseudomorphic GaAsSb on GaAs.* Journal of Applied Physics, 2001. **89**(10): p. 5473-5477.

129. D. Drews, A. Schneider, T. Werninghaus, A. Behres, M. Heuken, K. Heime, and D. R. T. Zahn, *Characterization of MOVPE grown InPSbInAs heterostructures.* Applied Surface Science, 1998. **123–124**(0): p. 746-750.

130. C. Alibert, G. Bordure, A. Laugier, and J. Chevallier, *Electroreflectance and band structure of* $Ga_xIn_{1-x}P$ *alloys.* Physical Review B, 1972. **6**(4): p. 1301-1310.

131. K. Uchida, P. Y. Yu, N. Noto, and E. R. Weber, *Pressure-induced* $\Gamma - X$ *crossover in the conduction band of ordered and disordered GaInP alloys*. Applied physics letters, 1994. **64**(21): p. 2858-2860.

132. K. Alavi, R. L. Aggarwal, and S. H. Groves, *Interband magnetoabsorption of* $In_{0.53}Ga_{0.47}As$. Physical Review B, 1980. **21**(3): p. 1311-1315.

133. J. D. Lambkin, and D. J. Dunstan, *The hydrostatic pressure dependence of the band-edge photoluminescence of GaInAs.* Solid State Communications, 1988. **67**(8): p. 827-830.

134. L. Desplanque, D. Vignaud, S. Godey, E. Cadio, S. Plissard, X. Wallart, P. Liu, and H. Sellier, *Electronic properties of the high electron mobility* $Al_{0.56}In_{0.44}Sb/Ga_{0.5}In_{0.5}Sb$ *heterostructure.* Journal of Applied Physics, 2010. **108**(4): p. 043704-043704-6.

135. N. Bouarissa, and H. Atheag, *Band structure calculations of* $In_xGa_{1-x}Sb$ *under pressure.* Infrared Physics & Technology, 1995. **36**(6): p. 973-980.

136. W. Shan, J. W. Ager, K. M. Yu, W. Walukiewicz, E. E. Haller, M. C. Martin, W. R. Mckinney, and W. Yang, *Dependence of the fundamental band gap of* $Al_xGa_{1-x}N$ *on alloy composition and pressure*. Journal of Applied Physics, 1999. **85**(12): p. 8505-8507.

137. Z. Dridi, B. Bouhafs, and P. Ruterana, *Pressure dependence of energy band gaps for* $Al_xGa_{1-x}N$, $In_xGa_{1-x}N$ *and* $In_xAl_{1-x}N$. New Journal of Physics, 2002. **4**(1): p. 94.1-94.15

138. A. Chen, and J. M. Woodall, *Photodiode characteristics and band alignment parameters of epitaxial* $Al_{0.5}Ga_{0.5}P$. Applied Physics Letters, 2009. **94**(2): p. 021102-021102-3.

139. C. Bosio, J. L. Stachli, M. Guzzi, G. Burri, and R. A. Logan, *Direct energy gap dependence on Al concentration in* $Al_xGa_{1-x}As$. Physical Review B, 1988. **38**(5): p. 3263-3268.

140. S. H. Wei, and A. Zunger, *Predicted band gap pressure coefficients of all diamond and zinc-blende semiconductors: the chemical trends*. Physical Review B, 1999. **60**(8): p. 5404-5411.

141. S. Adachi, GaAs and related materials: *Bulk semiconducting and superlattice properties*. 1994: World Scientific, Singapore, Singapore.

142. M. C. Tamargo, *II-VI Semiconductor Materials and Their Applications*. 2002: Taylor & Francis, New York, New York.

143. X. D. Yang, Z. Y. Xu, Z. Sun, B. Q. Sun, G. H. Li, I. K. Sou, and W. K. Ge, *Recombination kinetics of Te isoelectronic centers in ZnSTe.* Applied Physics Letters, 2005. **86**(5): p. 052107-052107-3.

144. M. J. Seong, H. Alawadhi, I. Miotkowski, A. K. Ramdas, and S. Miotkowska, *The anomalous variation of band gap with alloy composition: cation vs anion substitution in ZnTe*. Solid State Communications, 1999. **112**(6): p. 329-334.

145. J. Wu, W. Walukiewicz, K. M. Yu, W. Shan, J. W. Ager, III, E. E. Haller, I. Miotkowski, A. K. Ramdas, and C. H. Su, *Composition dependence of the hydrostatic pressure coefficients of the bandgap of* $ZnSe_{1-x}Te_x$ *alloys*. Physical Review B, 2003. **68**(3): p. 033206-033206-4.

146. K. R. Murali, K. Thilagavathy, S. Vasantha, P. Gopalakrishnan, P. R. Oommen, *Photoelectrochemical properties of* CdS_xSe_{1-x} *films.* Solar Energy, 2010. **84**(4): p. 722-729.

147. Y. M. Azhniuk, V. V. Lopushansky, Y. I. Hutych, M. V. Prymak, A. V. Gomonnai and D. R. T. Zahn, *Precipitates of selenium and tellurium in II–VI nanocrystal-doped glass probed by Raman scattering*. physica status solidi (b), 2011. **248**(3): p. 674-679.

148. S. Zerroug, F. Ali Sahraoui, and N. Bouarissa, *Structural parameters and pressure coefficients for* CdS_xTe_{1-x}*: FP-LAPW calculations.* The European Physical Journal B, 2007. **57**(1): p. 9-14.

149. N. Muthukumarasamy, R. Balasundaraprabhu, S. Jayakumar, and M. D. Kannan, *Photoconductive properties of hot wall deposited* $CdSe_{0.6}Te_{0.4}$ *thin films.* Materials Science and Engineering: B, 2007. **137**(1–3): p. 1-4.

150. A. Beliveau, and C. Carlone, *Pressure study of the direct band gap of* $Zn_xCd_{1-x}S$ *mixed crystals.* Semiconductor Science and Technology, 1989. **4**(4): p. 277-279.

151. D. J. Olego, J. P. Faurie, S. Sivananthan, P. M. Raccah, *Optoelectronic properties of* $Cd_{1-x}Zn_xTe$ *films grown by molecular beam epitaxy on GaAs substrates*. Applied physics letters, 1985. **47**(11): p. 1172-1174.

152. O. Madelung, W. Von Der Osten, and U. Rossler, *Landolt-Bornstein: Numerical Data and Functional Relationships in Science and Technology*. 1986: Springer-Verlag, Berlin, Germany.

153. K. Reimann, M. Haselhoff, St. Rubenacke, and M. Steube, *Determination of the pressure dependence of band-structure parameters by two-photon spectroscopy*. Physica Status Solidi (B), 1996. **198**(1): p. 71-80.

154. Z. Zhao, J. Zeng, Z. Ding, X. Wang, and J. Hou, *High pressure photoluminescence of CdZnSe quantum dots: Alloying effect.* Journal of Applied Physics, 2007. **102**(5): p. 053509-053509-3.

155. B. Gil, and D. J. Dunstan, *Tellurium-based II-VI compound semiconductors and heterostructures under strain.* Semiconductor Science and Technology, 1991. **6**(6): p. 428-438.

156. J. Gonzalez, F. V. Perez, E. Moya, and J. C. Chervin, *Hydrostatic pressure dependence of the energy gaps of CdTe in the zinc-blende and rocksalt phases.* Journal of Physics and Chemistry of Solids, 1995. **56**(3–4): p. 335-340.

157. Z. L. Fang, G. H. Li, N. Z. Liu, Z. M. Zhu, H. X. Han, K. Ding, W. K. Ge, and I. K. Sou, *Photoluminescence from* $ZnS_{1-x}Te_x$ *alloys under hydrostatic pressure*. Physical Review B, 2002. **66**(8): p. 085203-085203-6.

158. A. D. Prins, D. J. Dunstan, J. D. Lambkin, E. P. O'Reilly, A. R. Adams, R. Pritchard, W. S. Truscott, and K. E. Singer, *Evidence of type-I band offsets in strained* $GaAs_{1-x}Sb_x/GaAs$ *quantum wells from high-pressure photoluminescence.* Physical Review B, 1993. **47**(4): p. 2191-2196.

159. H. Teisseyre, B. Kozankiewicz, M. Leszczynski, I. Grzegory, T. Suski, M. Bockowski, S. Porowski, K. Pakula, P. M. Mensz, I. B. Bhat, *Pressure and time-resolved photoluminescence studies of Mg-doped and undoped GaN.* Physica Status Solidi (B), 1996. **198**(1): p. 235-241.

160. M. Cardona, *Band parameters of semiconductors with zincblende, wurtzite, and germanium structure*. Journal of Physics and Chemistry of Solids, 1963. **24**(12): p. 1543-1555.

161. W. Shan, W. Walukiewicz, J. W. Ager, K. M. Yu, J. Wu, and E. E. Haller, *Pressure dependence of the fundamental band-gap energy of CdSe.* Applied Physics Letters, 2004. **84**(1): p. 67-69.

162. P. Y. Yu, and M. Cardona, *Temperature coefficient of the refractive index of diamond- and zincblende-type semiconductors*. Physical Review B, 1970. **2**(8): p. 3193-3197.

163. P. A. Fernandes, P. M. P. Salomé, and A. F. Da Cunha, *Study of polycrystalline* Cu_2ZnSnS_4 *films by Raman scattering.* Journal of Alloys and Compounds, 2011. **509**(28): p. 7600-7606.

164. H. Katagiri, K. Jimbo, S. Yamada, T. Kamimura, W. S. Maw, T. Fukano, T. Ito, and T. Motohiro, *Enhanced conversion efficiencies of* Cu_2ZnSnS_4*-based thin film solar cells by using preferential etching technique.* Applied Physics Express, 2008. **1**(4): p. 041201-041202.

165. A. V. Moholkar, S. S. Shinde, A. R. Babar, K. Sim, H. K. Lee, K. Y. Rajpure, P. S. Patil, C. H. Bhosale, and J. H. Kim, *Synthesis and characterization of* Cu_2ZnSnS_4 *thin films grown by PLD: Solar cells.* Journal of Alloys and Compounds, 2011. **509**(27): p. 7439-7446.

166. S. Schorr, H. J. Hoebler, and M. Tovar, *A neutron diffraction study of the stannite-kesterite solid solution series.* European Journal of Mineralogy, 2007. **19**(1): p. 65-73.

167. A. Shavel, J. Arbiol, and A. Cabot, *Synthesis of quaternary chalcogenide nanocrystals: Stannite* $Cu_2Zn_xSn_ySe_{1+x+2y}$. Journal of the American Chemical Society, 2010. **132**(13): p. 4514-4515.

168. M. L. Liu, I. W. Chen, F. Q. Huang, and L. D. Chen, *Improved thermoelectric properties of Cu-doped quaternary chalcogenides of* $Cu_2CdSnSe_4$. Advanced Materials, 2009. **21**(37): p. 3808-3812.

169. C. Sevik, and T. Çağın, *Ab initio study of thermoelectric transport properties of pure and doped quaternary compounds*. Physical Review B, 2010. **82**(4): p. 045202-045202-6.

170. T. K. Todorov, K. B. Reuter, and D. B. Mitzi, *High-efficiency solar cell with earth-abundant liquid-processed absorber.* Advanced Materials, 2010. **22**(20): p. E156-E159.

171. H. Matsushita, T. Ichikawa, and A. Katsui, *Structural, thermodynamical and optical properties of* Cu_2*-II-IV-*VI_4 *quaternary compounds.* Journal of materials science, 2005. **40**(8): p. 2003-2005.

172. H. Matsushita, T. Maeda, A. Katsui, T. Takizawa, *Thermal analysis and synthesis from the melts of Cu-based quaternary compounds Cu-III-IV-VI4 and Cu2-II-IV-VI4 (II= Zn, Cd; III= Ga, In; IV= Ge, Sn; VI= Se)*. Journal of Crystal Growth, 2000. **208**(1-4): p. 416-422.

173. O. V. Parasyuk, I. D. Olekseyuk, and L. V. Piskach, *X-ray powder diffraction refinement of* $Cu_2ZnGeTe_4$ *structure and phase diagram of the* Cu_2GeTe_3*–ZnTe system*. Journal of Alloys and Compounds, 2005. **397**(1): p. 169-172.

174. O. V. Parasyuk, L. V. Piskach, Y. E. Romanyuk, I. D. Olekseyuk, V. I. Zaremba, and V. I. Pekhnyo, *Phase relations in the quasi-binary* Cu_2GeS_3*-ZnS and quasi-ternary* Cu_2S*-Zn(Cd)S-*GeS_2 *systems and crystal structure of* Cu_2ZnGeS_4. Journal of Alloys and Compounds, 2005. **397**(1-2): p. 85-94.

175. G. Q. Yao, H. S. Shen, E. D. Honig, R. Kershaw, K. Dwight, and A. Wold, *Preparation and characterization of the quaternary chalcogenides* $Cu_2B(II)C(IV)X_4$ *[B(II)=Zn, Cd; C(IV)=Si, Ge; X=S, Se]*. Solid State Ionics, 1987. **24**(3): p. 249-252.

176. D. M. Schleich, and A. Wold, *Optical and electrical properties of quarternary chalcogenides.* Materials Research Bulletin, 1977. **12**(2): p. 111-114.

177. M. León, S. Levcenko, R. Serna, G. Gurieva, A. Nateprov, J. M. Merino, E. J. Friedrich, U. Fillat, S. Schorr, and E. Arushanov, *Optical constants of Cu_2ZnGeS_4 bulk crystals*. Journal of Applied Physics, 2010. **108**(9): p. 093502-093502-5.

178. S. Chen, X. G. Gong, A. Walsh, and S. H. Wei, *Electronic structure and stability of quaternary chalcogenide semiconductors derived from cation cross-substitution of II-VI and I-III-VI_2 compounds*. Physical Review B, 2009. **79**(16): p. 165211-1652211-10.

179. Y. Zhang, X. Sun, P. Zhang, X. Yuan, F. Huang, and W. Zhang, *Structural properties and quasiparticle band structures of Cu-based quaternary semiconductors for photovoltaic applications*. Journal of Applied Physics, 2012. **111**(6): p. 063709-063709-6.

180. C. Persson, *Electronic and optical properties of Cu_2ZnSnS_4 and $Cu_2ZnSnSe_4$*. Journal of Applied Physics, 2010. **107**(5): p. 053710-053710-8.

181. C. Lamsal, D. Chen, and N. M. Ravindra, *Optical and Electronic Properties of AlN, GaN and InN: An Analysis.* Supplemental Proceedings: Materials Processing and Interfaces, Volume 1: p. 701-713.

182. X. Wang, J. Li, Z. Zhao, S. Huang, and W. Xie, *Crystal structure and electronic structure of quaternary semiconductors $Cu_2ZnTiSe_4$ and Cu_2ZnTiS_4 for solar cell absorber*. Journal of Applied Physics, 2012. **112**(2): p. 023701-023701-4.